Structural, Electrical, and Magnetic Properties of Pure and Rare Earth Doped $BiFeO_3$

A Thesis
Submitted for the degree of
DOCTOR OF PHILOSOPHY

By

Suresh Pittala
07PHPH14

School of Physics
University of Hyderabad
Hyderabad 500 046
Andhra Pradesh
India

June, 2013

Dedicated .....

To Jesus, who gave me Life and Eternal Life.
&
To My Parents, who nurtured me sacrificially.

DECLARATION

I hereby declare that the work embodied in this thesis entitled "**Structural, Electrical, and Magnetic Properties of Pure and Rare Earth Doped $BiFeO_3$"** is carried out by me, under the supervision of **Dr. S. Srinath**, School of Physics, University of Hyderabad, Hyderabad, India.

Suresh Pittala

Place: Hyderabad.

Date:

CERTIFICATE

This is to certify that the thesis entitled "**Structural, Electrical, and Magnetic Properties of Pure and Rare Earth Doped $BiFeO_3$**" submitted by **Suresh Pittala** to the University of Hyderabad is a bonafide work carried out by him under my supervision. The work embodied in this thesis has not been submitted to any other institute or University for the award of any degree or diploma.

Place: Hyderabad

Date:

(Dr. S. Srinath)
Thesis Supervisor

Dean
School of Physics,
University of Hyderabad.

Acknowledgements

I have great pleasure to write this part of my thesis and express my gratitude to all those who have helped me. First and foremost, to my Lord and savior Jesus Christ, who is God on Earth. I thank Him for all that has come to pass in my life, for I know all of it is in vain if it is not for Him. I want to thank my supervisor and mentor, **Dr. S. Srinath** to help me become the scholarly person I am today; his true belief in my abilities always surpassed my own. The way he encouraged, advised and helped me in an academic, personal life is unforgettable. He made all these six years, meaningful and enjoyable. I felt that it is my privilege to work with such a good person. I once again thank for his continuous guidance and motivation in all aspects during my research period.

I want to thank my doctoral committee, **Prof. M. Ghanashyam Krishna, Prof. V. Seshu Bai** for their valuable suggestions, light throwing discussions. I give very special thanks to **Prof. S. N. Kaul**, my mentor from M.Sc onwards. The discussions we held and all those sparking suggestions he made regarding my research are very much useful to me. His passion for physics and patience challenged me. As a coordinator, Centre for nanotechnology, UH, He allowed me to use PPMS facility. I am very thankful to Him.

I am also extremely thankful to our dean **Prof. S. Chaturvedi** and former Deans, **Prof. S. P. Tewari, Prof. C. Bansal & Prof. Vipin Srivastava,** for their support and providing the necessary facilities. I thank **Prof. K. C. James Raju**, for his valuable suggestions and providing facilities in his Lab. I would also like to thank other **faculty members** of school of physics.

I thank **Dr. P. D. Babu**, UGC-DAE, CSR Mumbai for providing the experimental facilities. I thank **Dr. Koteswararao**, SEST, University of Hyderabad, for allowing me to use instruments in their department. It is my pleasure to acknowledge

Dr. A. Srinivas, DMRL Hyderabad for his timely help and constant support from the very beginning of the research work.

I thank **Mr. Abraham** and other office staff of the school for their timely help on every occasion. I am thankful to all the CIL staff members for technical support they provided. I thank Mr. Turumalaiah, Mr. Lakshmi Narayana, Mr. Ravi Shankar, and Smt. Deepthi for their timely help in providing technical data.

It is with enormous pleasure that I acknowledge the support and encouragements that I received from my seniors D**r. A. Sendil Kumar, Dr. Shinto. P. Mathew** and **Dr. B. Yugandhar.** Their suggestions and encouragement in the lab made easy for analyzing the data. I sincerely thank all my dearly juniors, Prasanna, Ravi Kumar, Uma Sankar, Pavan Venu Prakash, for their valuable help. I thank postdoctoral fellows in my lab Dr. Y. Sundarayya, Dr. K. Praveena for their suggestions in academic issues.

I would like to thank all of my Ph.D batch mates Regina Jose, Dr. Sai priya, Yasashwini, Dr. Gopala Krishna, Dr. Balamurali Krishna, Dr. Sekhar, Dr. Satyanarayana, Suman Kalyan, Siva nasarayya Chari, Hongrey for encouraging and making the whole research period worthful.

I thank all research scholars from School of physics, especially Obulesu, Ramakanth, Anil, Raju, Pavan naik, Tirupati, Sriram, Uma Lavanya, Siva, Kamal and Naresh. I thank M.Sc friends Dr. Sridhar, Dr. Venkatesh, P. Rambabu, Ramudu, Bhaskar, Sudhakar, Sarat, Ravi, Suryanarayana, Sankar Anil for their help in aspects.

I also thank my dearest friends Nellore Srinu, Kesav (Slimboy), Pullarao, Rambabu, Lazapathi, Rajesh, R.K, Sirisha, Vinitha, M Prathyusha, Anitha, Sunitha.

I also want to thank my beloved ones, Kodanda Ram family, Paul Kiran family, Dr. Prakash family, Dr. Srinivas family, Krupanand family, Calvin, Philip, Rajesh dasari, Rajesh Gudipalli, Yellaswamy, Prasad, Joseph Anna, Dr. Rattaiah, Masapogu Raju, Benhur, Prakash Elliot, Raviji (R.K), Vijay Uppu, Ganesh, M. V. Suresh, Bhanu, Vara

Lakshmi, Sujatha, Sudheer staff, Dr. Reddithota (KP), Vijaya Prasad, Staff Anil, Neelima akka, Sunil, Eswar, Chandu, Johnson, Raj Kumar for their kind loving nature, care and spiritual support in all conditions during my stay in the campus.

My special thanks to all EU believers, Dr. Bheem, Dr. Rambabu, Venkaiah anna, Dr. Kishore, Ajay, Nagarjuna, Manoj, Varma, Rajesh, Babu Rao, Kanth, Suresh K, Mani, and my loving sister Prathyusha, Ancy David, Annapurna, Imkum Naro, Radhika and all for their love and fellowship throughout my stay in campus. Joyful movements with them are unforgettable in my life. They made the Life on campus ease and worth.

I am thankful to pastor. B. Paul Martin and family, HBC, Burugagudem for leading me to Christ. My special thanks to Dr. P. Satish Kumar, Calvary Temple, for his encouraging messages. I thank Mr. M. Sunith Kumar, Founder, SAVE A CHILD Orphanage for his guidance. I thank all my family at SAC, especially, Ruth, Salomi, Lissy, Priyanka, Swaroopa, Rajesh, Pragathi, Emmanuel, Samuel, and Cindy.

I am happy to express my gratitude for the financial support from University of Hyderabad BBL, UCG- CAS and BSR, made me to reach my goal in crucial time. Also the support from UGC-DAE CSR project (CRS-M-180) is greatly acknowledged.

I want to take an exclusive moment to praise my family: my parents, Mr. Ramakotaiah Pittala and Mrs. Samrajyam Pittala, without whom I would have ceased to be. Their words: "Get the highest degree you can" has always played in the forefront of my mind. They are truly proud to have produced the first Dr. Pittala in the history of the Pittala's extended family. My brother and sister-in-law, Ramesh babu and Vijaya, have been a great support to me on this journey of life. I also thank all of my relatives for their love, affection and moral support all the time.

Suresh Pittala

CONTENTS **Page no**

Introduction and Motivation of the Present Work: Single phase Mutiferroics

1 Chapter

1.1. Introduction

Multiferroic materials have been of great interest due to their promising applications in new kind of memory devices. These materials have at least two ferroic properties (ferroelectricity, ferromagnetism, ferroelasticity and ferrotoroidicity) that coexist in the same phase.

Although multiferroics were discovered long back, the renaissance in this field actually came when the review article by Nicola Spaldin posed a challenge to researchers in addressing the requirements for simultaneous existence of ferroelectricity and ferromagnetism in oxides [1]. Thereby, scientists started investigations for new materials in their search for the problems raised by Nicola. Secondly, the continual hunt for better technology in the investigation of new materials to be used as better-quality transducers, integrated circuits, magnetic field sensors, and most importantly multiple state memory elements. Besides their abundance in applications, there is a great need to understand the fundamental physics of these materials to improve them in order to make new materials in place of the existing ones.

The multiferroic material can exhibit the following coupling mechanisms:

1. a spontaneous magnetization that can be reoriented with an applied electric field,

2. a spontaneous polarization that can be reoriented with an applied magnetic field.

This leads to magnetoelectric effect (ME effect). This coupling phenomenon increases the degree of freedom in the device technological applications in mass storage. Even though current technologies integrate both electric and magnetic orders, for a long time, no known materials display these properties at room temperature with a considerable coupling.

This work examines the important properties of multiferroic $BiFeO_3$ perovskite oxide and the effect on their properties when doped with rare earth elements.

A brief overview of some of the fundamental and important concepts of magnetism, including brief descriptions of different types of magnetic materials and ferroelectric order(s) that are essential to form magnetoelectrics will be discussed.

1.2 Types of Magnetic orders

1.2.1. Diamagnetism

The motion of electrons in an orbital is analogues to the circulating electric charges. According to ampere's law the circulating electric charge can produce a magnetic field. Such motion of electrons in atoms can be changed by an applied field. In case of a diamagnetic material the effect of an applied field on a single electron orbit is to reduce the effective current of the orbit, and so to produce a magnetic moment opposing the applied field. This is called diamagnetic effect. This effect is summed over all the electrons in the atom, and each atom is regarded as acting independently. The Magnetic susceptibility, χ diamagnetic materials is negative and temperature-independent as shown in figure 1.1. Though the diamagnetism is a part of all magnetic states, it is usually negligible in the presence of permanent magnetic moments. Cu, NaCl, SiO are some examples of diamagnetic materials. Superconductors are also ideal diamagnets [2, 3].

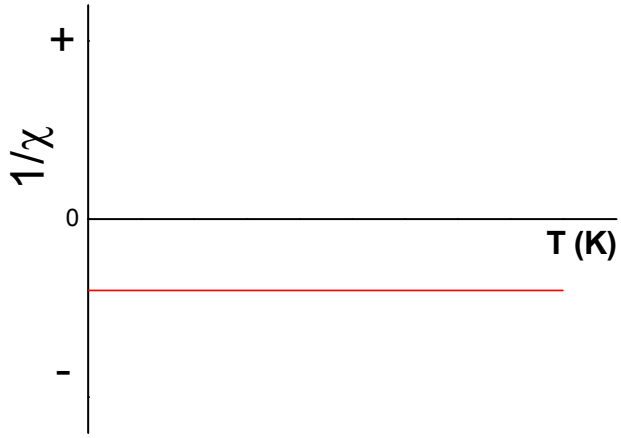

Figure 1.1 Diamagnetic inverse susceptibility.

1.2.2. Paramagnetism

Paramagnets are the materials which have a permanent dipole moment, by virtue of incomplete cancellation of electron spin and/or orbital magnetic moments. This happens only when there are unpaired electrons in the atoms of the material. Thus, a transition metal cation having a partially filled *d* shell exhibit paramagnetism. The net magnetization is zero in the absence of external field due to random alignment of individual magnetic moments of atoms which cancels out each other. When field is applied, all the individual magnetic moments try to align in the field direction, giving rise to large magnetic moment. But, thermal agitation counters their alignment, results in, only a partial

alignment in the field direction giving rise to a small positive susceptibility.

Paramagnetic substances obey Curie law, which indicates that the susceptibility is inversely proportional to their temperature T.

The mathematical expression is shown in Eq.1.1

$$\chi = \frac{C}{T} \qquad (1.1)$$

Where C is the Curie constant, which is a material-specific. The Curie law is only a special case of a more general law, called Curie Weiss law, which states that

$$\chi = \frac{C}{T-\theta} \qquad (1.2)$$

where θ is a constant. Curie-Weiss behavior is shown in figure 1.2.

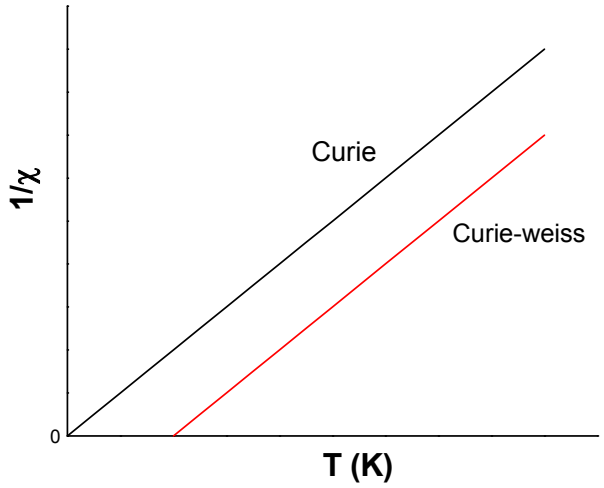

Figure 1.2 Paramagnetic inverse susceptibility (Curie and Curie-Weiss plots).

Paramagnetic materials, due to the lack of net permanent magnetic moment only have a few applications. However, paramagnets are useful in Magnetic resonance imaging (MRI) [4].

1.2.3. Ferromagnetism

Ferromagnetism is a cooperative magnetism leading to a long-range collinear alignment of all the moments in the system [3]. Origin of ferromagnetism comes from the quantum mechanical exchange interaction between permanent magnetic dipoles. The magnetic susceptibility χ of ferromagnets is positive. A divergence in the susceptibility can be observed when $T = \theta$, which corresponds to a phase transition to a spontaneously ordered magnetic phase. When θ is positive, then the material behaves as ferromagnetic as it is below the Curie temperature, T_C, which is a critical temperature above which a ferromagnetic material exhibits paramagnetism.

Ferromagnetism was explained by Weiss in 1906 in terms of a huge internal 'molecular field' proportional to the magnetization [5]. Molecular field is a useful way of approximating the effect of the interatomic Coulomb interaction in quantum mechanics, which Heisenberg described by the Hamiltonian

$$H = -2JS_i.S_j$$

When there is a lattice, the Hamiltonian is generalized to a sum over all pairs of atoms on lattice sites i, j:

$$H = -2\sum_{i>j} J_{ij} S_i . S_j$$

where Si and Sj are operators describing the localized spins on two adjacent atoms i and j and J is the exchange integral. When J > 0 exchange interaction leads to ferromagnetic order.

The typical temperature dependence of the spontaneous magnetization (Ms) is shown in figure 1.3. An ideal ferromagnet becomes a paramagnet above T_C and Curie-Weiss law shows linear dependence between $1/\chi$ and T. Fe, Co, Ni, Dy and Gd are examples of elemental ferromagnets.

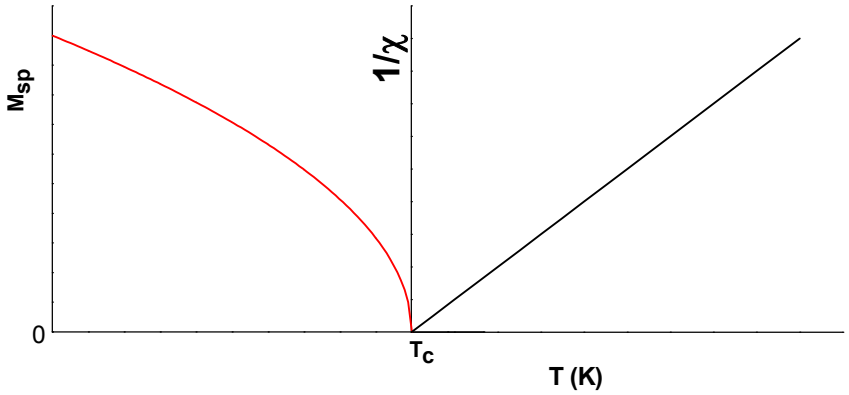

Figure 1.3 Ferromagnetic order parameter and inverse susceptibility

1.2.4. Antiferromagnetism

Two identical magnetic sublattices, with antiparallel moments form a simple antiferromagnet. The origin of this arrangement of the moments comes from the negative exchange interactions i.e. $J < 0$. Antiferromagnets have a small positive susceptibility χ and a linear dependence of magnetization with an applied field [5]. The susceptibility of antiferromagnets is temperature dependent and below T_N, it exhibits antiferromagnetic order and, above this temperature the material behaves like a paramagnet.

Antiferromagnetism, like ferromagnetism, is a cooperative magnetism of long-range order among identical, spontaneous moments. Ideally, the magnetic ions occupy crystallographically identical sites [3]. Antiferromagnetic inverse susceptibility as a function of temperature is shown in figure 1. 4.

Depending on the type of arrangement between the neighboring spins perovskite-type oxide antiferromagnets are further classified into three types (figure 1. 4)

A-Type Antiferromagnets: The intra-plane coupling is ferromagnetic while inter-plane coupling is antiferromagnetic.

C-Type Antiferromagnets: The intra-plane coupling is antiferromagnetic while inter-plane coupling is ferromagnetic.

G-Type Antiferromagnets: Both intra-plane and inter-plane coupling are antiferromagnetic.

These are shows schematically in below figure 1.5.

Some examples of antiferromagnets are FeO, MnS, Fe_3Mn, CrPt, Pt_3Fe etc.

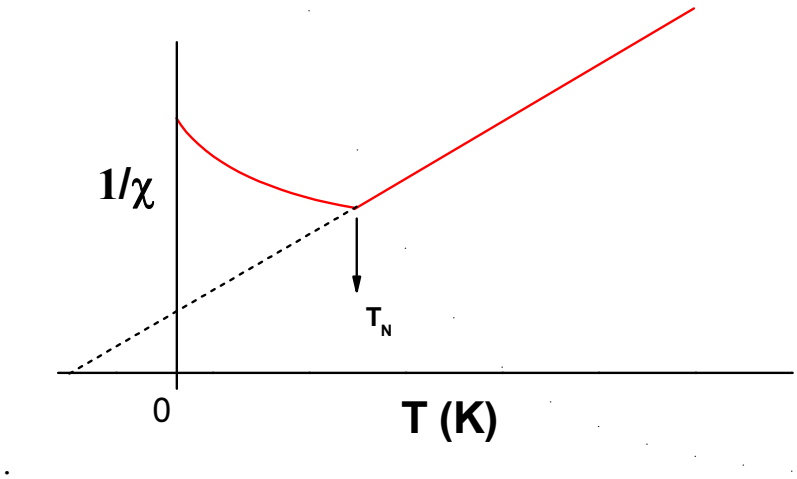

Figure 1.4 Inverse susceptibility as a function of temperature

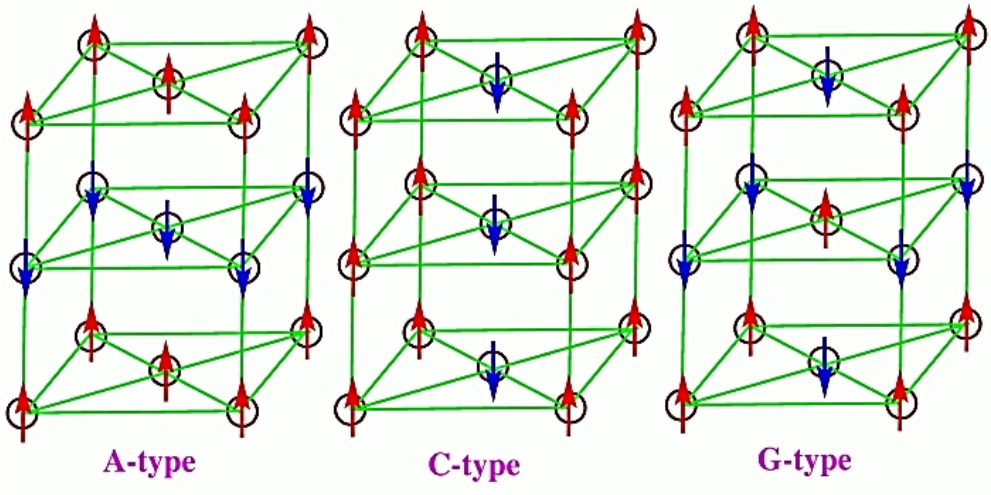

Figure 1.5 Schematic representations of various magnetic orders.

1.2.5. Ferrimagnetism

A Ferrimagnetic material consists of two identical ferromagnetic interpenetrating sublattices which are arranged in opposite direction. The magnetization in one sublattice will have a greater value than that of the other, resulting a net magnetic moment. Thus, ferrimagnetic materials also exhibit a spontaneous magnetization below T_C.

In Ferrimagnets, two (or more) chemically different magnetic species are present. These species may be two different valence states of the same ion (Fe^{2+} and Fe^{3+}) or they may be two different elements (Gd and Co). The magnetization in this system can be understood in the following description [3].

Let us consider that the magnetic ions in a crystalline ferrimagnet occupy two kinds of lattice sites, namely 'A' and 'B', which have different crystallographic environments. The each sub lattice 'A' and 'B' is occupied by the magnetic species, with ferromagnetic alignment between the moments on the sub lattice and between 'A' and 'B' the moments are coupled anti-ferromagnetically. The spontaneous magnetization in the ferrimagnetism results from the combination of these two since the numbers of A and B sites per unit cell and the magnitudes of the A and B moments are different. The two sublattices respond to the temperature differently as they possesses different molecular field in each sublattice. Thus, the net magnetization and P_S have complicated temperature dependence.

According to Weiss theory of ferrimagnetism the total magnetization is given by sum of the individual contributions of sublattice magnetizations. The temperature dependence of spontaneous magnetization can be derived from the expression [6]

$$M_s(T) = \left| M_A(T) + M_B(T) \right|$$

The behavior of M_S (T) with temperature changes depending upon M_A (T) and M_B (T) to be unequal and the different possibilities for sublattice interaction strength. Let us consider two cases to see the variation of total magnetization in two different situations as follows.

First, a compound in which the A–sublattice interaction is antiferromagnetic or only weakly ferromagnetic while the B–lattice interaction is ferromagnetic and much stronger (figure 1.6).

Second, a case where 'A' moments experience more effective molecular field compared to the field that experienced by 'B' moments (figure 1.7).

In first case the M_A (T) decreases rapidly because the effective molecular field experienced by the 'A' moments is smaller than that experienced by the 'B' moments. In the second case, a sign reversal occurs for spontaneous magnetization at a temperature called as "compensation temperature" (Θ_C). In other words the temperature where the spontaneous magnetization becomes zero from its finite value is known as compensation temperature.

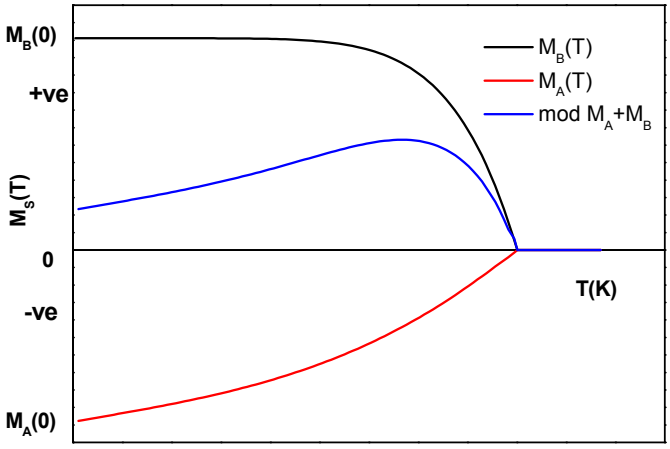

Figure 1.6 Temperature dependence of M_S.

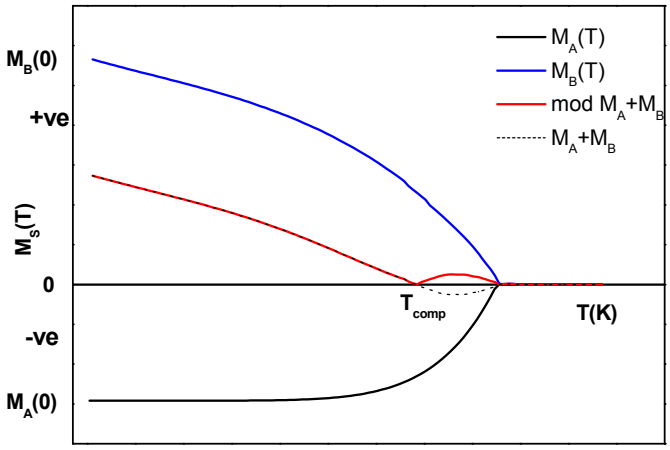

Figure 1.7 Temperature dependence of M_S.

Examples occur in alloys of the form RE-Fe_2, where RE is a heavy rare earth like Tb or Gd. In these alloys, the Fe-Fe and RE-RE couplings are believed to be ferromagnetic, but the Fe-RE interaction is antiferromagnetic [6].

1.3. Magnetic interactions

1.3.1. Super exchange

A common way to predict antiferromagnetic ordering is to consider a system, such as Fe_3O_4, where there are linear chains of Fe^{3+}-O_2 - Fe^{3+} linkages. The oxygen outer electron shell is partially filled with 6 electrons, and so hybridization occurs by the donation of electrons from O_2- ion onto the all vacant spin up (or all spin down) orbitals of the

Fe^{3+} ions. This occurs throughout the chains leaving a zero net magnetic moment from this oxygen mediated interaction [7].

1.3.2. Dzyaloshinskii-Moriya interaction

Dzyaloshinskii-Moriya (DM) interaction is similar to super exchange except that spin orbit interactions mediate the process rather oxygen. This is observed only when the space-time symmetry is broken at the centre of two magnetic sites. Dzyaloshinskii was the first to describe this interaction in 1958 [8]. An exchange interaction occurs between the excited state of magnetic ion and its neighbouring ion which is in ground state. By expanding the thermo dynamical potential he proved the existence of terms representing the Heisenberg exchange, magnetic anisotropy and an additional E_{DM} term which is proportional to the cross product of neighbouring spins S_i and S_j,

$$E_{DM} = -D.\ (S_i \times S_j)$$

Where D is the Dzyaloshinskii-Moriya vector. Couple of years later Moriya developed the general theory for any crystal structure and it is less for symmetric crystals and higher for anisotropic crystals. The effect of DM interaction is usually occurs in many Antiferromagnets to provide a small canting of the moments and then results a weak ferromagnetic component of the moments produced perpendicular to the spin-axis of the antiferromagnet. It is observed in systems like Fe_2O_3,

$MnCO_3$ and $CoCO_3$ etc. This interaction favours the cyclic spin ordering, which has vital implications for multiferroic properties, will be discussed in next chapters.

1.3.3. Crystal Field Splitting

Crystal field splitting occurs in TMO systems; basically the transition metal ion with d^n configurations is perturbed by their chemical environment. If the B cation is in octahedral symmetry then the degeneracy splits 3d orbitals into two different sets, triply degenerate t_{2g} and doubly degenerate e_g orbitals, with an energy difference of Δ_{CF} (figure 1.8).

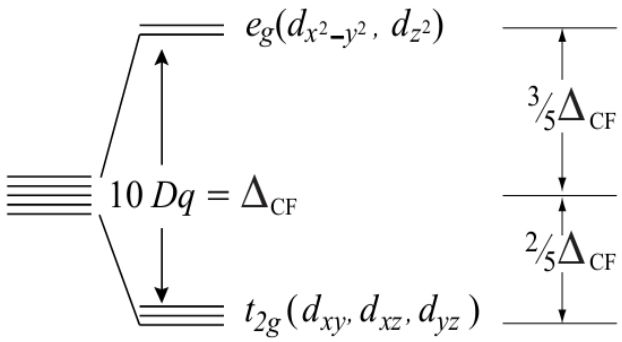

Figure 1.8 Splitting of fivefold degenerate d-orbital of an isolated ion in an octahedral crystal field environment.

Based on Hund's rule the electrons in B cation are accommodated in t_{2g}-e_g orbitals up to the maximum. If the crystal field splitting is larger (Δ) than the pairing energy (U), the electrons first fill up the t_{2g} orbitals

completely. The strength of the crystal field decides the electron configuration, if $\Delta > U$ leads to low spin state and if $\Delta < U$ gives rise to High spin state [5].

1.3.4. Jahn-Teller Distortion

The 3d electron configuration in TMO is decided by the internal crystalline fields. In an octahedral coordination (cubic symmetry) two fold degenerate is present. Jahn and Teller (JT) pointed out that to lower the energy of the crystalline fields at $3d^4$ cations distort the cubic symmetry. Distortion of orbital degenerate configuration to achieve lower energy is known as static JT effect whereas dynamic JT effect is switching of the distortion from one orientation to the other (figure 1.9) [9].

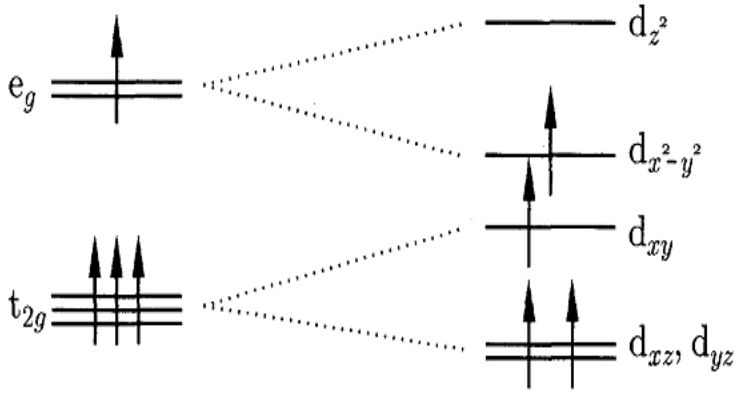

Figure 1.9 Splitting of d-orbital of a TM ion in an octahedral crystal field environment and Jahn-Teller splitting of weak field d^4 configuration.

1.4. Perovskite Structure

ABO_3 stoichiometric materials mostly stabilize in perovskite structure. In ABO_3 formula, generally A is a cation with 2+ valence state and B is a transition metal cation. A is the larger of the three ions. If there is a distortion in perovskites due to external parameters such as temperature, field, pressure and chemical strain induced by doping, the structure transform from cubic symmetry depending upon the ratio of ionic radii of A and B. The transformations may take place from cubic to tetragonal, rhombohedral, or monoclinic depending upon the amount of distortion. To sustain a cubic structure the three ions A, B and O should satisfy two conditions simultaneously. The lattice parameter of the unit cell 'a' should be equal to (r_B+r_O) and $a=\sqrt{2}*(r_A+r_O)$, where r_A,r_B and r_O are the ionic radii of A,B and O. Figure 1.10 shows the typical cubic perovskite structure.

For an ideal contact distance of A and B cations,

$$(r_B+r_O) = 1/\sqrt{2}\ (r_A+r_O)$$

The above condition is difficult to satisfy, if satisfied the existing ions show a perfect perovskite structure for a tolerance factor 't = 1 (in an ideal case)' where t is defined as

$$t*(r_B+r_O) = 1/\sqrt{2}*\ (r_A+r_O).$$

In practice the structure normally remains cubic for *t* in the range from 0.9 to 1.0.

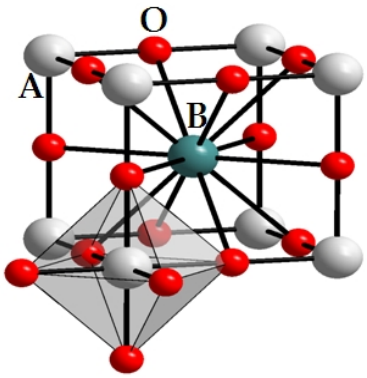

Figure 1.10 The cubic ABO_3 perovskite structure with B cation body center.

1.5. Ferroelectrics

Ferroelectrics are the dielectric materials which have spontaneous polarization and it can be reversed by applying external electric field. Out of the available 32 crystal classes, there are 21 non-centrosymmetric and 11 centrosymmetric (non-polar) groups. Non-centrosymmetry is necessary for a material to exhibit ferroelectric properties. Thus, in these 21 there are 10 polar piezoelectrics [10]. In a polar state, these crystals possess a permanent dipole. A piezoelectric material is one that experiences a change in polarization when it undergoes a mechanical stress. On the other hand, by applying an electric field, the crystal will undergo a change in dimension either being stretched or compressed

depending on the electric field's orientation to the polarization of the crystal.

The crystals fall into the 10 polar groups are considered Ferroelectric in which they have spontaneous polarization, a property that is inherent to their structure.

1.5.1. Ferroelectricity

The property of the materials, possessing spontaneous polarization, the direction of which can be reversed by applied electric field is termed ferroelectricity. The most extensively studied ferroelectrics have the perovskite structure in nature. The non-Centro symmetric structure in perovskites is reached by A or B cations (or both) off-center relative to the oxygen anions, shown in figure 1.10, and the spontaneous polarization comes from the electric dipole moment created by this off centering.

A ferroelectric material possesses spontaneous polarization even in the absence of external electric field. In these materials the centre of negative charges will not coincide with the centre of positive charges, and hence results in a spontaneous polarization. The thermal motion will destroy the ferroelectric order beyond certain temperature; this temperature is called Curie temperature (T_C) or transition temperature. These materials will exhibit high symmetric phase (paraelectric) above

phase transition temperature (T_C) and low symmetric phase (ferroelectric phase) below T_C. The polarization is non-volatile and reversible. In contrast pyroelectric materials, the polarization direction in ferroelectrics can be switched by externally applied field.

Ferroelectric have been extensively used in nonvolatile memory devices, fatigue which arises from multiple cycling of these materials is the obstruction for the application able growth of ferroelectrics. Oxide electrodes are the current research interest in overcoming the fatigue problem. The interest in nondestructive read-out devices, ferroelectric field-effect transistors (FFETs), and ferroelectric ferromagnetic structure devices for memory applications has made ferroelectric materials and multiferroic materials as the future technology suitable materials.

1.5.2. Antiferroelectricity

An antiferroelectric state is defined as the state in which lines of ions in crystal are spontaneously polarized but with neighboring antiparallel polarized lines [11]. Thus, the net polarization is zero in this state. In simple cubic lattice the antiferroelectric state is more stable than the ferroelectric state.

1.6. Maxwell- Wagner dielectric relaxation

In dielectrics, sometimes charge carriers can be blocked at the external electrodes contacting the sample. This results to electrode

polarization or Maxwell-Wagner polarization [12, 13]. Due to this, an additional contribution to the polarization can be oserved as the separation of charges occurs. The charge may be separated over a considerable distance. Therefore, the dielectric loss increases by orders of magnitude than the normal dielectric response.

The Maxwell-Wagner polarization has to be taken into consideration for the materials where interphase polarization is significant. Any kind of secondary phase acts as an internal phase and at the internal phase boundaries charge can be blocked. This phenomena gives rise to a Maxwell-Wagner polarization, which causes a large increase in ε' with decreasing frequency [14].

Even though the Maxwell Wagner mechanism of relaxation is more suitable for inhomogeneous materials, this kind of behavior is also seen in a number of ceramics synthesized through wet chemical routes.

1.7. Multiferroics

Multiferroics are materials that exhibit more than two "ferroic" properties namely ferroelectricity, ferromagnetism, and/or ferroelasticity in the same phase. Materials with coexistence of magnetic and electronic properties are of great interest in recent times which are termed as multifunctional materials. Technically, these materials in a single device form, can perform multiple functions. Multiferroics in recent times

mostly are the materials that combine both ferroelectric and ferromagnetic in the same material. Such kind of materials are attractive for the coupling between the charges and spin order which leads to a phenomenon called as magnetoelectric effect (ME effect). Thus, the materials having the linear ME effect, have promising applications as this additional functionality can give rise to a type of electric-field controlled magnetic data storage device. By using magnetoresistance (the effect of a magnetic field on the conductivity) and magnetocapacitance (the magnetic field dependence on the dielectric properties) measurements, magnetoelectric behavior can be detected. The conditions favoring to form the multiferroic materials are very rare. Theory explored some of the possible restricting factors to exhibit multiferroics. The d-orbital occupancy of the B-site cation in ABO_3 perovskite type materials is a critical variable in deciding the tendency for perovskite materials to exhibit ferroelectricity or ferromagnetism [1]. This d-orbital occupancy problem reduces the chance for materials to be a multiferroic. However, other mechanisms such as ferroelectricity via lone pair will allow for this phenomenon.

1.7.1. Classification of multiferroics

Multiferroics are classified into different subgroups based on the involved mechanism of multiferroicity and its nature. Composites and

Heterostructures have two different origin of multiferroicity in them inspite of exhibiting some coupled effects. Thus depending upon the mechanism these materials have divided into two categories namely Type 1 and Type 2 multiferroics.

a. Type 1 multiferroics

In this class, the origin of the magnetism and ferroelectricity exists independently. The nature of coupling in such systems is weak. The origin for multiferroicity in this type can be in three ways. Firstly, multiferroicity in the materials can arise due to lone pair of electrons. This can be seen in compounds like $BiFeO_3$, $BiMnO_3$ and $PbVO_3$. Secondly due to charge ordering for example in materials like $YbFe_2O_4$, $YMnO_3BaMF_4$ (M = 3d transition metal ion). Geometric frustration is another reason for the origin of mutiferroicity.

b. Type 2 multiferroics

In some materials, strong coupling between magnetism and ferroelectricity can induce the magnetism due to ferroelectricity and vice-versa. The materials falling under this type have spiral or collinear magnetic spin structure. Thus ferroelectricity in these materials is because of magnetic ordering of material. $TbMnO_3$ and $YbMn_2O_5$ etc are the examples for type 2 multiferroics.

1.7.2. Single Phase Multiferroics

Single-phase multiferroics are classified into four types by Fiebig as follows [15].

1. Perovskite structure materials (ABO_3 or $A_2B'B''O_6$). The multiferroicity in these materials is because of distortion cubic structure. $BiFeO_3$, ferroelectric, ferroelastic, and antiferromagnetic compounds will come under this catogiry. These compounds have been used in preparing various solid solutions because of its high electric and magnetic ordering at high temperatures.
2. Hexagonal structure materials, the stoichiometric formula of these materials same as that of perovskite materials but crystallize in hexagonal structure. This compounds also exhibits multiferroic properties. The manganites with formula $RMnO_3$ where R = Sc, Y, In, Ho, Er, Tm, Yb, or Lu will comes under these family. These compounds have ferroelectric property with an antiferromagnetic Mn^{3+} sublattice.
3. Boracites ($M_3B_7O_{13}X$) have ferroelectric, ferroelastic antiferromagnets, ordering in it. These compounds also have a weak ferromagnetic moment. The bivalent ions are M = Cr, Mn, Fe, Co, Cu, Ni and the anions, X = Cl, Br, or I. But these materials have ferroelectric T_C > 300 K and magnetic transitions occur below 100 K.

4. BaMF$_4$ (M = Mg, Mn, Fe, Co, Ni, Zn) are ferroelectric, ferroelastic with exclusively antiferromagnetic or weak ferromagnetic ordering. These are having their melting temperature lesser than their Curie temperature. In spite of having multiferroic property these materials cannot be found in many applications due to the temperature range of the coupled phenomena or the nature of the magnetic ordering (i.e. antiferromagnetic).

1.8. Bismuth Manganite ($BiMnO_3$)

Bismuth Manganite ($BiMnO_3$) is one of the multiferroic materials with low-temperature ferromagnetic (below 105 K) and room-temperature ferroelectric characteristics. Magnetization in this compound is caused by the orbital ordering of Mn^{3+} ions [16]. And lone pair electrons of Bi ions are responsible for the observation of ferroelectric polarization. $BiMnO_3$ has a triclinic structure which has a structural phase transition at 450 K to monoclinic structure and then to orthorhombic phase at 770 K, which is a non-ferroelectric phase [17]. In the bulk $BiMnO_3$, multiferroic properties can be seen at 80 K [18]. However, poor resistivity of this material in polycrystalline form limits its practical device applications. Nevertheless, the resistivity of the same can be appreciably improved by making it in thin film form [19].

1.9. Bismuth Ferrite ($BiFeO_3$)

$BiFeO_3$ (BFO) is the only material till date at room temperature to exhibit multiferroic properties. It is the most promising and well-studied material for the device applications. It shows the antiferromagnet nature below T_N ~ 643 K and ferroelectricity below T_C ~ 1143 K [20]. This material exists in a distorted rhombohedral perovskite structure, with polar space group *R3c* [21]. The space group *R3c* allows BFO to exhibit a large value of ferroelectric polarization of ~ 50 $\mu C/cm^2$ and its polarization vector occurs along the [111] direction [22]. Unlike the usual ABO_3 perovskite structures, where B-cation is responsible for the observation of polarization, lone pair Bi ions ($6S^2$) are responsible for the ferroelectricity in $BiFeO_3$ [23]. Also, $BiFeO_3$ possess G-type antiferromagnetism below a Nèel Temperature T_N, that means, each Fe^{+3} ions align with the antiparallel spins of six neighboring Fe all three Cartesian directions.

Sosnowska et al [24] using high resolution neutron diffraction discovered that $BiFeO_3$ has a complex magnetic spiral or helical magnetic structure. This incommensurate cycloid spin structure has a spin periodicity of 62 nm [25]. Due to this spin alignment the spins are not perfectly aligned in anti-parallel direction but canted with some angle. This leads to a net magnetic moment in the $BiFeO_3$ [26]. The spiral

structure of BFO is stable at temperatures below the Curie temperature T_C.

1.9.1. Structure of $BiFeO_3$

It is well established that bulk BFO in its pure phase exhibits rhombohedrally distorted perovskite structure with *R*3*c* polar space group at room temperature. The schematic diagram of the crystal structure is shown in figure 1.12. The rhombohedral unit cell contains two formula units of $BiFeO_3$ arising from neighboring oxygen shifts about (111) axis. This rhombohedral unit cell can also be represented as an equivalent hexagonal cell. The magnetic and electrical properties of the BFO are expressed based on the hexagonal cell. The rhombohedral pseudo-cubic direction $[111]_C$ corresponding to the hexagonal $[001]_h$ direction. The hexagonal unit cell of BFO contains 6 formula units, where Bi^{3+} ion occupies the corner position, Fe^{3+} in the body centered, and O^{2-} in all face centered positions. The corresponding lattice parameters are a = 5.587 Å, b = 5.587 Å and c = 13.867 Å with $\alpha = \beta = 90°$ and $\gamma = 120°$.

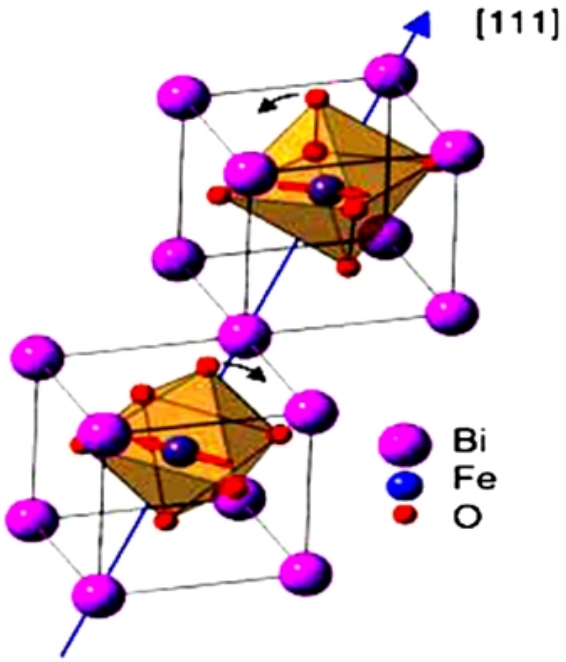

Figure 1.12 Perovskite type structure of $BiFeO_3$ [22]

1.9.2. Electrical and magnetic properties of $BiFeO_3$

In general, ferroelectricity is produced by vacant d^0 orbital but, in $BiFeO_3$, the space group *R3c* allows to exhibit ferroelectricity. The spontaneous polarization grows along [111]c or [001]h direction due to the cooperative displacement of Bi, Fe, and O ions relative to one another along this [111]c axis.

As mentioned above, BFO exhibits G-type anti-ferromagnetism below a Nèel Temperature of 643 K Generally, ferromagnetism is observed due to the availability of partially filled d^n orbitals where in

Fe^{+3} ions are responsible for the ferromagnetism in case of $BiFeO_3$ [1]. The magnetic structure of BFO is discovered by Sosnowska et al using high resolution neutron diffraction. It has a complex magnetic spiral, or helical magnetic structure, which is stable at most temperatures below T_C. In this spin configuration, each Fe^{3+} spin is surrounded by six of the nearest Fe neighbours with opposite spin. Further, this G-type antiferromagnetic structure is modulated by a spiral spin arrangement, whose vector has a wavelength of 620 ± 20 Å.

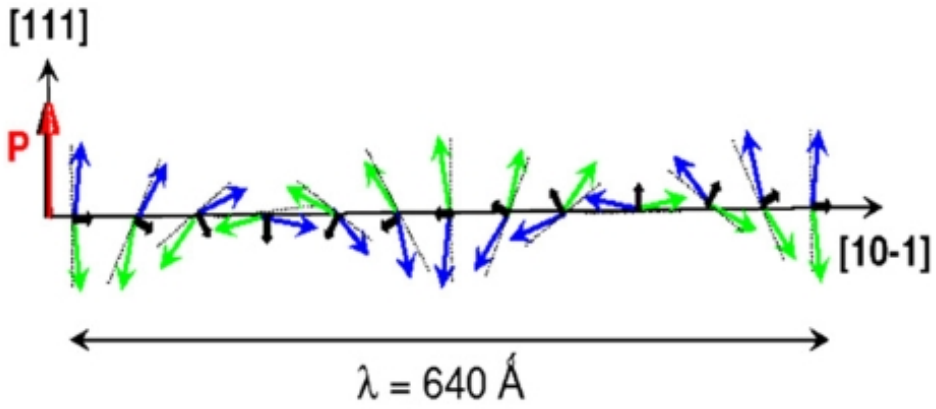

Figure 1.13 Spiral spin arrangement in BFO [26].

1.9.3. Applications of BFO

- Due to multiferroic nature of $BiFeO_3$ it has broad applications in the field of transducers, magnetic field sensors and information storage industry [27].

- The magnetic state is electrically switchable in BFO because the easy plane of its antiferromagnetic domains is correlated with the polar direction. Thus it is a promising candidate for Spintronic applications [28].
- Due to its magnetoelectric coupling, it has the advantage that data can be written electrically and read magnetically. It exploits the best aspects of ferroelectric random-access memory (FeRAM) and magnetic data-storage [29].
- $BiFeO_3$ is interesting to study because it can be used as a lead-free ferroelectric and multiferroics material for nanoscale devices.

1.10. Rare earth doped $BiFeO_3$

Bismuth Ferrite, though a room temperature multiferroic, the observation of magnetoelectric (ME) effect in this system is restricted by its complex spin structure. So, the question about how to derive ferromagnetism in the canted G-type antiferromagnetic order with the space-modulated spin structure is hunted many researchers in recent days. In the past, it is found that the magnetism and ferroelectricity in BFO can be improved by substituting A-site ion with rare-earth ions such as La^{3+}, Sm^{3+}, Gd^{3+}, Eu^{3+}, and Ho^{3+} [30 - 32] or B-site ion doping by transition-metals elements [33 - 34]. In this work, we study the crystal structure, temperature-dependent electrical and magnetic properties of

$Bi_{1-x}RE_xFeO_3$ (RE=La, Gd and Ho, abbreviated as RBFO) bulk ceramic samples are investigated. The upper doping level was fixed at 40 mol% for La, 30 mol% for Gd and 20 mol % for Ho. The RE elements are selected in such a way to see the effect of non-magnetic and magnetic element on the modification of spin structure of BFO. La is larger in ionic radius than Bi whereas the magnetic elements, Gd and Ho are smaller. On the basis of our studies, we show that the structural distortion is a crucial factor in affecting the magnetic properties of BFO material besides its electrical properties.

1.11. Motivation and objective of present work

Multiferroics are the materials in which any two or more of the orders, viz. ferroelectricity, ferromagnetism, and ferroelasticity co-exist in the same phase. These materials are interesting for their underlying rich physics and technologically promising due to potential applications. However, obtaining single phase bismuth ferrite is a challenging task due to volatile nature of bismuth and also the occurrence of secondary phases during the preparation of $BiFeO_3$ [35]. Due to its G-type antiferromagnetism and spin cycloid structure, $BiFeO_3$ has a very low magnetization value. High leakage current and the poor magnetic properties also limit this material from many useful applications. Hence, there is a great need to stabilize the single phase BFO and improve its multiferroic properties for real world applications.

Rare earth elements such as La, Gd, Dy, Eu, Ho etc helps in improving the properties when doped at A-site of ABO_3 type BFO.

There have been many reports on the structural analysis of BFO based on x-ray diffraction (XRD) and neutron measurement. However, there are very few studies probing the structural and Raman properties of RE doped $BiFeO_3$. These investigations can provide useful insight into the enhancement of the ferroelectric properties and cycloid spin modification associated with the variation of bond length and bond angles and also the microscopic properties such as the spin–phonon coupling. Furthermore, there are significant discrepancies among the structural transitions reported on RE doped $BiFeO_3$ ceramics, providing strong motivation for further studies. Besides, there is no clear understanding on the enhancement of the ferroelectric and magnetic properties with RE doping. Hence a systematic study on the structural transitions and the subsequent effect on the multiferroic properties of RE doped $BiFeO_3$ are desirable.

In this work, the crystal structure of $Bi_{1-x}RE_xFeO_3$ (RE = La, Gd and Ho) system is established through an elaborate x-ray diffraction data refinement. RE substitution is expected to affect the structure and multiferroic properties of $BiFeO_3$ host drastically due to the distortion in the crystal. This prompted us to investigate the structural, magnetic and electrical properties with the following objectives in mind.

- The first and foremost aim is to attempt the synthesis of single phase undoped polycrystalline $BiFeO_3$ ceramics using different synthesis routes such as solid state and sol-gel techniques and/or to stabilize the single phase of BFO by RE element substitution.
- Effect of synthesis route on the structural, electrical and magnetic properties of polycrystalline undoped and RE-doped $BiFeO_3$ ceramics.
- The effect of nonmagnetic La^{3+} and magnetic Gd^{3+} and Ho^{3+} ions partially substituting Bi^{3+} ion on the magnetic properties such as H_C, M_r, and transition temperature (T_N).
- Temperature dependent magnetic and electric properties of undoped and RE- doped $BiFeO_3$ (BFO) ceramics to investigate the conduction mechanism.
- The effect of La and Gd co-doping is interesting to see the synergy it brings to the crystal structure and also to understand the role of each element in improving the physical properties of BFO.

1.12. Organization of the thesis

Chapter-1

In this chapter, a brief introduction to the multiferroic oxides is presented. Various types of magnetic order and interactions relevant to

this field are outlined. A brief survey of the literature, highlighting the interest in pure and RE doped BFO is made. This chapter concludes with the aim and scope of the thesis.

Chapter - 2

In this chapter, the details of preparation and various experiments carried out in this dissertation are explained.

Chapter - 3

Chapter 3 is divided into two parts. Chapter 3(a) describes the synthesis, structural, microstructure, and multiferroic characterization of BiFeO3 prepared using solid state and sol-gel methods without any doping. Chapter 3(b) presents the effect of La substitution on the structural and multiferroic properties of Sol-gel prepared bismuth ferrite. $BiFeO_3$ samples were prepared through Solid State (SS) reaction and Sol-Gel (SG) method. Using the Reitveld refinement, the rhombohedral crystal structure with space group R3c is established and the structural parameters for the samples prepared under different synthesis routes are calculated**.** Using Field Emission Scanning Electron Microscope (FE-SEM), particle morphology is viewed and with combined attachment composition analysis (EDS) is carried out. Raman studies are also carried out in this system. Dielectric constant of the BFO

for a measured frequency range of 20 Hz - 2 MHz**.** M-H curves and M-T curves are measured on BFO samples**.**

Chapter - 4

In this chapter, we have investigated the effect of rare earth doping on the structural, electric and magnetic properties of solid state reaction prepared BFO, mainly to see how RE element stabilize the phase purity and affect G-type spin cycloid structure in BFO. To understand the variations in the magnetic properties we have taken nonmagnetic and magnetic rare earth elements as dopants.

Chapter - 5

Chapter 5 describes the structural, electric and magnetic properties of La, Gd co-doped $BiFeO_3$ prepared through solid state reaction method. A-site doping of BFO by La stabilizes the perovskite phase, reduces leakage current and enhances the magnetic properties whereas Gd doping improves both electric as well as magnetic properties**.**

Chapter - 6

The sixth chapter presents the major conclusions drawn from the present study and also gives some scope for future work on these systems.

References

[1] Nicola A. Hill, *J. Phys. Chem.* B **104**, 6694 (2000).

[2] W. Buckel, R. Kleiner WILEY-VCH Verlag GmbH & Co. KGaA, Weinheim (2004).

[3] C. M. Hurd, *Cont. Phys*. **23**, 469493 (1982).

[4] Magnetic Materials by Ehsan Hoseinkhani

[5] J. M. D. Coey, *Magnetism and Magnetic Materials*, Cambridge University press (2009).

[6] K. H. J. Buschow and F. R. de Boer, *Physics of Magnetism and Magnetic Materials* Kluwer academic publishers, (2003).

[7] R Skomski, *Simple models of Magnetism*, Oxford University Press (2008).

[8] *Physics and Chemistry of Solids* **4**, 241 (1958).

[9] Stephan Blundell, *Magnetism in Condensed Matter*, Oxford University Press (2001).

[10] A J Dekker, *Solid state physics,* Prentice-Hall (1962).

[11] C. Kittel, *Phys. Rev*. **82**, 729 (1951)

[12] Wagner RW, *Arch Elektech*., **2**, 371 (1914).

[13] Sillars RW, *Inst. Elect Engg*., **80**, 378 (1937).

[14] Kremer, A. Schonhals, *Broadband dielectric spectroscopy* Springer-Verlag Berlin Heidelberg New York (2003).

[15] Manfred Fiebig, *J. Phys. D: Appl. Phys*. **38**, R123 (2005).

[16] H. Chiba, T. Atou, and Y. Syono, *Journal of Solid State Chemistry*, **132**, 139 (1997).

[17] T. Kimura, S. Kawamoto, I. Yamada, M. Azuma, M. Takano, and Y. Tokura, *Physical Review B*, **67**, 1804011 (2003).

[18] A. Moreira Dos Santos, S. Parashar, A. R. Raju, Y. S. Zhao, A. K. Cheetham, and C. N. R. Rao, *Solid State Commun.* **122**, 49 (2002).

[19] W. Eerenstein, *Appl. Phy. Lett.*, **87**, 1 (2005).

[20] J. Wang, J. B. Neaton, H. Zheng, V. Nagarajan, S. B. Ogale, B. Liu, D. Viehland, V. Vaithyanathan, D. G. Schlom, U. V. Waghmare, N. A. Spaldin, K. M. Rabe, M. Wuttig and R. Ramesh, *Science* **299,** 1719 (2003).

[21] C. Michel, J.-M. Moreau, G. D. Achenbach, R. Gerson, and W. J. James, *Solid State Commun.* 7, 701 (1969)

[22] A Lubk, S Gemming, N A Spaldin. *Phys Rev B.* **80**, 104110e7 (2009).

[23] D. Khomskii, *Physics* **2**, 20 (2009).

[24] I. Sosnowska, T. Peterlin-Neumaier, and E. Steichele, *J. Phys. C.* **15**, 4835 (1982).

[25] I Sosnowska, A. K. Zvezdin, *J. Magn. Magn. Mater.* **140**,167(1995).

[26] D. Lebeugle, D. Colson, A. Forget, M. Viret, A.M. Bataille, A. Gukasov, *Phys. Rev. Lett.* **100**, 227602 (2008).

[27] V. E. Wood, A. E. Austin, A. J. Freeman, H. Schmid, *Magnetoelectric Interaction Phenomena in Crystals*, Gordon and Breach, London, (1975).

[28] H. Bea, M. Gajek, M. Bibes, A. Barthelemy, *J. Phys.: Cond. Mat*. **20**, 434231 (2008).

[29] M Brian, B Michael, J Klug, J-C Lin, *Nanoscape* **5**, 95 (2008).

[30] Y Yao, W Liu, Y Chan, Ch Leung, and Ch Mak, *Int. J. Appl. Ceram. Technol*., **8** 1246 (2011).

[31] Y-J Zhang, H-g Zhang, J-h Yin, H-w Zhang, W-q Wang, J-l Chen and G-h Wu, *J. Mag. Mag. Mater.* **322**, 2251 (2010).

[32] M. Azuma, H. Kanda, A.A. Belik, Y. Shimakawa, M. Takano, *J. Phy. Cond. Matt.* **310,** 1177 (2007).

[33] I. S. Dubenko, V. A. Murashov, D. N. Rakov and I. B. Krynetsky, *Phy. Lett. A.* **l58**, 491 (1991).

[34] Y Wang and C-W Nan, *Appl. Phy. Lett.* **89**, 052903 (2006).

[35] M. Valant, A. Anna-Karin, and N. Alford, *Chem. Mater.* **19**, 5431(2007).

Experimental Details and Techniques

2
Chapter

Abstract:–

In this chapter, the details of preparation and various experiments carried out in this dissertation are explained. We also describe different experimental techniques namely; X-ray powder diffraction, micro-Raman spectroscopy, Field emission scanning electron microscope (FESEM) with energy dispersive X-ray absorption spectroscopy (EDS), dielectric measurements, and magnetic measurements that form the basis of the studies presented in this thesis are explained in detail.

2.1. Introduction

The synthesis and characterization of material is the first and foremost important step during the experimental research in condensed matter physics and materials science. The quality of samples depends to a great extent on the synthesis methods used. In addition, the proper selection of synthesis parameters helps to obtain desired properties in the samples to be characterized along with desired potentials. Structure, surface morphology, grain growth, dielectric and magnetic properties depend on material synthesis. The present chapter gives a brief introduction to different sample synthesis routes, X-ray powder diffraction, Raman measurements, FE-SEM with EDS, Dielectric and Magnetic measurement techniques and also basis of Rietveld analysis of the XRD data.

2.2. Preparation and characterization techniques for ceramic samples

This section deals with the different preparation and characterization techniques used for $BiFeO_3$ ceramic samples. Since this material has to be characterized for its dielectric and magnetic properties, it has to be prepared in a regular geometry with the highest possible densification. This being a ceramic oxide material, the available methods for its preparation are (a) Solid-state reaction method (or ceramic method) (b) Chemical methods like sol-gel, co-precipitation,

hydrothermal etc, and (c) Mechanical methods [1-3]. Of these, the methods used for preparation of bulk $BiFeO_3$ preparation in this study are the solid-state reaction method and sol-gel reaction technique.

2.2.1. Solid-state reaction method

Ceramics are polycrystalline materials having fine crystalline grains and imperfections like grain boundaries, impurities segregated in the grains and grain boundaries, pores etc. In general, they are brittle thus, shaping and densifying them without cracks and deformation is a challenge. The solid-state reaction method is used for forming $BiFeO_3$ and RE-substituted $BiFeO_3$ compositions from the precursor reagents. The shaping and densification are separate processes, which are described in subsequent sections.

The conventional solid state reaction method involves the following steps: (a) Uniform mixing of the initial reagents and (b) Phase formation of the required compound at a high temperature, which is called the calcination temperature. The main disadvantage of this method is that it needs high processing temperatures to achieve the best properties. This process increases the particle size and also causes the loss of bismuth which eventually leads to the formation of secondary phases. But cost effectiveness and simplicity are the major advantages of this process.

Raw materials Bi_2O_3, RE_2O_3 (RE = La, Gd and Ho), and Fe_2O_3, of purity ~ 99.9% from Aldrich Chemicals were used as the starting reagents to attain control over impurities in the product and to maintain reproducibility in properties. An electronic balance (citizen) is used to weigh the reagents, which has an accuracy of up to 0.001 mg.

The individual reagents are mixed homogenously in order to increase the reactivity and the point of contact between the reagents with a suitable mixing medium. The powders were mixed using a planetary single station ball mill (Retsch PM 100) at 250 rpm for about 10 hours in a Tungsten carbide (WC) jar with different diameters of Tungsten carbide balls (3, 5 and 10 mm diameter). Ethanol was used as the grinding medium.

a. Calcination stage

Calcination is a process of the solid-state, where diffusion controlled chemical reaction between the initial reactants result in the desired phase formation. It is the intermediate heat treatment at lower temperatures prior to sintering. Calcination could involve chemical decomposition reactions in which solid reactants are heated to produce a new solid phase and remove the gases which are commonly associated with the initial metal oxide compounds such as carbonates, hydroxides, nitrides, sulphates, acetates and other metal salts. The parameters of the

calcination stage such as temperature, duration of heating and atmosphere are important factors influencing shrinkage during sintering. In the present case, the reagents being oxides, they do not undergo any decomposition. All the mixed reagents used in the present study were calcined at 820°C for 30min to form the required composition and the phase formation was maintained by XRD.

b. Particle size reduction

The particle size reduction (milling) of the complex oxides after the calcination stage is important to homogenize the formed phase. It is well known that the smaller initial particle size reduces the sintering temperature and enhances the density of the ceramics. Planetary ball mills are generally used for milling the powders to achieve particle size reduction.

There are several processing variables that determine the finite size of the particles after milling process, such as type of mill, vial, milling speed, milling time, milling medium and ball to powder ratio [4]. In the present study, Retsch PM 100 single station planetary ball mill (figure 2.1) was used to achieve the initial stoichiometric mixing before the calcination and to reduce the particle size of the calcined powders (250 rpm for 4 hours). A 250 ml Tungsten carbide vial with Tungsten carbide balls having different diameters (3, 5 and 10 mm) are used. All

the processing conditions were optimized to achieve finite particle sizes. In the milling process, the particle experiences the mechanical stresses at their contact points due to compression, shear with the milling medium or with other particles. The mechanical stresses lead elastic and inelastic deformation. If the stress is exceeding the ultimate strength of the particle then it will result in fracture of the particles.

Figure 2.1 Schematic diagram for Retsch ball mill system

c. Uniaxial pressing

After reducing the particle size of the calcined powder, the fine powder is compacted into cylindrical pellets by uniaxial pressing. The compaction of the powder should be done slowly to facilitate the escape of the entrapped air. To make the good pellets of the ceramic powder, a

rigid rust free dye is needed. To make the inner walls of the die smooth, stearic acid is used as an internal lubricant. The pressure gradient on the die as a function of the distance from the upper punch is given by the equation

$$P_x = P_a e^{-4\mu KL/D} \qquad (2.1)$$

Where, μ is the coefficient of friction, P_a is the applied pressure, L is the length and D is the diameter of the dye and K is a constant [5].

d. Solid-state sintering

In ceramics, porosity is an important parameter which governs many of its properties. For maximizing properties such as the dielectric constant, electric polarization, mechanical strength, and thermal conductivity, it is desirable to eliminate as much of porosity as possible. The purpose of sintering is the reduction of porosity in the compact process. The development of microstructure and densification during sintering is a direct consequence of mass transport through several possible paths and one of these paths is usually predominant at any given stage of sintering [5]. In the present study, all the samples were sintered at a temperature range of 800 °C for 4 hrs.

2.2.2. Sol- Gel reaction method

This is an inorganic route, where in ceramics are prepared using metal salts dissolved in an aqueous solution (chloride, oxychloride, nitrate, etc). This is generally treated as a room temperature liquid phase reaction route to produce ceramic materials. The sol-gel synthesis involves two different steps. In the first stage, a colloidal suspension of particles is formed in a liquid medium, which is referred as sol. Second stage involves the formation of gel out of this sol. The particles in the sol react with each other to form the polymeric chains that lead to a three-dimensional structure. When this structure extends to the sides of the container, the material turns rigid, called as gel. When this gel is dried, it forms the powders, called xerogel. Final step involves the calcination of xerogel to form the desired compound.

Simply by changing the initial reaction agents, a variety of final ceramic samples can be formed. Moreover, this technique operates near normal temperature and pressures and thus became an alternative route to synthesize materials that require low temperature synthesis conditions.

2.3. Characterization techniques used for the samples

1. Powder X-Ray Diffraction
2. Raman spectroscopy

3. Field Emission Scanning Electron Microscopy
4. Dielectric properties
5. Ferroelectric properties
6. Magnetic properties

2.3.1. X-ray diffraction (XRD)

X-ray Diffraction (XRD) is a nondestructive technique used to obtain the structural properties of a material. It has a very broad range of applications in physics, material science, geology, mineralogy, ceramics, etc. The applications include the type and quantities of phases present in the sample (phase analysis), the crystallographic unit cell and crystal structure, crystallographic texture, crystallite size, macro-stress, micro-strain and also electron radial distribution functions [6]. The powder diffraction is characteristic of the substance and forms a sort of fingerprint [7] of the substance and yields a great deal of structural information about the crystalline materials. Powder diffraction method involves the diffraction of monochromatic x-rays by a powder specimen. Monochromatic usually means a strong Kα characteristic component of the filtered radiation from x-ray tube operated above the Kα excitation potential of the target material. Figure 2.2 shows INEL x-ray diffractometer with Co target x–ray tube is used to do x-ray diffraction

measurements. Position Sensitive Detector (PSD) filled with P10-gas (10 % methane in Argon) is employed to record the counts.

The peaks of the x-ray diffraction pattern of known as synthesized powder samples are compared with the available standard data for the confirmation of the crystal structure. For comparison, many standards are available [8], some of which are Willars Hand book; Joint Committee on Powder Diffraction Standards (JCPDS) Pcpdf win and National Bureau of Standards.

If the material under investigation is crystalline, then well-defined peaks will be observed while non crystalline or amorphous systems show broad instead of well-defined peaks.

2.3.1.1. Principle

Consider a beam of X-rays of wavelength λ, incidents on the crystal at an angle θ to the atomic planes. In Bragg's law, the interaction between X-rays and the electrons of the atoms is visualized as a process of reflection of X-rays from a stack of parallel equidistant atomic planes. This is an equivalent description of the diffraction effects produced by a three-dimensional grating. The atomic planes are considered to be semi-transparent; that is, they allow a part of the x-ray to pass through and reflect the other part, the incident angle θ (called the Bragg angle) being equal to the reflected angle. Referring to figure 2.3, there is a path

difference between the x-rays reflected from plane 1 and the adjacent plane 2 in the crystal. The condition where the reflected beams interfere positively to give a strong diffracted beam is represented by Bragg's law and is given by $2d \sin\theta = n\lambda$, where n is the integral number describing the order of reflection, λ is the wavelength of X –rays, d is the inter planar spacing and θ is the Bragg angle at which a maximum in diffracted intensity occurs.

Figure 2.2 INEL X-ray diffractometer.

In X-ray diffraction, the line broadening is caused by small crystallite size; the crystallite size can be estimated from the Scherrer's equation.

$$D = k\lambda / \beta \cos\theta \qquad (2.2)$$

where θ is the Bragg angle, λ is the wavelength of the X-rays, d is the mean dimension of the crystallite size composing the powder sample, β

is the full width at half maximum of the pure diffraction profile on the 2θ scale in radians, k is a constant. In the determination of particle size by this method, it must be realized that the instrumental effects might also increase the width of reflection and correction for instrumental broadening must be applied. This method can be used for the determination of size of small crystals.

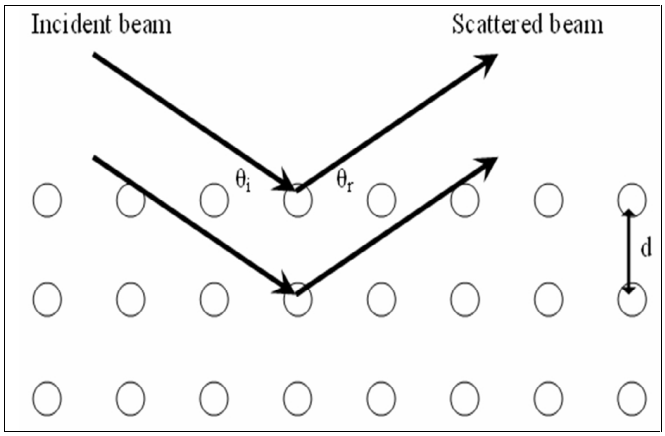

Figure 2.3 Bragg diffraction of X-rays from a lattice

2.3.1.2 Rietveld Analysis

Rietveld method is a very useful tool to refine the x-ray powder diffraction data. This is a computational fitting procedure based upon the least squares refinement of parameters. These user defined parameters represent a structural model that has contribution from crystal structure, the diffraction peak profile, the diffraction optics and

the instrumental factors. To refine a given data successfully, all the above parameters are to be refined.

The least squares residual, S, which is to be minimized, is defined as

$$S_y = \sum_i w_i \left(y_i - y_{ci}\right)^2 \qquad (2.3)$$

Where y_i is the observed intensity at the i^{th} step of the diffraction pattern, y_{ci} is the calculated intensity at the i^{th} step and $w_i = 1$. The calculated intensity, y_{ci} is determined using the following equation

$$y_{ci} = s\sum_K L_K \left|F_K\right|^2 \phi(2\theta_i - 2\theta_K) P_K A + y_{bi} \qquad (2.4)$$

where 's' is the scale factor, K denotes a given Bragg reflection (h k l), L_K contains the Lorentz, polarization and multiplicity factors, ϕ is the reflection profile function, P_K is the preferential orientation function, A is the absorption factor, F_K is the structure factor of the K^{th} Bragg reflection and y_{bi} is the background intensity.

The least squares refinement is performed by finding the partial derivatives of y_{ci} as a function of each parameter. This non-linear calculation is solved through an iterative procedure to get a best fit. And to avoid a divergent solution, a good initial guess for the model is essential. Therefore, Rietveld analysis is not a structure solution algorithm, but only a structural refinement procedure. It is also possible

to model and fit a number of different phases, simultaneously. In this way impurity, presence of secondary phases or instrumental anomalies can be quantified.

The Rietveld refinement uses a number of R factors [9-11] given in equations 2.5 to 2.7 to give an indication of how reliable the fit of the model is to the data once S has been minimized. Amongst a number of software packages that implement Rietveld analysis, we employ the TOPAS package [12] to analyze the x-ray powder diffraction data presented in Chapter 3.

$$R_p = 100 \frac{\sum_i |y_i - y_c|}{\sum_i y_i} \qquad (2.5)$$

$$R_{wp} = 100 \left[\frac{\sum_i w_i |y_i - y_c|^2}{w_i \sum_i y_i^2} \right]^{1/2} \qquad (2.6)$$

$$R_e = \left[\frac{N - P}{w_i \sum y_i} \right]^{1/2} \qquad (2.7)$$

where R_p is R- pattern, R_{wp} is R-weighted pattern, R_e is R-expected. N is the number of observations, P is the number of adjusted parameters and w_i is the observation weight.

2.3.2. Raman spectroscopy

Raman scattering is a nondestructive technique and it do not need any special sample preparation techniques. The main difficulty of Raman spectroscopy is separating the weak inelastically scattered light from the intense Rayleigh scattered laser light. Historically, Raman spectrometers used holographic grating and multiple dispersion stages to achieve a high degree of laser rejection. In the past, photomultipliers were the detectors of choice for dispersive Raman setups, which resulted in long acquisition times. However, modern instrumentation almost universally employs notch or edge filters for laser rejection. Schematic setup of the confocal Raman spectrometer is shown in figure 2.4. Many organic and inorganic, materials are suitable for Raman spectroscopic analysis, and it is finger print technique. These can be solids, liquids, polymers or vapors.

We investigated Raman peaks of ceramics using HR 800 Horiba Jobin Yvon confocal micro-Raman spectrometer equipped with grating having 1800 groves/mm and is shown in figure 2.5. It consists of three excitation laser sources. He:Ne laser, which provides 632 nm wavelength, Argon ion laser, which provides 514 nm, and diode laser, which provide 785 nm wavelengths. In the present study, 514 nm is used to investigate the vibrational modes. The detecting system is CCD.

A notch filter is used in the HR 800 for the rejection of the exciting line. It is specific for one wavelength, and it is changed with excitation wavelength source is changed. A joy stick is provided to position the sample exactly under the illumination spot. Furthermore, the sample holder is placed on a XY stage so that Raman mapping can be carried out for different places of the sample.

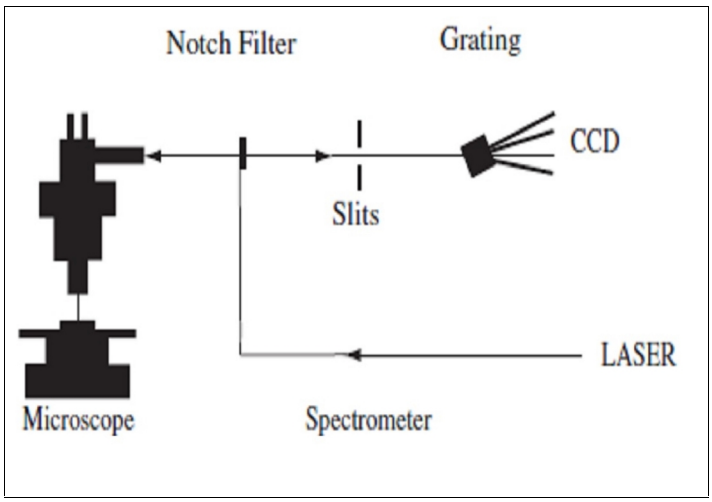

Figure 2.4 Schematic setup of confocal Raman spectrometer

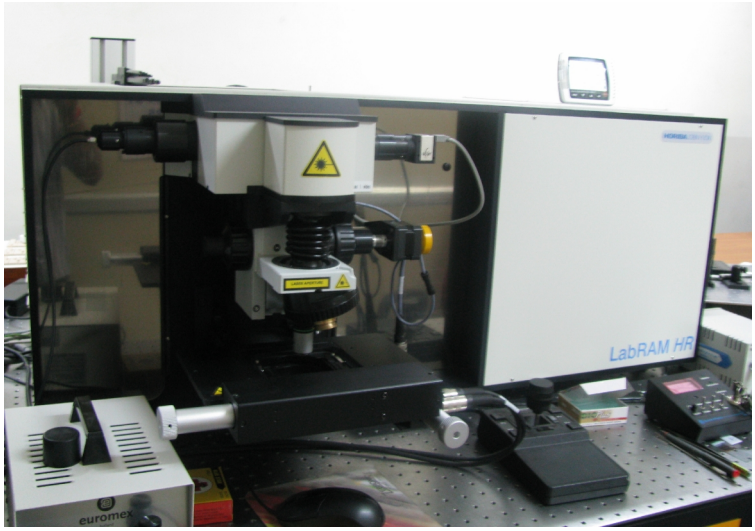

Figure 2.5 HR 800 Horiba Jobin Yvon confocal micro-Raman spectrometer

2.3.3. Field Emission-Scanning Electron Microscopy (FE-SEM)

Microscopy involves the study of objects that are too small to be examined by the unaided eye. In the SI (metric) system of units, the sizes of these objects are expressed in terms of sub-multiples of the meter, such as the micrometer (1 μm = 10^{-6} m, also called a micron) and also the nanometer (1 nm = 10^{-9} m). There are many types of microscopes, the most common and first to be invented is the optical microscope which uses light or electrons to image the sample [13].

The grain size and surface morphology of the powder samples were investigated using Carl-Zeiss FESEM, model of Supra 40 VP (figure 2.6). In this model combined with GEMINI- FESEM column with

beam booster comprises of three direct detection systems; In-lens SE detector for high contrast topography, In-column EsB detector for low KV ultra-high resolution material contrast and integrated annular AsB detector for compositional imaging. FE-SEM uses a field emission source producing a cleaner image with a spatial resolution < 2 nm.

Figure 2.6 Field emission scanning electron microscope

The electrons generated by the Field emission source under the vacuum are accelerated in a field gradient and passes through electromagnetic lenses. This beam focuses and bombards on to the specimen resulting secondary electrons, back scattered electrons, auger electrons and others which are collected by the detector. The image of the sample surface is constructed by comparing the intensity of these

secondary electrons to the primary electron beam and this is displayed on the monitor.

The schematic diagram of field emission scanning electron microscopy is shown in the figure 2.7. FE-SEM operates always under high vacuum (less than $1x10^{-7}$ Pa), which prevents electron scattering and discharges inside the instrument. The field emission electron Gun consists of an emitter usually a Tungsten (W) wire fashioned into a sharp point of radius ~ 100 nm so that the electric field can be concentrated to an extreme level.

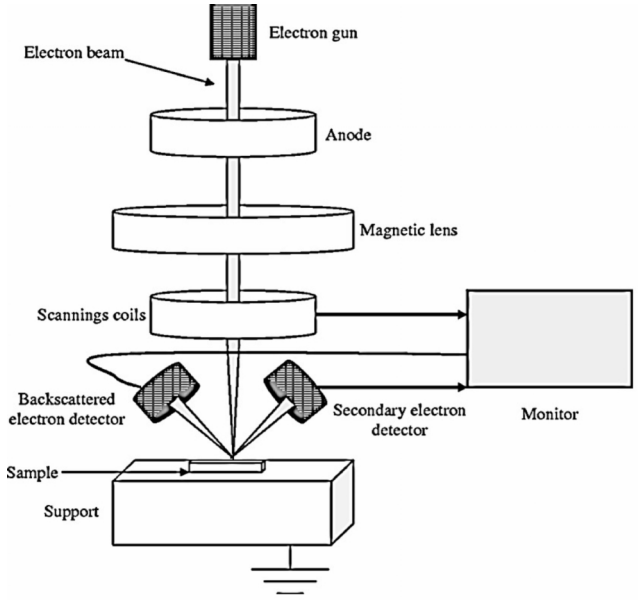

Figure 2.7. Schematic diagram of field emission scanning electron microscopy.

This emitter is held at several kilovolts (1~30 KV) negative potential relative to a nearby electrode, so that there is sufficient potential gradient at the emitter surface to cause field electron emission. A high energy (10-30 keV) electron beam, emitted from a tungsten tip is condensed to a spot diameter of 1-5 nm using electromagnetic lenses. The pair of scanning coils deflect the electron beam over the sample surface. This incident primary electron beam bombards the sample and cause low energy secondary electrons generation, which originates within a few nanometers from the surface.

The secondary electrons emitted from the sample are detected by a scintillator-photomultiplier device and signal is modified into a two-dimensional intensity distribution that can be viewed and saved as a digital image in a monitor. There are the high-energy electrons called as back scattered electrons, which are elastically scattered and essentially possess the same energy as the incident electrons. These are used to detect contrast between zones with different chemical compositions as they are emitted from a depth in the sample. For specimen with poor electrical conductivity, a negative charge builds up gradually from bombardment by the high-energy electron beam. An abnormal contrast and splitting of the image result from the uneven distribution of the negative charge on the sample. A simple solution is to coat a very thin (generally 10-20 nm thick) gold layer on the sample's surface. It can

enhance the emission of secondary and backscattered electron, reduction of thermal damages as well as the elimination of charge accumulating effect.

a. Sample preparation

In the process of SEM imaging, electrons hit the sample and if the sample is insulator, the sample may exhibit a phenomenon called "charging." To overcome this problem, samples can be prepared by coating them with a conducting material. In the present work, samples were coated with Gd-Pd, using an SPI Sputter Coater.

b. X-Ray spectral measurement via electron dispersive spectrometer (EDS)

Energy Dispersive Absorption of x-rays (EDS) or Energy Dispersive x-ray analysis (EDS) is a method used to determine the energy spectrum of x-ray radiation emitted by a sample. It is a technique used for identifying the elemental composition of the specimen in an area of interest thereof. The EDS attachment works as an integrated feature of a Field emission scanning electron microscope (FE-SEM), and cannot operate, on its own, without the FE-SEM. In addition, elemental analysis can be possible in two different ways. Based on energy called EDS and wavelength (WDS) up to the element Boron one can determine using this probe.

2.3.4. Dielectric properties

The low frequency dielectric spectroscopy is emerging as an important material characterization tool [14]. The low frequency dielectric measurements are unequaled in their ability to dynamically monitor the many physical and chemical processes important in the investigation of new materials such as polymerization, phase transition and diffusion. The conventional way for making the low frequency measurement (below < 10 MHz) of the dielectric properties of solids is to place a sample between closely spaced parallel conducting plates and monitor the AC equivalent capacitance $C_{(\omega)}$ and the dissipation factor (also known as the loss tangent) $D_{(\omega)}$ of the resulting capacitor [15]. Normally one has to design the plate spacing to be much less than the plate size as this serves to minimize the effect of the fringing field. The material under test in the parallel plate configuration can be modeled as a frequency dependent capacitance $C_{(\omega)}$ in parallel with a frequency independent resistor R_0. The DC resistance R_0 takes into account processes such as tunneling of thermally activated hopping and ionic conduction. The capacitance $C_{(\omega)}$ is proportional to the complex dielectric function of the material under test which can be represented as follows,

$$\varepsilon_{(\omega)} = \varepsilon_{r(\omega)} - j\varepsilon''_{(\omega)} \qquad (2.8)$$

The capacitance $C_{(\omega)}$ can be measured by a typical capacitance bridge which can be used to calculate the real part of the complex dielectric function $\varepsilon'_{(\omega)}$.

$$C_{(\omega)} = \frac{\varepsilon_{r(\omega)}\varepsilon_0 A}{d} \qquad (2.9)$$

Here, A is the cross section area of the capacitor, d is the separation between the plates and ε_0 = 8.85 x10^{-12} F/m is the absolute permittivity of free space. The other measured quantity, the dissipation factor (the loss tangent) given by

$$D_{(\omega)} = \frac{\varepsilon''_{(\omega)}}{\varepsilon_{r(\omega)}} + \frac{d}{\omega \cdot \varepsilon_0 \cdot \varepsilon'_{(\omega)} \cdot A \cdot R_0} \qquad (2.10)$$

and can be used to extract the imaginary part of the dielectric function, $\varepsilon''_{(\omega)}$.

For the dielectric measurement, silver paint was applied on both sides of the pressed pellets and cured. The samples were fixed in the spring loaded sample holder attached to a heating chamber. The parallel capacitance (C) and the dissipation factor (D) for all the samples were measured using an Agilent E4980A impedance analyzer in the frequency range of 20 Hz – 2 MHz in a temperature range of 50 to 500 ^{o}C with a temperature control unit. The temperature and measurement process were controlled electronically by a lab made programme using

lab view software. The temperature was maintained with an accuracy of ±1 °C.

2.3.5. Ferroelectric properties

The ferroelectric behavior in a given material can be identified by polarization reversal, i.e. ferroelectric switching. The polarization reversal can be studied by recording the hysteresis loop (P-E loop) using Sawyer-Tower circuit [16]. The principle for measuring hysteresis loops is based on Sawyer-Tower circuit, shown in figure 2.8.

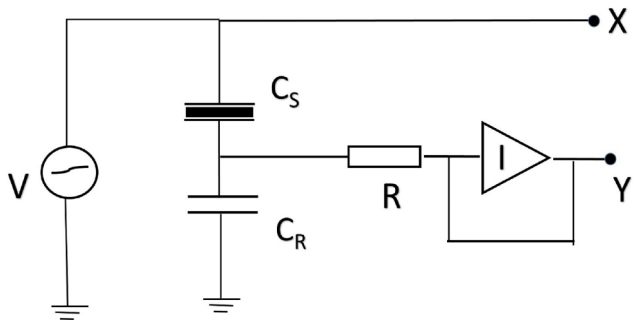

Figure 2.8. Schematic representation of Sawyer-Tower circuit.

In the circuit, the C_S stands for the ferroelectric sample in capacitor geometry, C_R represents the reference capacitor and 'I' represents the integrated circuit. Since the C_S and C_R are in series, the same amount of charge is stored in both the capacitors. The charge can be measured as

$$Q = C_S V_S = C_R V_R$$

$$V_R = Q/C_R$$

This voltage is given as X channel to the CRO, which measures the applied electirc field given by the relation,

$$E = V_i/d \qquad (2.11)$$

The displacement is equal to the surface charge density D = Q/A, where A is the area of the parallel plate capacitor. We can express the displacement vector as follows,

$$D = V_y C_R/A$$

Further, the polarization and displacement vectoor are related as $D = \varepsilon_0 E + P$, in this case $\varepsilon_0 E << P$, the polarization can be expressed as

$$P = V_y C_R/A \qquad (2.12)$$

This is taken as input to Y-axis of CRO. Hence, with varying applied field, the polarization of the sample is measured. The typical P-E loop is shown in schematic diagram (figure 2.10).

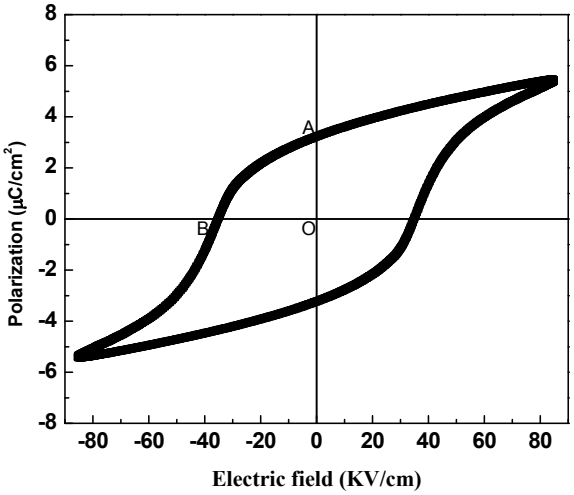

Figure 2.9 Schematic diagram of P-E hysteresis loop.

The hysteresis loop shown in figure 2.10 gives information about the remnant polarization which a material possesses when the applied field is zero. The length OA represents the remnant polarization (P_r) and OB represents the minimum filed required to reverse the direction of polarization i.e coercive field (E_C). The shape of the loop is affected by number of factors such as dimensions of the sample, thermal and electrical treatment of the sample, humidity, temperature and crystal symmetry.

In the present study, the polarization vs. electric field loop is traced by using a computer controlled standardized ferroelectric test system with a maximum operating voltage limit of 4KV built using the Sawyer-Tower circuit.

Figure 2.10 Automated P-E loop set up.

2.3.6. Magnetic properties

2.3.6.1. Physical Property Measurement System (PPMS)

Magnetization, and AC Susceptibility measurement is carried out using PPMS-6000 with a maximum field of 9T (Quantum Design) attached with vibrating sample magnetometer (VSM), AC measurement system (ACMS) and oven options. The principle and operation of each technique will be discussed one by one [17].

a. Vibrating Sample Magnetometer (VSM)

The VSM option for the PPMS (Quantum design, U.S.A) consists primarily of a VSM linear motor transport (head) for vibrating the sample; a coil set puck for detection, electronics for driving the linear motor transport and detecting the response from the pickup coils. The basic measurement is accomplished by oscillating the sample near a detection (pickup) coil and synchronously detecting the voltage induced

from sample. The system is able to resolve magnetization changes even less than 10^{-6} emu.

The basic principle of operation for a vibrating sample magnetometer is a changing magnetic flux induces a voltage in a pickup coil. The time-dependent induced voltage is given by the following equation

$$\begin{aligned} V_{coil} &= d\Phi / dt \\ &= \left(d\Phi / dz\right)\left(dz / dt\right) \end{aligned} \qquad (2.13)$$

In equation (2.13), Φ is the magnetic flux enclosed by the pickup coil, *z* is the vertical position of the sample with respect to the coil, and *t* is time. For a sinusoidally oscillating sample position, the voltage is based on the following equation

$$V_{coil} = 2\pi f C m A \sin(2\pi f t) \qquad (2.14)$$

In equation (2.14), *C* is a coupling constant, m is the DC magnetic moment of the sample, *A* is the amplitude of oscillation, and f is the frequency of oscillation. The acquisition of magnetic moment measurements involves measuring the coefficient of the sinusoidal voltage response from the detection coil.

b. ac Measurement System (ACMS)

The ACMS option has possibility to be used as either a DC magnetometer or an AC susceptometer. The ACMS contains an AC-drive coil set that provides an alternating excitation field and a detection coil set that inductively responds to the combined sample moment and excitation field. The copper drive and detection coils are situated within the ACMS insert, concentric with the superconducting DC magnet of the PPMS. The drive coil is wound longitudinally around the detection coil set. The field amplitude that can be applied depends on the frequency of the alternating field and the temperature within the PPMS probe, but, at any temperature, the drive coil can generate alternating fields of up to ±10 Oe in a frequency range of 10 Hz to 10 kHz. Both the amplitude and phase of this response are reported. Alternatively, the ACMS can report the in-phase and quadrature components of the sample's response. The dynamic or ac susceptibility χ_{ac} = dM/dH, where dM is amplitude of change in magnetic moment and dH the amplitude of alternating field.

c. High Temperature Magnetic measurements

Sensitive D.C magnetometry measurements in the temperature range 300 K - 800 K were performed on PPMS VSM with Oven option [18]. VSM Oven vibrates the heater stick inside the VSM detection coil set. Heater stick is a specially designed heated sample holder that

connects to VSM sample holder with electrical feed through and contains a one gram heated substrate on which the sample is glued using alumina - based cement to maximize thermal contact. Platinum resistive heater element is lithographically patterned onto the sample holder. Platinum heater region is wrapped securely with in a copper – foil radiation shielded that retains heat and reduces thermal gradients between the sample and heater stick.

Heating of the sample is achieved by applying current to platinum resistive heating element. A thermocouple embedded on the backside of the sample holder measures the temperature in the sample region, and a thermistor at the top connector of the sample holder corrects for heating of the cold junction. Due to the low thermal mass of the heated substrate heating rates of +200 K/min at the sample can be maintained throughout the full temperature range of the oven. Cooling rate will depend on the current temperature of the heater stick and occurs through thermal radiation from the heater stick to the VSM detection coil set.

References

[1] M. N. Rahaman, (Marcel Dekker, Inc, New York) 2003.

[2] D. Seagal, (Cambridge University Press, Cambridge) 1991.

[3] R. E. Carter, *J. Chem. Phys.* **34**, 2010 (1961).

[4] C. Suryanarayana, *Progress in Mater. Sci.* **46**, 1 (2001).

[5] S J. Kang (Elsevier, Amesterdam) 2002

[6] D. Cullity, (Addision-Wesley, Reading, MA) 1956.

[7] B. D. Cullity, Elements of X-ray Diffraction (Ind. Ed.) (Addison-Wesley, 1977).

[8] Theo Hahn, International Tables for Crystallography, Volume A: Space-Group Symmetry, Published for The International Union of Crystallography by Springer (2005).

[9] H. M. Rietveld, *J. Appl. Crystallo gr*. **2**, 65 (1969).

[10] R. A. Young, the Rietveld Method, Oxford IUCr/OUP (1995).

[11] G. Bragon, Neutron Diffraction, Oxford 3rd edition (1989).

[12] Topas 4.2 tutorial DOC-M88-EXX062 V4.2 -01.2009.

[13] R F. Egerton, *Physical Principles of Electron Microscopy*, Springer, 2005.

[14] Helene Hagerstrom, Katarina Edgman, Maria Stromme, *J. Pharma. Sci.* **92**, 1869 (2003).

[15] J. F. Johnson and R. H. Cole, *J. Ame. Che. Soc.* **73**, 4536 (1951)

[16] C. B. Sawyer and C. H. Tower, *Phys. Rev.* **35**, 269 (1930).

[17] PPMS-6000 (Quantum Design) *User's Manual* Part Number 1081-400 C1.

[18] PPMS VSM Oven option *User's manual, Rev.* A1, February 2008.

Synthesis and multiferroic properties of $BiFeO_3$ prepared by solid state and sol-gel methods and the effect of La substitution on sol-gel prepared $BiFeO_3$.

3
Chapter

Abstract:–

Preparation of single-phase bismuth ferrite is a challenging task due to narrow synthesis range. It has high leakage current and very poor magnetic properties. Thus, various synthesis methods are attempted to achieve the bismuth ferrite in its single phase. The solid-state method do not avoid all the secondary phases but the volume fraction of them reduces highly by optimized preparation conditions of $BiFeO_3$ (BFO), calcinated at 820 °C for 30 min. Sol-gel route is another synthesis technique in which the minor impurity phases are avoided due to modified reaction conditions. Phase pure BFO powders were obtained at reaction temperature of 250 °C and calcinated at 600 °C for 1 h. Sol-gel samples show an improvement in dielectric and magnetic properties due to the homogeneity. The effect of lanthanum doping on the structure and multiferroic properties of Sol-gel prepared BFO is studied. Lanthanum doping above 20 % results in a structural phase transition from *R3c* to *Pbnm*. The polarization and hence, dielectric constant increases due to the crystal distortion. A Maxwell-Wagner kind of behavior is seen in these samples. A huge improvement in the magnetic properties, especially coercivity suggests that lanthanum doping results in the modification of cyclic spin structure and samples become more anisotropic. The spin glass kind of observation is seen in lanthanum doped samples also. High temperature magnetic measurements reveal that Nèel temperature shifts to the higher temperatures with La doping.

Synthesis of $BiFeO_3$ through solid state and sol-gel methods: a comparative study

3(a)

3.1. Introduction

Among all the multiferroic materials, $BiFeO_3$ (BFO) is the only room temperature (RT) multiferroic, which has a G-type antiferromagnetic order below Nèel temperature, T_N = 643 K and ferroelectric order with Curie temperature, T_C = 1103 K [1]. Because of the simultaneous existence of these two order parameters, the mutual control between them is possible, which has many favourable applications. Presence of impurities results in high leakage current, leading to poor ferroelectric behaviour [2]. Hence, in the present work, first we have focused on the preparation of single phase bismuth ferrite by using different synthesis routes, later the effect of the impurity phase on the physical properties of the BFO is also studied.

3.2. Synthesis of $BiFeO_3$

Bismuth ferrite, being a vastly investigated material, many synthesis procedures are reported to prepare single phase BFO. The preparation of bismuth ferrite in its pure phase is a challenging task, mainly in the

solid-state synthesis due to the following reasons.

1. Bi_2O_3 is an easily volatile material with a melting point of ~ 820 °C , which is close to the crystallization temperature of $BiFeO_3$, resulting in some amount of Bi loss during the calcination at high temperatures.
2. Bi being a metastable can easily forms secondary phases with Fe, such as $Bi_2Fe_4O_9$ and $Bi_{25}FeO_{40}$, etc [3].
3. A very narrow synthesis range of pure BFO in its phase diagram as shown in the figure 3.1.

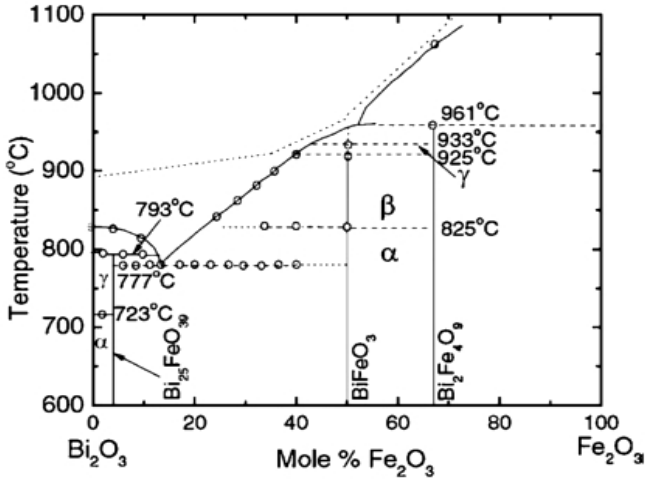

Figure 3.1 Compositional phase diagram of $BiFeO_3$. Figure adopted from Ref. [4]

In order to address the above issues, many approaches are adopted by the researchers, such as 1) adding extra Bi_2O_3, 2) changing the calcination temperature, 3) liquid phase sintering technique and 4) leaching minor phase with HNO_3. Furthermore, apart from the usual

solid-state method, different wet chemical routes such as, hydrothermal [5], sol-gel technique [6, 7], auto combustion [8] and other chemical methods [9, 10] are trailed to reduce the reaction temperature and obtain the pure phase. In the present chapter, the importance of phase purity of BFO is highlighted by making a comparative study between the solid state reaction and sol-gel method prepared systems.

3.2.1. Solid state reaction method

To prepare $BiFeO_3$ by conventional solid state (SS) reaction method, stoichiometric ratios of high purity chemicals Bi_2O_3 (99.9% Aldrich) and Fe_2O_3 (99.9% Aldrich) taken as starting materials, were ground thoroughly in ethanol medium using high energy ball mill for 4 h. The ball milling was carried out in a Retsch single station (PM-100) planetary ball milling system in air. A 125 mL tungsten carbide (WC) vial and tungsten carbide balls with a diameter of 10 mm, 5 mm and 3 mm were used. The milling speed was set at 350 rpm, and it was stopped for every 30 min of milling, for a duration of 2 min to cool down the system, and the balls were rotated in both clockwise and anti-clockwise directions. The mixture was then pre-calcinated at 600 °C for 30 min and ball milled again for 30 min. Later, powders are calcinated at 820 °C for 30 min. Further, pellets of 10 mm diameter and 2 mm thickness were made and sintered at 800 °C for 4 h. The same procedure

is followed for all the solid state prepared samples discussed in the thesis. The flow chart of the synthesis procedure is shown in figure 3.2. These sintered pellets are used for further characterization.

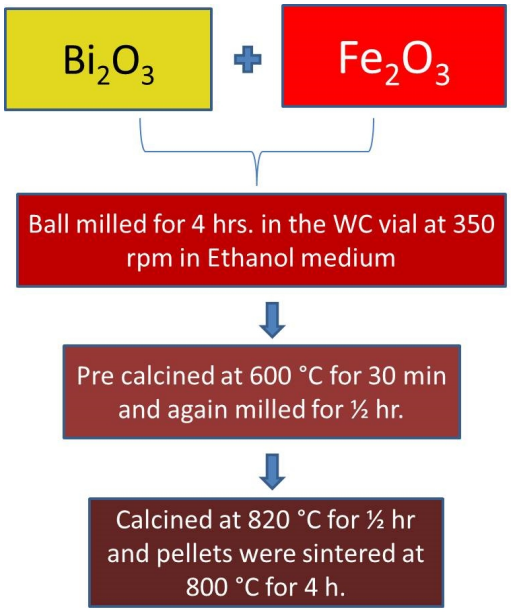

Figure 3.2 Flow chart for the solid-state synthesis reaction method.

3.2.2. Sol-Gel technique

Sol-Gel (SG) technique is another effective method adopted to synthesize pure BFO as it needs low temperatures for the phase formation compared to solid-state route. This helps to avoid the bismuth loss and in turn, reduces the formation of secondary phases. In order to carry out the preparation, the high purity (99.9 %) precursors $Bi(NO_3)_3 \cdot 5H_2O$ and $Fe(NO_3)_3 \cdot 9H_2O$ were taken in a stoichiometric molar

ratio, dissolved in 1:5 HNO_3 solution to form an aqueous solution in separate beakers. This mixture is continuously stirred using a magnetic stirrer for 30 min to form a clear solution. Later, citric acid was added as a chelating agent to the liquid solution and stirred for 2 hours at RT. The solution was heated at 250 °C on a hot plate and subsequently, heated at 600 °C for 1 hour to form the BFO compound. This powder is pressed into pellets and sintered for densification at 750 °C for 4 hours. Figure 3.3 gives the flow chart for the sol-gel synthesis and this is followed for La doped BFO samples also discussed in next section. The pellets were cut into desired geometry for magnetic and electric measurements.

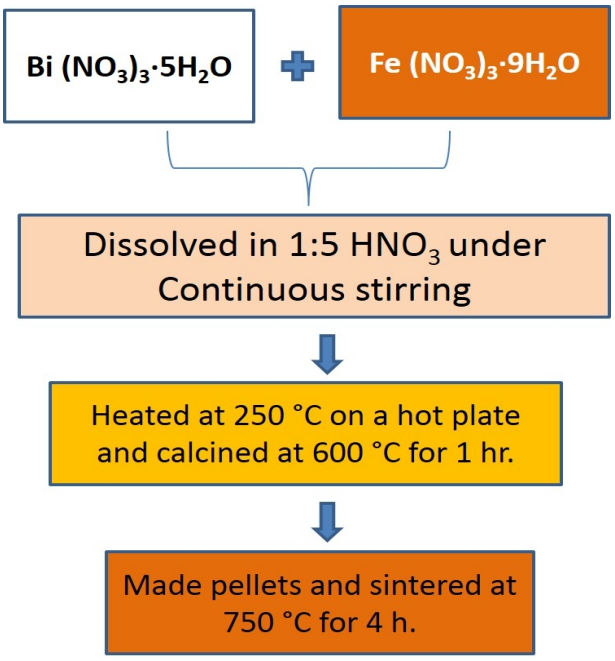

Figure 3.3 Flow chart of sol-gel synthesis reaction

3.3. XRD Analysis

Structural Phase analyses of the samples prepared by both the reaction methods were studied using the room-temperature powder X-ray diffraction (Model: Inel X-Ray (Co Kα) diffractometer). XRD patterns were recorded in 2- Theta range of 10° – 100° in a Bragg-Brenton geometry.

3.3.1. XRD of SS prepared BFO

3.3.1.1. Optimization of calcination temperature

The $BiFeO_3$ samples prepared by solid-state reaction method are calcined at various temperatures to optimize the calcination temperature, time, and the corresponding XRD patterns are shown in the figure.3.4. The calcination temperature reported in literature is ranging from 600 °C to 820 °C [11]. In the present study, it is observed that the BFO phase formation starts from 700 °C. As the temperature increases the percentage of the impurity phase reduces. The prominent peaks in XRD plot of samples calcined at 820 °C (near to the melting point of Bi_2O_3) for 30 min are indexed to various (h k l) planes of BFO, indicating the formation of rhombohedral structured BFO. In addition, peaks corresponding to $Bi_2Fe_4O_9$ and $Bi_{25}FeO_{40}$ impurity phases were also observed with small intensities. However, the impurity phases are

much smaller in comparison to 810 °C. The calcination temperature is restricted to 820 °C, due to bismuth loss at higher temperatures which leads to the increase in formation of secondary phases. Thus, calcination temperature is optimized as 820 °C for 30 min to get the better phase formation.

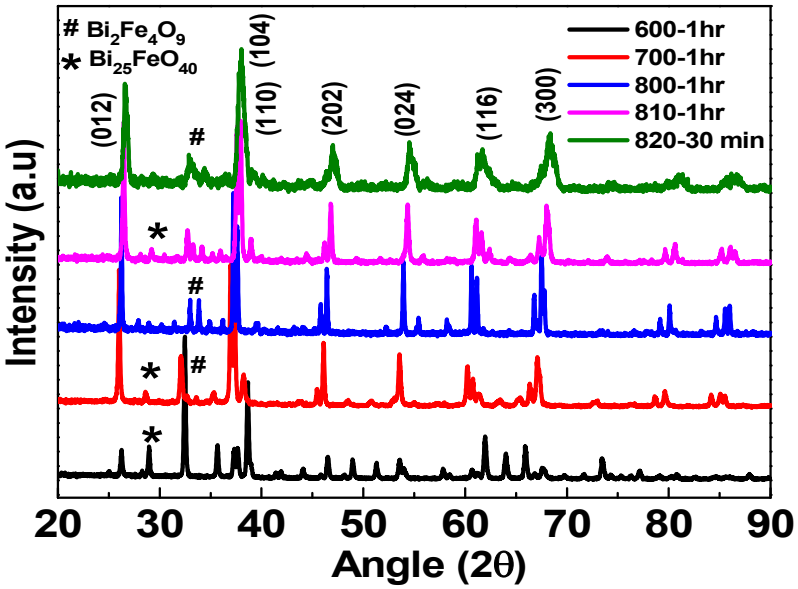

Figure 3.4 XRD pattern of BFO prepared through SS at different calcination temperatures

3.3.1.2. Compensation of bismuth loss

To compensate the bismuth loss, an extra amount of Bi_2O_3 was added to the stoichiometric amounts of precursors to get the single phase of BFO as reported in the literature [12]. However, the percentage

of bismuth loss is arbitrary; one do not have a clear control on how much extra percentage to add since there was no quantitative details of how much bismuth loss occur at high temperatures. Hence, in the present work, 1 - 5 wt % excess Bi_2O_3 are tried and the resulting XRD pattern is shown in the figure 3.5. From the figure, it is very clear that all the samples have the secondary phases in varying proportions with respect to the primary phase of BFO. Even though 2 % excess Bi_2O_3 helps in reducing the fraction of impurities, this method is not very successful in achieving the single phase BFO. Even if single phase is achieved, the reproduction of the same is questionable as any slight change in the reaction parameters would result into secondary phases easily.

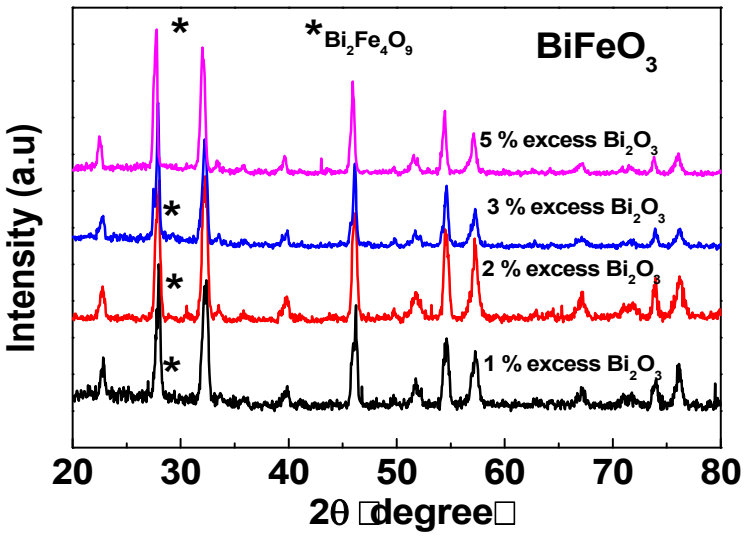

Figure 3.5 XRD pattern of BFO prepared through SS with excess bismuth oxide compositions calcinated at 820 °C for 30 min.

3.3.1.3. Liquid phase sintering

Another popular method implemented by the researchers is the liquid phase sintering, where the reagents are calcined at very high heating rates of (~100 °C/min) above the melting point of Bi_2O_3 for shorter durations [13, 14]. This will help to avoid the formation of secondary phases as the precursors do not have sufficient time for the formation of secondary phases except BFO. In the present study, the samples were calcinated at 880 °C for various durations at a maximum heating rate of 20 °C/min only due to the limitation of the furnace. The XRD pattern calcined in this way are shown in the figure 3.6. From the figure, the sample calcined at 880 °C with duration time of 30 min and 4 min are having many additional peaks other than BFO whereas that prepared at 880 °C with 1 min duration has less impurity peaks. The appearance of these additional phases at larger durations is due to high bismuth loss at higher temperatures. Though this method is successful in the literature [14, 15], in the present study, it is not helpful in getting pure BFO phase due to smaller heating rates.

Leaching is one of the popular methods to dissolve the secondary phases and to get the single-phase BFO for the powders obtained through solid-state synthesis. However, leaching method often results in the coarse powder and a poor reproducibility [16]. Hence this method is excluded in this study.

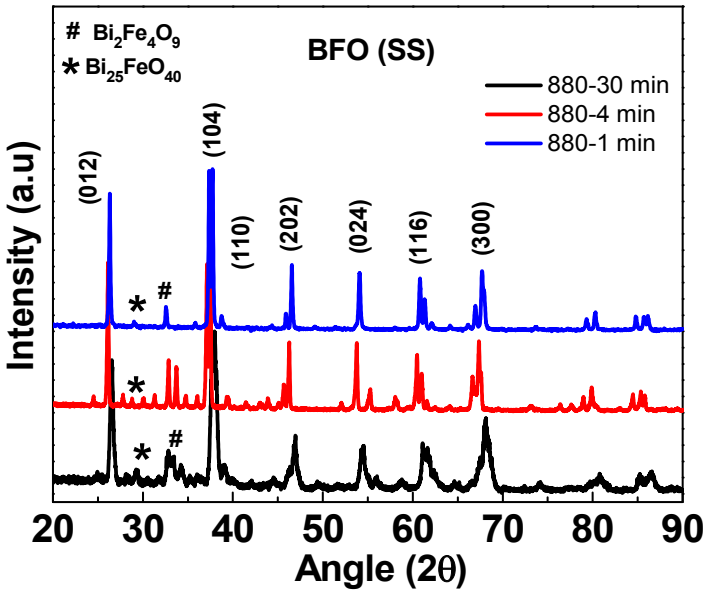

Figure 3.6 XRD pattern of BFO prepared through SS at different rapid heating calcination temperatures

Of all the trails, the samples calcined at 820 °C for 30 min has less impurity phase of $Bi_2Fe_4O_9$, as it is evident from the smaller (4.8 %) peak intensity than others. Therefore, the calcination temperature is restricted to 820 °C with 30 min for all the samples prepared through solid state synthesis in the present study. Figure 3.7 shows the XRD pattern of BFO prepared at 820 °C for 30 min, indexed with the rhombohedral *R*3*c* structure (JCPDS file No. 86-1518).

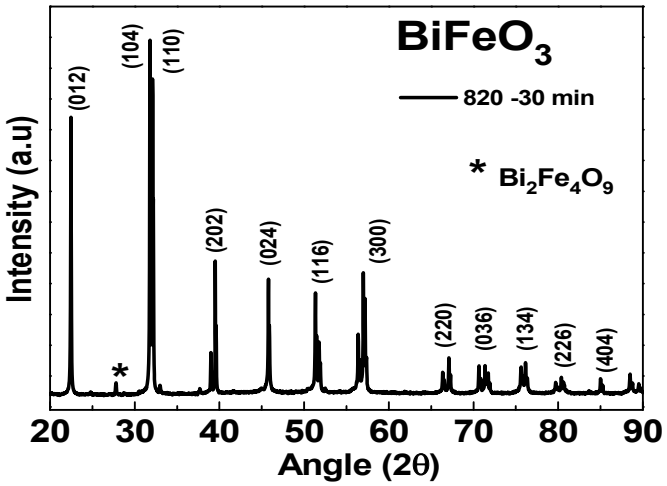

Figure 3.7 XRD pattern of BFO prepared through SS at 820 °C for 30 min

3.3.2. XRD of BFO prepared through sol-gel technique

The single-phase formation through a sol-gel synthesis depends upon the reaction temperature at which the sol is heated to form the gel. The sol formed during this process of reaction is heated at distinctive temperatures to form the gel. Also calcination temperature is another crucial parameter in obtaining the required phase. Hence in this technique, these two parameters are optimized by varying all possible calcination temperatures for every fixed reaction rate and vice versa. XRD studies are carried out on all the samples and only two cases are discussed below.

Figure 3.8 shows the x-ray diffraction plots of sol-gel prepared BFO ceramics at various calcination temperatures for the powders obtained at a fixed reaction temperature of 250 °C. It is observed that

the BFO phase formation occurs from 450 °C and the *R*3*c* phase evolves with an increase in the temperature till 550 °C with a minor impurity phase. When the sample was heat treated at 600 °C for 1 hour, the *R*3*c* phase is completely stabilized and the impurity phases are absent.

To optimize the reaction temperature, the sol is heated in the range of 80 °C to 250 °C. The obtained powders at distinct reaction temperatures are calcinated at a fixed temperature of 600 °C for 1 hour. The corresponding XRD pattern is presented in the figure 3.9. From XRD, the formations of impurity phase are minimized for the powders obtained at a reaction temperature of 200 °C. However, the reaction temperature 250 °C results in the formation of single phase $BiFeO_3$.

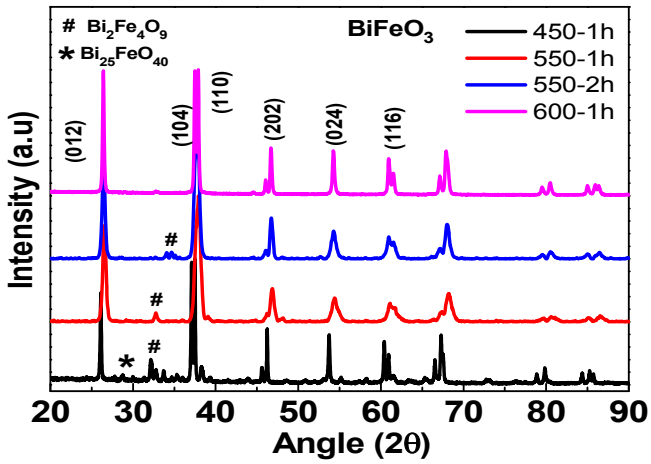

Figure 3.8 XRD pattern of BFO prepared through SG at different calcination temperatures

Therefore, compared to traditional solid-state sintering process, the pure $BiFeO_3$ is formed using sol-gel route at a much lower temperature (600 °C) without formation of any other secondary phases.

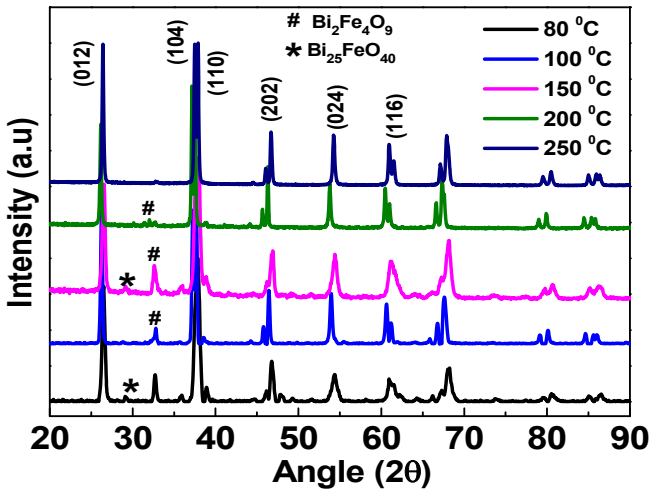

Figure 3.9 XRD pattern of BFO prepared through SG at different reaction temperatures calcinated at 600 °C.

3.4. Rietveld refinement of X-ray results

The x-ray diffraction data were further analyzed by Rietveld refinement method using "TOPAS" software. The Rietveld refinement of the samples processed using SS and SG routes were carried out by considering rhombohedrally distorted perovskite structure with the *R*3*c* space group. We obtained a good refinement with the *R*3*c* symmetry. The good refinements are confirmed by the good statistics that we obtained R_{wp} = 6.81% and R_p = 4.99 % at room temperature. The fittings

thus obtained for BFO are shown in figure 3.10 and corresponding refined lattice parameters, and position coordinates are listed in table 3.1- 3.3.

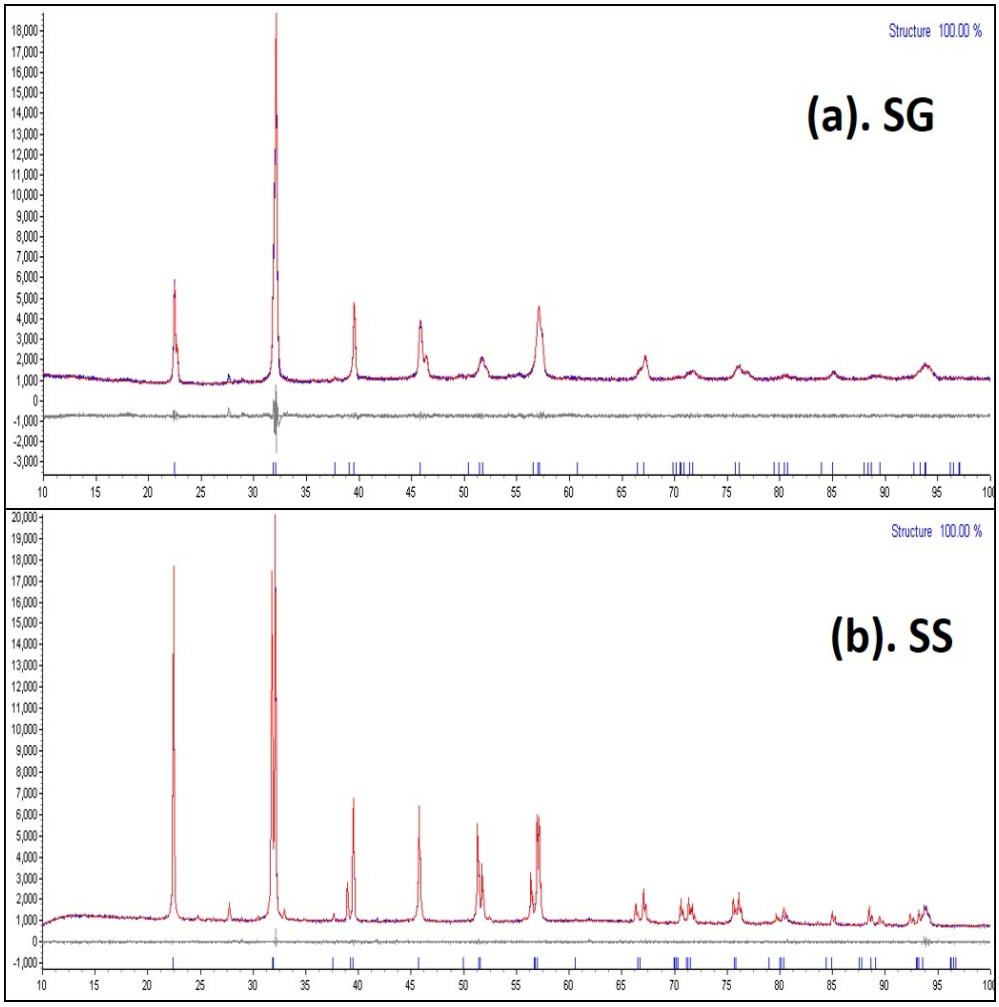

Figure 3.10 Rietveld refinement of the XRD data for BFO sample prepared by (a). SG and (b) SS. Observed (red lines), calculated (blue line), and difference (bottom line) profiles are shown. The Bragg reflections are marked by vertical bars. The bars correspond to *R3c* phase.

Table 3.1 Refined Structural Parameters for SS prepared $BiFeO_3$.

Site	*Np*	*x*	*y*	*z*	Atom	Occupancy
Bi	2	0	0	0	Bi^{+3}	1
Fe	2	0	0	0.22	Fe^{+3}	1
O	6	0.445	0.0187	0.952	O^{-2}	3

Table 3.2 Refined Structural Parameters for SG prepared $BiFeO_3$.

Site	*Np*	*x*	*y*	*z*	Atom	Occupancy
Bi	2	0	0	0	Bi^{+3}	1
Fe	2	0	0	0.203	Fe^{+3}	1
O	6	0.435	0.0207	0.914	O^{-2}	3

Table 3.3 Comparison of Structural Refined parameters of SS and SG prepared BFO

	SS - BFO	SG -BFO
***a* (Å)**	5.620(3)	5.5786(4)
***b* (Å)**	5.620(3)	5.5786(4)
***c* (Å)**	13.692(8)	13.871(6)
***V* (Å³)**	374.62(5)	373.84(5)
Bi-O (Å)	2.889	2.849
Fe-O (Å)	2.20	2.21
Fe-O-Fe (°)	153.42	153.02
R_{wp} %	6.81	5.01

3.5. FE-SEM and EDS studies

The microstructure of the samples viewed after polishing the surface of the samples with the help of a Carl-Zeiss Ultra55 Field

Emission Scanning Electron Microscope (FE-SEM is presented in figure 3.11. The microstructure shows well densified samples with few voids. The sol-gel (SG) synthesized materials contain fine grains, with average grain size ~0.6 μm, compared to powders synthesized via the solid-state (SS) reaction method (~0.9 μm). The density of SG prepared samples is higher than the SS prepared samples. The microstructure of the SG processed sample is agglomerated and exhibits grains of various shapes and sizes (0.1 μm to 1 μm). Energy Dispersive X-Ray Spectroscopy (EDS) analyses of these samples is shown in Figure 3.12 to determine chemical composition analysis of samples. From EDS spectra, no extra peaks other than the constituent elements are observed. The signals match exactly for the standard peak position for Bi, Fe, and Oxygen. Moreover, the EDS analysis shows that the chemical composition of BFO prepared through SS has bismuth loss whereas the samples processed through SG have nearly stoichiometric ratios (table 3. 4). This reveals that the elemental composition of BFO sample does not contain any foreign elements and the samples are chemically homogeneous.

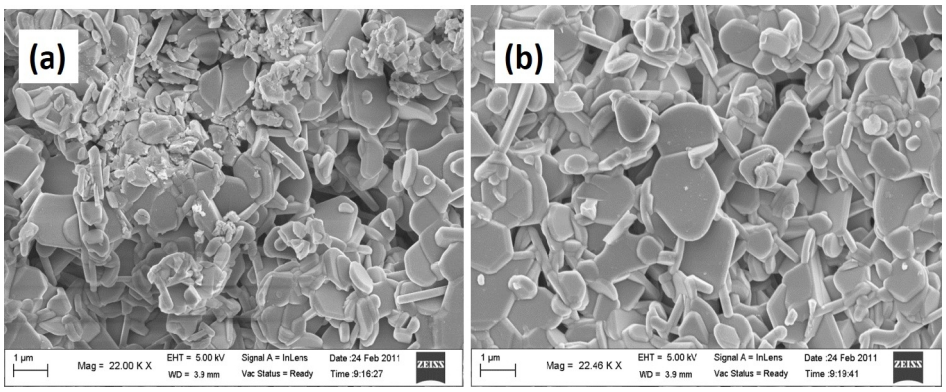

Figure 3.11 FE-SEM images of $BiFeO_3$ samples prepared by (a) sol-gel and (b) solid state methods.

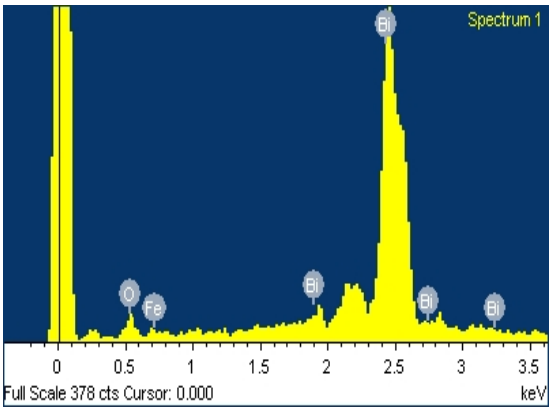

Figure 3.12 EDS spectram of SS prepared BFO.

Table 3.4 EDS composition

Element	Solid state		Sol-Gel	
	Weight %	Atomic %	Weight %	Atomic %
O	18.76	65.14	15.40	59.06
Fe	18.20	18.10	20.92	21.61
Bi	63.05	16.76	63.68	19.34

3.6. Raman Spectroscopy studies

The variation in the Raman modes with respect to different synthesis route will provide the information about the structural changes since Raman spectroscopy is sensitive to atomic displacements [17] and crystal symmetry [18]. The Raman modes of BFO prepared using SS and SG methods are presented in figure 3.13 and figure 3.14 respectively. For the pure BFO, Group theory calculations predict Γ_{R3c} = 13 ($4A_1$+9E) Raman modes in its rhombohedral distorted *R*3*c* space group [19, 20]. In the present study, out of 13 expected modes, twelve active Raman modes are detected. In addition to this, two phonon modes are also observed around 1100 – 1300 cm^{-1} in all samples, as observed in the previous studies on BFO [21, 22] (inset of the figure 3.13). From the first principal theory, the low frequency modes are attributed to the Bi-O bonds in the BFO. Most of the A_1 modes and some of the E (TO) modes are governed by the Bi–O bonds while Fe–O bonds contribute to the higher order E (TO) modes [22]. The observed Raman modes are same for the samples prepared by SS and SG. These modes are compared with the literature values and tabulated below in the table 3.5. All the observed modes in this study are well comparable with early reports and the mode at 98 cm^{-1}, which is inactive in the pure samples is seen in the doped systems, which will be discussed in the next session.

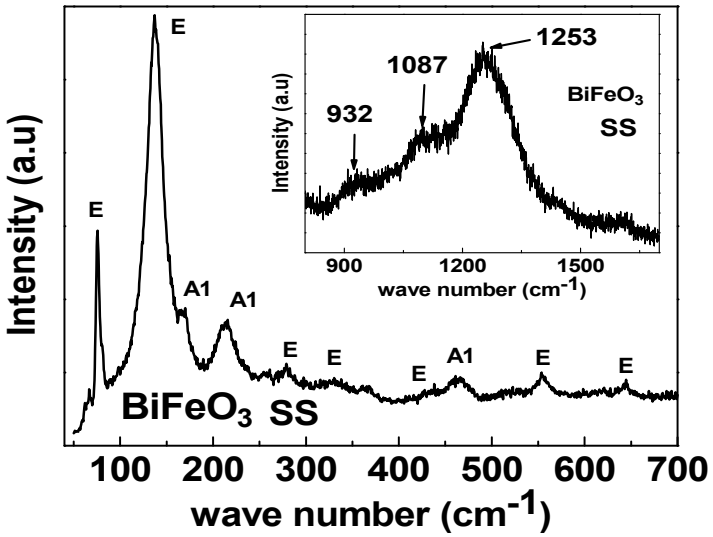

Figure 3.13 Raman modes of BFO prepared by SS method.

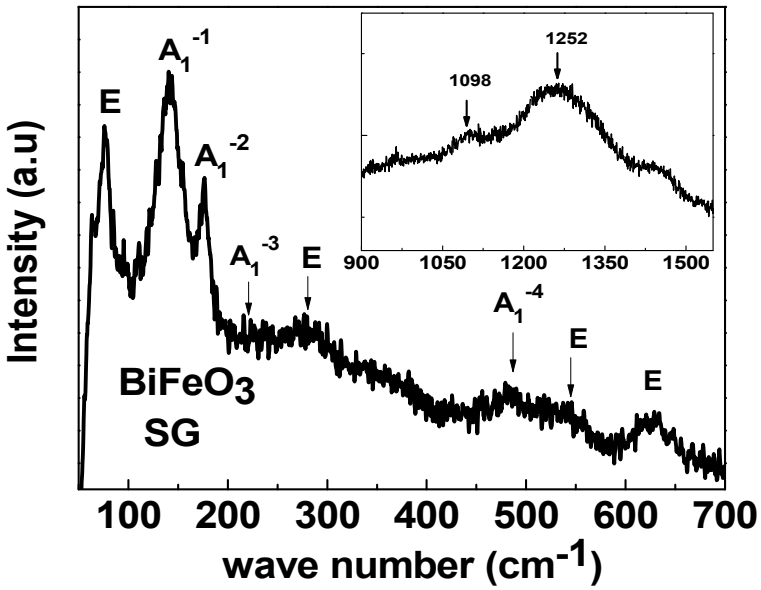

Figure 3.14 Raman modes of BFO prepared by SG method.

Table 3.5 Raman mode comparison of present study with the literature

Raman mode	$x = 0.0$	Literature values		
	Present Study	D. Kothari et al [23]	Fukumura et al. [24]	Singh et al. [25]
E (cm^{-1})	75.193	71.3	77	-
E (cm^{-1})	-	98	-	-
A_1^{-1} (cm^{-1})	136	135	136	136
A_1^{-2} (cm^{-1})	169	167	176	168
A_1^{-3} (cm^{-1})	215	218	227	211
E (cm^{-1})	256	255	265	-
E (cm^{-1})	278	283	279	275
E (cm^{-1})	330	321	351	335
E (cm^{-1})	367	351	375	365
A_1^{-4} (cm^{-1})	438	431	437	425
E (cm^{-1})	465	467	473	456
E (cm^{-1})	552	526	525	549
E (cm^{-1})	644	-	-	-

3.7. Electrical properties

The dimensions of the sample and the electrodes are very crucial in electrical measurements. The thickness of the sample determines the strength of the electric field applied. In the current study, silver paint is used as electrode and the sample thickness for dielectric measurements

is maintained as 1.5 mm while for ferroelectric measurements, it is reduced to 0.5 mm.

3.7.1. Dielectric properties

The dielectric measurement as a function of frequency in the range 20 Hz to 2 MHz are carried out to explore the effect of synthesis route on the electrical properties. The variation of dielectric constant (ε_r) with frequency for SS and SG processed BFO is shown in figures 3.15 and 3.16 respectively. The dielectric constant for BFO at a frequency of 1 kHz is 68 and 538 for SS and SG, respectively. There is a remarkable increase in εof sol gel prepared samples. The dielectric constant for SS prepared BFO decreases continuously with an increase in frequency showing the Debye relaxation. Whereas, for the samples prepared using SG, a large dielectric constant is found at low temperatures, which drastically falls up to a certain frequency range, and later it decreases slowly. This kind of behavior may come from the space charges at low frequencies. Along with the improvement in the dielectric constant, an increase in the dielectric loss (inset) is also found. The large dielectric value compared to SS processed samples indicates that the observed increase in the dielectric constant in SG processed samples is not intrinsic but has few contributions from other source. The high dielectric constant associated with high dielectric loss at low frequencies is a mark of

Maxwell-Wagner relaxation, generally exhibited by most of the samples prepared by wet chemical routes [26].

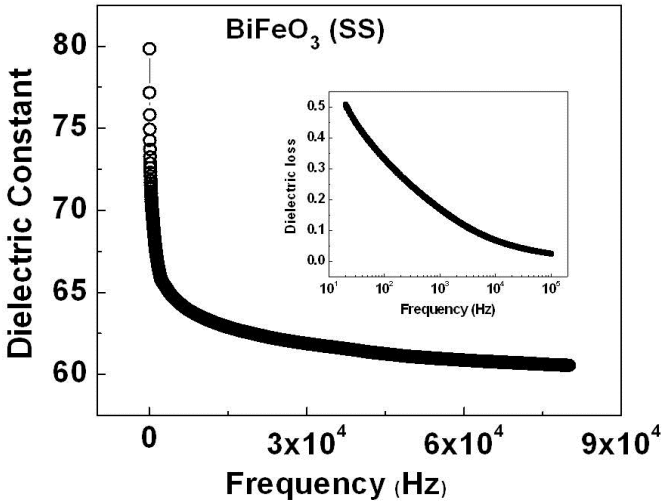

Figure 3.15 Dielectric constant versus frequency of $BiFeO_3$ samples prepared by solid state route. Inset shows the variation of dielectric loss with frequency.

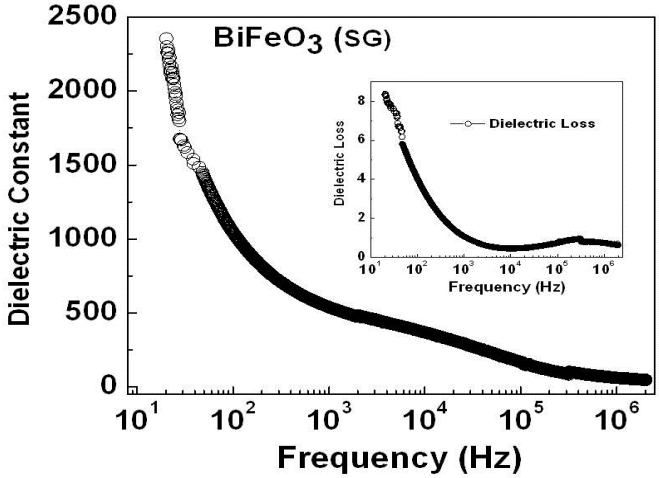

Figure 3.16 Dielectric constant versus frequency of $BiFeO_3$ samples prepared by sol-gel technique. Inset shows the variation of dielectric loss with frequency.

High frequency dielectric constant (60 and 150 at 10 kHz for SS and SG respectively) is due to the intrinsic nature of the sample. This increase in dielectric constant for SG samples is due to the smaller grain size and higher density.

The temperature dependent dielectric constant of SS prepared BFO at different frequencies is shown in the figure 3.17. Dielectric constant increases with an increase in the temperature for all the frequencies.

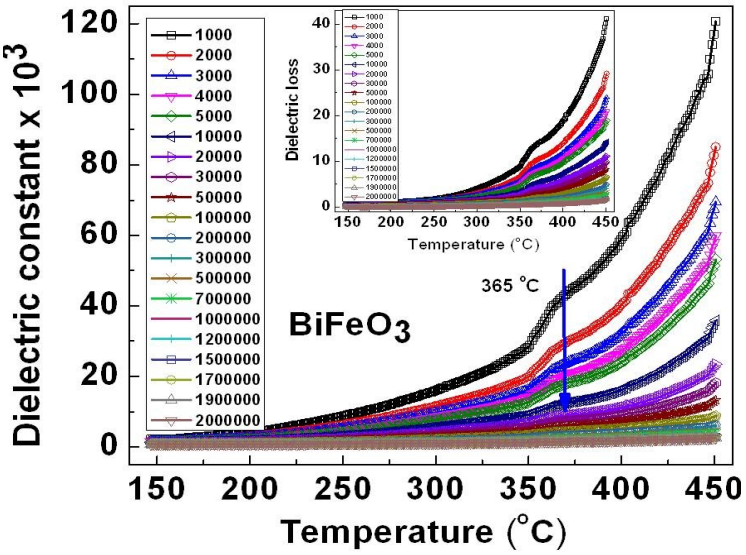

Figure 3.17 Dielectric constant versus temperature at various frequencies of SS prepared $BiFeO_3$. Inset shows the variation of dielectric loss with temperature.

It is observed that the temperature-dependent response shows a broad transition region at round 365 °C at 1 kHz. This temperature

corresponds to the Néel temperature (T_N) of BFO. The measurements at various frequencies show relaxor characteristics as the peak in dielectric plot shifts to higher temperatures with an increase in frequency.

3.7.2. P-E Hysteresis analysis

The ferroelectric polarization behavior of BFO was then investigated using electric response of the polarization. Bismuth ferrite undergoes a ferroelectric ordering along [001] polarization due to the cooperative distortion of the Bi centro-symmetric positions. The spontaneous polarization (P_s) is along pseudo-cubic $[111]_c$. The dielectric hysteresis loop was first measured by Teague et al [27] on the single crystal BFO at 70 K and the reported spontaneous polarization (Ps) value as ~ 3.5 $\mu C/cm^2$ for an applied electric field of 55 kV/cm. However, this value is much smaller than the theoretical predictions for such a ferroelectric material with a high Curie temperature and large distortion [28]. Nevertheless, a large P_r is also reported for BFO thin films and single crystals [29, 30]. The electric polarization hysteresis loops (*P-E*) of the bulk bismuth ferrite prepared through solid-state route is shown in figure 3.18. A non-linear P-E relationship can be seen with an unsaturated loop within the field limit of E ~ 60 kV/cm. The loops are not saturated at RT due to its high conductivity at high temperatures

[31]. It was found that the remnant polarization (P_r) and coercivity (E_C) of the BFO are around 0.83 μC/cm^2 and 35 kV/cm respectively.

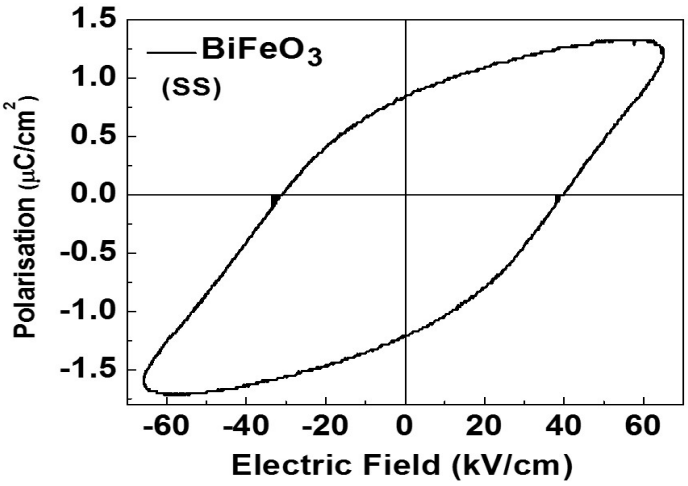

Figure 3.18 P-E loop for $BiFeO_3$ prepared through SS.

3.8. Magnetic properties

Subsequently, the magnetization behavior of the BFO samples prepared by both SS and SG was measured for different temperatures to see the effect of impurity phases on the magnetic properties. The M-H response of BFO at an applied field of 7 T is shown in figure 3.19. From the figure, the unsaturated and linear loops at 300 K indicate the antiferromagnetic nature of these samples. However the M-H loops measured at 5 K in both the samples show a curvature, indicating the existence of weak ferromagnetism at low temperatures. M-H loops clearly demonstrate that ceramics prepared through SG have enhanced

magnetic parameters, such as remnant, coercivity and saturation magnetizations, than that of SS prepared BFO. This improvement in magnetic properties can be attributed to the impure free phase of BFO in SG processed samples.

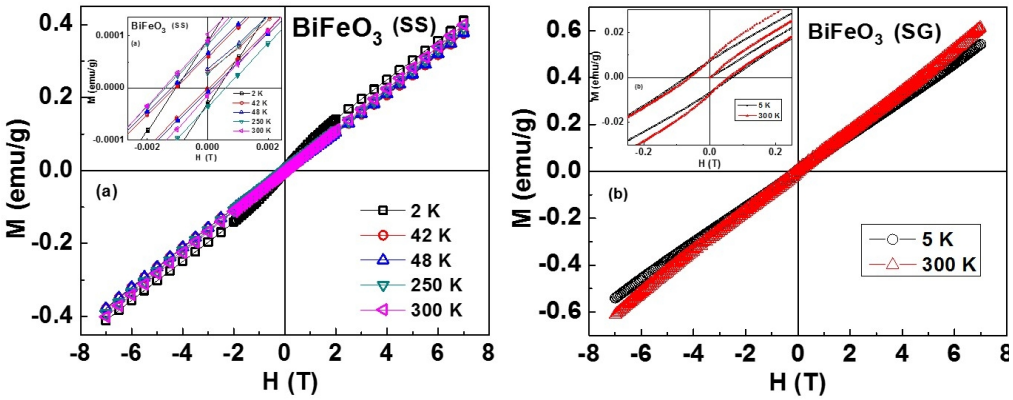

Figure 3.19 M-H loops at various temperatures for BFO prepared through (a) SS and (b) SG methods.

It is noted that the ceramics prepared through SS has a small percentage of secondary phase $Bi_2Fe_4O_9$, which is antiferromagnetic below room temperature with T_N ~ 250 K [32]. This impurity phase is almost absent in the SG samples. Thus, there is a small contribution of this impurity phase on the magnetic properties of BFO. The magnetic parameters derived from the magnetic hysteresis curves are listed in the Table 3.6. There are some interesting observations, the high field magnetization (M_{7T}) and remnant magnetization (M_r) increases with

decrease in temperature. But the temperature dependence of coercivity shows that H_C increases with an increase in the temperature. Similar kind of observation is reported in the literature for nanocrystalline BFO [33].

Table 3.6 Magnetic parameters of BFO prepared through SS and SG.

	Solid state		Sol-gel	
	5K	**300 K**	**5K**	**300 K**
M_r (emu/g)	$5.9x10^{-5}$	$5.3 x10^{-5}$	0.01	0.01
H_C (Oe)	6.8	8.8	52	63
M_{7T} (emu/g)	0.40	0.40	0.57	0.53

3.8.1. Low temperature M-T studies

Temperature dependence of magnetization, M (T) data is shown in figure 3.20. The ZFC and FC measurements are carried out in the temperature range 5 K - 300 K for an applied field of 1 kOe and 500 Oe for SS and SG prepared BFO samples respectively. Magnetization decreases with decrease in the temperature, which indicates antiferromagnetic nature. A sudden upturn in the magnetization is observed below 50 K for all the samples. The value of the magnetization at 5 K is $7.9x10^{-3}$ emu/g, 0.041 emu/g for SS and SG samples respectively. It is interesting to note that for solid state prepared samples, a cusp in

FC, ZFC is observed at 50 K. This indicates a change in spin ordering at low temperatures from AFM to FM in $BiFeO_3$.

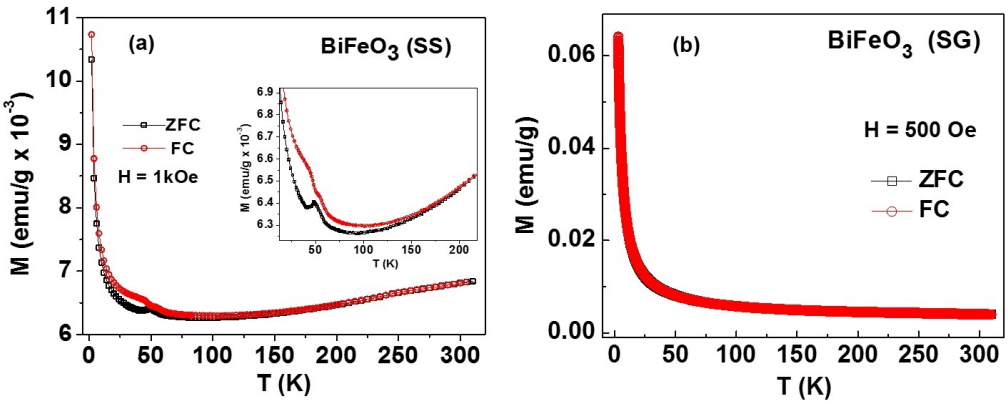

Figure 3.20 Temperature dependent magnetization curve (M-T) for BFO prepared through (a) SS and (b) SG.

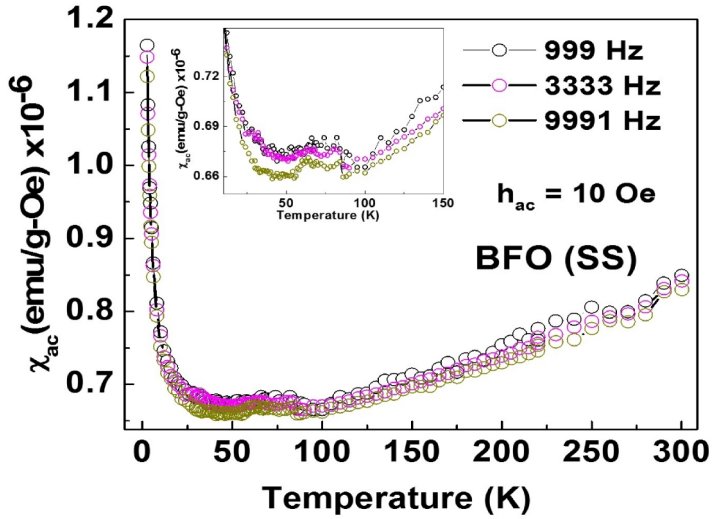

Figure 3.21 ac susceptibility data for BFO prepared through SS method.

Though the cusp at 50 K is not observed for SG samples in the present study, Park et al [34] reported this behavior for BFO prepared through the wet chemical method for different particle sizes. The splitting in ZFC and FC magnetization at 50 K is attributed to spin-glass transition in BFO in the previous studies [35, 36]. To confirm the spin glass nature, ac susceptibility measurements are carried out at h_{ac} = 10 Oe and various frequencies as presented in figure 3.21 to see the time dependence. The ac susceptibility data mimics the dc magnetization behavior with a cusp at 50 K. However, no frequency dependence is seen in the magnetization, which rules out the spin glass nature in these samples.

3.8.2. High Temperature M-T studies

So far, in the literature ZFC-FC measurements are reported mainly from 300 K to the lowest temperature 5 K. But to measure the true ZFC the sample needs to be cooled in zero fields from above the ordering temperature. In this thesis, to measure ZFC, the samples are cooled in zero fields from 850 K. The high-temperature ZFC-FC magnetization measured at 500 Oe is shown in figure 3.22. The magnetic transition is clearly seen in the M-T curves. Néel temperature (T_N) of the BFO is found to be 651 K. This value is well comparable with the reported value [33]. From the figure, it is noted that unlike low

temperature M-T, this shows a clear bifurcation in the ZFC and FC magnetization right from the transition temperature, representing the magnetic irreversibility present in this sample. After crossing the T_N, presence of short range magnetic interactions is seen.

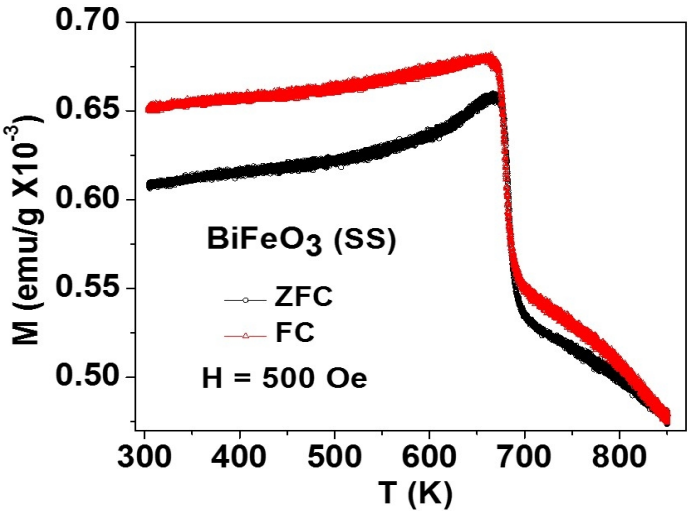

Figure 3.22 M-T for BFO prepared through SS method from 300 K – 850 K.

Conclusions

In summary, single phase bismuth ferrite is prepared through SG method and the secondary phases are minimised in SS route. The electrical and magnetic properties are enhanced slightly for SG processed samples.

Effect of RE element (La) doping on the Sol-gel prepared $BiFeO_3$

3(b)

3.9. Introduction

In the previous section, although the single-phase BFO is achieved through sol-gel reaction, the electric and magnetic properties are still very weak. In this regard, doping with La is chosen since many recent studies suggest La doping is effective to improve the multiferroic properties. Hence, the aim of present study is to prepare single phase La doped bismuth ferrite and measure different physical properties to understand the doping effect of rare earth element.

3.10. Experimental Details

To prepare $La_xBi_{1-x}FeO_3$ (LBFO) ceramics with x = 0 - 0.5 high-purity precursors $Bi(NO_3)_3{\cdot}5H_2O$, $La(NO_3)_3{\cdot}6H_2O$ and $Fe(NO_3)_3{\cdot}9H_2O$ of Sigma- Aldrich make were taken in a stoichiometric molar ratio for the Sol-gel synthesis as described in the previous section. The structural, electrical and magnetic properties are investigated.

3.11. Results and Discussion

3.11.1. X-ray diffraction Analysis

Figure 3.23 shows the room-temperature x-ray diffraction (XRD) pattern of the $La_xBi_{1-x}FeO_3$ (x = 0.0 - 0.5) samples. The diffraction peaks observed for pure BFO (x = 0) indicate the rhombohedral phase with the *R3c* space group and are consistent with powder diffraction patterns provided by the international Centre for diffraction data (JCPDF File No. 86-1518). A low-intensity peak at 27° indicates the presence of $Bi_{25}FeO_{40}$ as a secondary phase. However, absence of peak at 27° on La doping indicates that the $Bi_{25}FeO_{40}$ secondary phase is completely stifled and stable rhombohedral phase of BFO is established for La doping as low as x = 0.05. On increasing x = 0 to x = 0.2 and further to 0.5, the intensity of (1 2 2), (1 3 1) reflections found to decrease gradually and the intensity of (1 0 4) diffraction peak suppresses while the intensity of (1 1 0) peak increases and finally these two merge into a single broad peak with a shift towards higher angles as depicted in the inset of figure 3.23. These observations clearly indicate the gradual structural phase transition from the distorted rhombohedral *R3c* to orthorhombic *Pbnm* [37]. Further, the XRD pattern in the range of 31°– 33° (inset of fig.3.23) shows the resulting crystal distortion on substituting the larger La^{3+} (r = 1.22 Å) ion for Bi^{3+} (r = 1.14 Å) ion in LBFO.

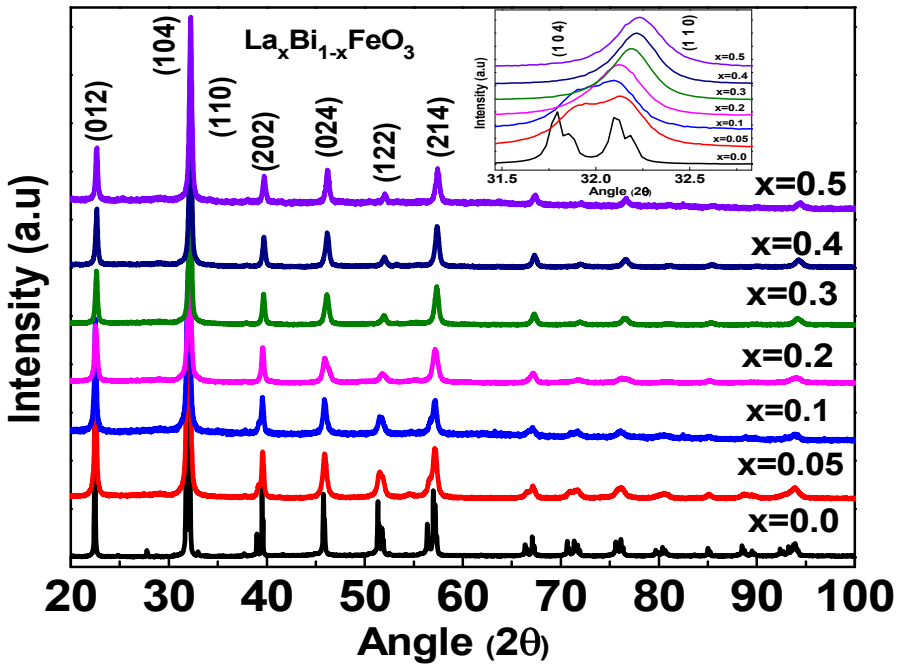

Figure 3.23 XRD data for $La_xBi_{1-x}FeO_3$ samples prepared by SG (Inset shows the zoomed view of the same around 32°).

3.11.2. Rietveld refinement

Rietveld refinement is carried out on $La_xBi_{1-x}FeO_3$ ceramics for x = 0.0, 0.05, 0.2 and 0.4. As the concentration of La increases, the structure is anticipated to go to orthorhombic *Pbnm* phase since pure $LaFeO_3$ exists in *Pbnm*. Hence, *R3c* and *Pbnm* structural models are considered for refinement below and above certain concentration of lanthanum. The detailed analysis of Rietveld refinement reveals that up to x = 0.2, LBFO is in *R3c* phase and the structure becomes *Pbnm* for $0.2 < x \leq 0.5$, which is consistent with earlier reports [38]. The rietveld refinement pattern is

shown in the figure 3.24 and corresponding refined lattice parameters for $La_xBi_{1-x}FeO_3$ powders are tabulated in table 3.7.

Table 3.7 Refined parameters of $La_xBi_{1-x}FeO_3$ sample.

	$x = 0$	$x = 0.05$	$x = 0.2$	$x = 0.4$
***a* (Å)**	5.5786(4)	5.5782(9)	5.5789(7)	5.6095(5)
***b* (Å)**	5.5786(4)	5.5782(9)	5.5789(7)	7.8139(4)
***c* (Å)**	13.871(6)	13.865(4)	13.85(13)	5.432(8)
***V* (Å^3)**	373.84	373.63	373.32	238.09
Fe – O_2 (Å)	2.20	2.178	2.12	2.11
Fe- O_2 –Fe (°)	153.4	153.3	152.3	152.01
R_{wp} %	2.95	4.2	3.06	5.34
R_p %	2.12	2.40	3.10	2.20

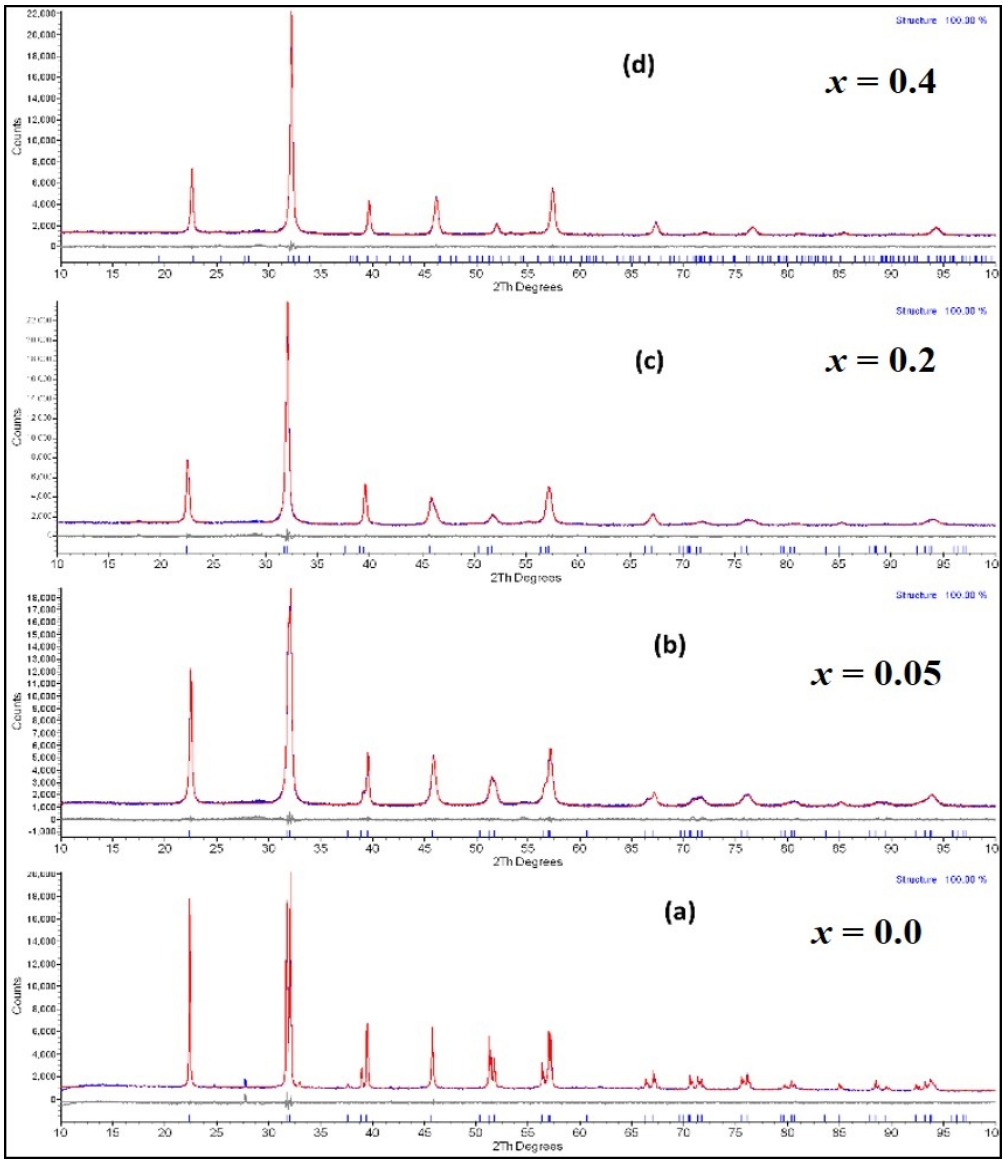

Figure 3.24 Rietveld refinement of the XRD data for $La_xBi_{1-x}FeO_3$ sample prepared by SG at (a) x = 0.0, (b) x = 0.05, (c) x = 0.2 and (d) x = 0.4. Observed (red lines), calculated (blue line), and difference (bottom line) profiles are shown. The Bragg reflections are marked by vertical bars.

3.11.3. Raman Studies

Figure 3.25 shows the Raman spectra of LBFO samples recorded at 300 K. The Raman spectra from the LBFO samples exhibit almost the same BFO modes, but with reduced intensities accompanied by a slight shift in the wave number to lower frequency with x. The modes appear with a strong intensity for the composition x = 0.05 consistent with the rhombohedral, *R3c* structure of single phase BFO. A new mode corresponding to *R3c* structure is observed at 94 cm^{-1}(E) in all the doped samples. As the value of x rises, the modes at 215 (A_1^{-3}), 278 (E), 330 (E), 367 (E) and 465 (E) cm^{-1} were found to vanish, and the modes at 438 (A_1^{-4}), 552 (E) and 644 (E) cm^{-1} were found to shift towards lower frequency. It is very interesting to note that the intensity of the mode at 136 cm^{-1} (A_1^{-1}) decreases gradually with x up to x = 0.1 and disappears completely for x = 0.2 and suddenly it reappears for $x \geq 0.3$. The mode at 169 (A_1^{-2}) cm^{-1} diminishes and shifts to a low frequency up to x = 0.3 and it vanishes for further doping levels. As x increases, these displacements in Raman modes are attributed to structural distortion and reduction of vibrations in the FeO_6 octahedral with increasing substitution of Bi by La. The fundamental 12 Raman modes of BFO are reduced to 10 modes in LBFO for x = 0.2 and further reduced to 7 modes for x = 0.4. This is a clear indication of structural modification and symmetry change in BFO

due to the La doping. The observed results of Raman spectra are found to be consistent with XRD results.

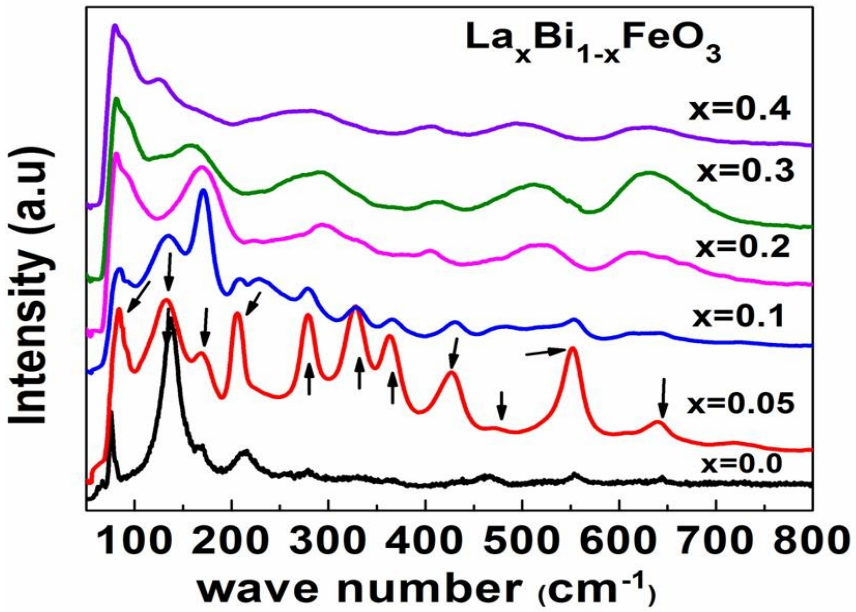

Figure 3.25 Raman spectrum at 300 K of $La_xBi_{1-x}FeO_3$ (x = 0 - 0.4).

3.11.4. Dielectric properties

One of the main problems of $BiFeO_3$ that limit the usage in devices is its low resistivity. A very low dielectric constant is observed for undoped BFO. Hence, the effect of Lanthanum doping on its electrical properties is interesting as lanthanum results in crystal distortion due to unequal ionic radii.

The variation of dielectric constant (ε′) of these samples as a function of frequency in the range 20 Hz - 2 MHz prepared by SG route

is shown in figure. 3.26. The maximum value of dielectric constant can be observed at La content x = 0.05. It is clear that all the SG prepared samples have a very high value of dielectric constant in low frequency region which is higher than previous reports in other RE doped $BiFeO_3$ [39, 40]. Similar kind of dielectric behaviour with huge value of dielectric constant has been found in citric acid route prepared $SmFeO_3$ [41]. This kind of behaviour exhibiting high dielectric constant at low frequency and the low value at high frequency is a mark of Maxwell-Wagner type dielectric dispersion [26]. The high value of dielectric at low frequency is not merely from the sample but other contributions such as silver paint or unevaporated reagents, along with the space-charge polarization. The true dielectric constant of the SG processed samples can be seen at high frequency range, which has the values 59, 61, 75, 78 and 97 for x = 0, 0.05, 0.1, 0.2 and 0.3 respectively at 1 MHz.

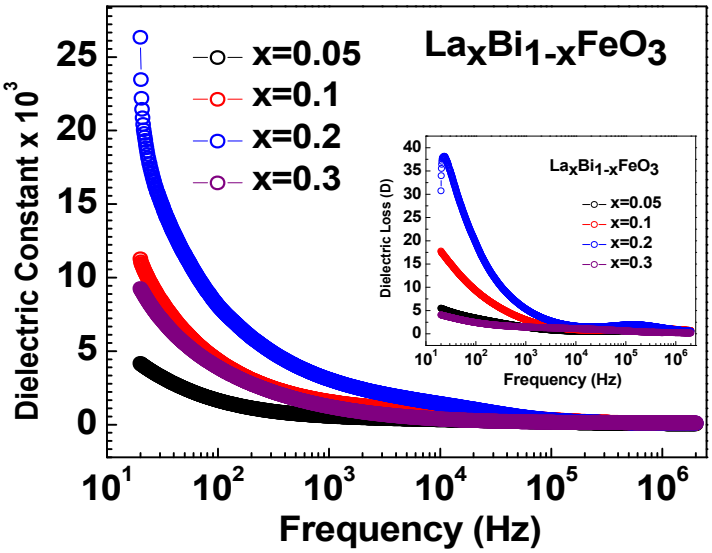

Figure 3.26 Dielectric versus frequency graph of $La_xBi_{1-x}FeO_3$ (x = 0, 0.05, 0.2 and 0.4) samples.

3.11.5. Magnetic properties

The magnetic hysteresis loops of LBFO samples with x = 0.0, 0.05, 0.2 and 0.4 are measured by applying a field of 7 T at 300 K and 5 K (Figure. 3.27(a)) The M-H curve for x = 0.0 sample show a linear field dependence of magnetization indicating the antiferromagnetic nature of undoped BFO. Remnant magnetization (M_r) for BFO at RT is found to be almost zero and increases gradually with x reaching a maximum value of 0.274 emu/g for x = 0.4. The coercive field, H_C is found to increase from 8.53 to 591.8 Oe as x increases to 0.05 and further rise in La to x = 0.4 results in a huge improvement in H_C to ~19 kOe, which is the **highest H_C reported for any RE doped BFO system**, to the best of our

knowledge. This increases further to ~ 20 kOe at 5 K (Figure 3.27(b)). The increase in the H_C at low temperatures is due to the increase in anisotropy constant of these samples. However, the H_C of the order of ~15 kOe at RT was previously reported for the other dopant systems [42, 43]. This remarkable enhancement in the H_C and M_r with La is a clear indication of the transition from antiferromagnetic to ferromagnetic nature. The M measured at 7 T (M_{7T}) increases linearly with x at RT whereas at 5 K, it reaches a maximum value of 0.88 emu/g for $x = 0.2$.

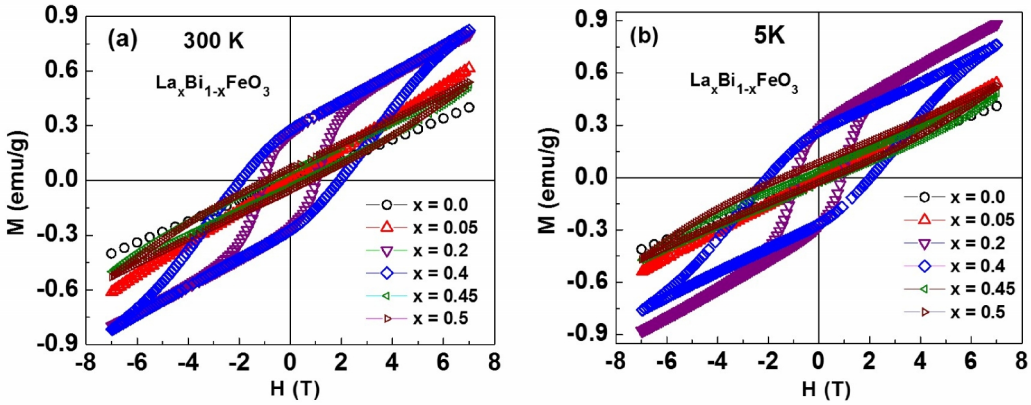

Figure 3.27 M-H loops of $La_xBi_{1-x}FeO_3$ (x = 0, 0.05, 0.2, 0.4, 0.45 and 0.5) samples at (a) 300 K, and (b) 5K.

The G-type AFM structure in BFO limits the observation of net magnetization. The potential magnetization locked in the spin cycloid of the BFO can be released by destroying the cyclic spin structure upon doping [44]. The systematic increase in M_r with x is due to the gradual collapse of the space-modulated spin structure of BFO. The hysteresis

loops for various doping levels of La are compared in figure 3.28. The M at 7 T for x = 0.05 is very low compared to x = 0.2, while a radical improvement is found for x = 0.4. As a result, clear openings in the hysteresis loops are observed for 0.2 and 0.4 samples. This is in good agreement with the change in the crystal structure caused by La doping. For $x \leq 0.2$ the structure remains in *R3c*, whereas a change in the structure to *Pbnm* is observed for $0.2 < x \leq 0.5$. Thus, both the canting angle of the spins and the cycloid spin structure gets modified with the doping. As x increases, the approach to the saturation in M-H loops starts at lower fields and high H_C is observed for doped samples, which is associated to the doping-driven increase in the magnetic anisotropy [45, 46]. The La substitution can influence the anisotropy directly by inducing changes in the crystal field of ligands through the doping or indirectly by changing spontaneous polarization through the chemical pressure and dilution of polar-active Bi sub lattice [47]. The observed magnetic anisotropy may mainly come from magneto crystalline and magneto elastic anisotropy. Further studies are needed to compliment the details of the high magnetic anisotropy in La-doped BFO.

Temperature dependences of the 'zero field cooled' (ZFC) and 'field cooled' (FC) magnetization curves measured at H = 500 Oe for LBFO samples (x = 0, 0.05 and 0.2) are depicted in figure. 3.28. It is observed that the magnetization is enhanced significantly by La doping.

The M at 5 K for x = 0 found to be 0.011 emu/g increases to 0.169 emu/g for x = 0.2 sample. Similar to SS prepared BFO, a cusp at 50 K is observed in all the samples, which is attributed to the spin glass transition in the literature [36]. To confirm the spin glass nature, ac susceptibility measurements are carried out on x = 0.2 sample with an applied field of 10 Oe for several frequencies. The ac susceptibility data shows a peak near 60 K, following the dc magnetic behaviour with no frequency dependence of magnetization (figure 3.29). This rules out the possibility of spin glass nature in these systems.

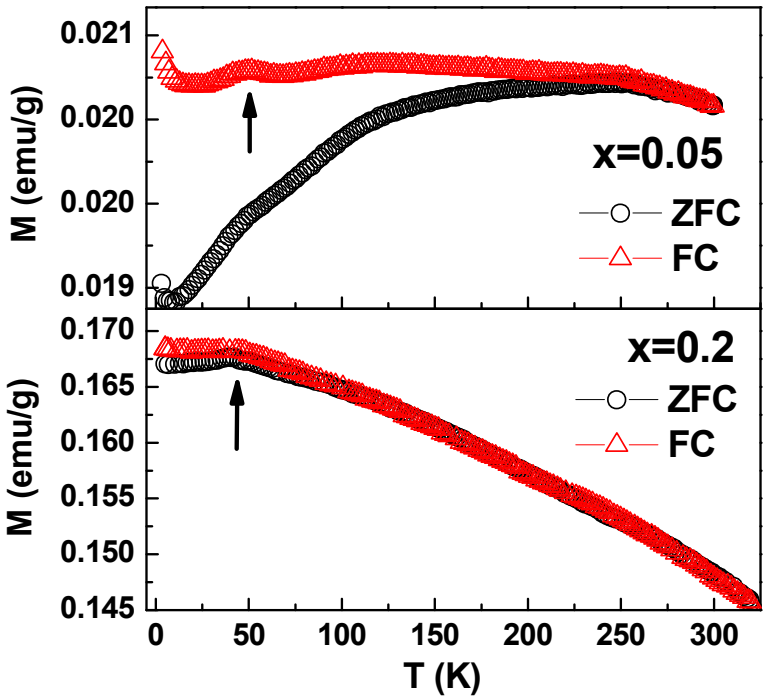

Figure 3.28 M-T curve of $La_xBi_{1-x}FeO_3$ (x = 0.05 and 0.2) samples at 500 Oe from 5K - 300K.

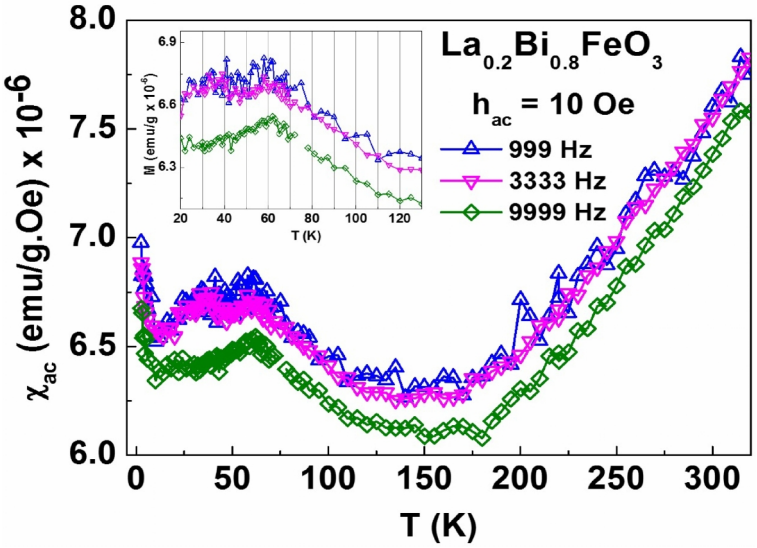

Figure 3.29 ac susceptibility measurement on $La_xBi_{1-x}FeO_3$ (x = 0.2) sample at 10 Oe from 5K - 300 K.

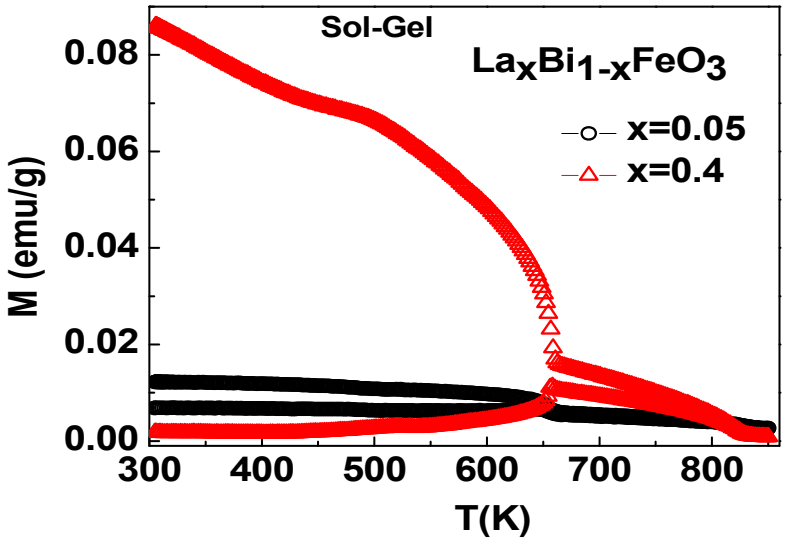

Figure 3.30 M-T curve of $La_xBi_{1-x}FeO_3$ (x = 0.05 and 0.4) samples at 500 Oe from 300 K – 850 K.

The high-temperature M-T curves are shown in the figure 3.30 at H = 500 Oe. Similar to the low-temperature M-T curve, magnetization in high temperature region shows an increase in the magnetization for the La doping level x = 0.4 compared to x = 0.05. It clearly shows the magnetic transition in these samples. T_N of the BFO is found to be 651 K. The value of T_N linearly increases with x, and it reaches to 663 K for x = 0.4 sample in agreement with the earlier report [48]. The increase in T_N with x approaching T_N of $LaFeO_3$ (738 K) also supports the structural transition to orthorhombic *Pbnm*. The significant bifurcation between the ZFC and FC curves indicate the presence of magnetic irreversibility in magnetization in all the samples below T_N.

3.12. Summary

Bismuth ferrite is prepared through solid state and sol gel reactions. Solid-state reaction method prepared BFO contains minor secondary phases for calcination at 820 °C for 30 min. whereas, sol-gel method helps in removing the secondary phases for the optimal preparation conditions. A huge improvement in the dielectric constant is seen for the SG prepared compounds due to Maxwell-Wagner contribution. Magnetic properties also increased slightly in SG.

Lanthanum doped bismuth powders were prepared using sol gel method taking citric acid as a complexion agent. The *R3c* structure

changes to orthorhombic *Pbnm* phase as the La doping increases. The smaller particle size ~0.4 μm of SG prepared samples results in the high densification and the dielectric constant increases. A large dielectric constant in the order of ~10^4 is observed in these samples at low frequencies. M-H loops show a huge coercivity due to the high anisotropy in LBFO samples. The increase in the magnetization of these samples is due to the destruction of spin cycloid structure.

References

[1]. P. Fischer, M. PoIomska, I. Sosnowska, and M. Szymanski, *J. Phys.C: Solid St. Phys.* **13**, 1931 (1980).

[2]. D. Maurya, T. Harikishan, N K Singh, A Garg, *J. Alloys and Compounds* **477,** 780 (2009).

[3]. M. Valant, A. Anna-Karin, and N. Alford, *Chem. Mater.* **19**, 5431(2007).

[4]. R. Safi, H. Shokrosllahi, *Prog in Solid State Chemistry* **40**, 6e15 (2012).

[5]. A Jaiswal, D Raja, K. Vivekanand, M A Priya, A Suguna, and P Poddar, *J. Phys. Chem. C*, **114**, 2108 (2010).

[6]. J-H Xu, Hua Ke, De-Chang Jia, Wen Wang, Yu Zhou, *J. Alloys. Compounds* **472**, 473 (2009).

[7]. F. Chen, Q. F. Zhang, J. H. Li, Y. J. Qi, C. J. Lu, *Appl. Phys. Lett.* **89**, 092910 (2006).

[8]. M. P. Pechini, *U.S. Patent No.* **3330697**, July 11, (1967).

[9]. S Ghosh, S Dasgupta, A Sen, H S Maiti, *Mater. Res. Bull.* **40**. 2073 (2005).

[10]. S. Shetty, V. R. Palkar, R. Pinto, *Pramana, J. Phys.* **58**, 1027 (2002).

[11]. T.T. Carvalho and P.B. Tavares, *Materials Letters* **62,** 3984 (2008).

[12]. M. M. Kumar, A. Srinivas, S.V. Suryanarayana, *J. Appl. Phys.* **87**, 855 (2000).

[13]. A. K. Pradhan, K. Zhang, D. Hunter, J. B. Dadson, G. B. Loutts, P. Bhattacharya, R. Katiyar, J Zhang, D. J. Sellmyer, U. N. Roy, Y. Cui, and A. Burger, *J. Appl. Phys.* **97**, 093903 (2005).

[14]. Y. P. Wang, L. Zhou, M. F. Zhang, X. Y. Chen, J. M. Liu, and Z. G. Liu, *Appl. Phys. Lett.* **84**, (2004).

[15]. Yuan, G. L.; Or, S. W.; Wang, Y. P.; Liu, Z. G.; Liu, *J. M. Solid State Commun.* **76,** 138 (2006).

[16]. G Biasotto, A. Z. Simões, C. R. Foschini, S. G. Antônio, M. A. Zaghete, J. A. Varela, *Proce.Appli.Cer.* **5**, 171(2011).

[17]. R. Guo, F. Liang, D. Wen, F. Zheng, and M. Shen, *J. Phys. Chem. C* **114**, 21390 (2010).

[18]. M. Cazayous, D. Malka, D. Lebeugle, and D. Colson, *Appl. Phys. Lett*. **91**, 071910 (2007).

[19]. M. N. Iliev, A. P. Litvinchuk, V. G. Hadjiev, M. M. Gospodinov, V. Skumryev and E. Ressouche, *Phys. Rev. B.* **81**, 024302 (2010).

[20]. Y. Wang and C. –W. Nan, *J. Appl. Phys.* **103**, 114104 (2008).

[21]. O. R. Mariola, M. Krishnamurthi, S. Denev, A. Kumar, S. Y. Yang, Y. H. Chu, E. Saiz, J. Seidel, A. P. Pyatakov, A. Bush, D. Viehland, J. Orenstein, R. Ramesh and G. Venkatraman, *Appl. Phys. Lett.* **92**, 022511 (2008).

[22]. V. R. Reddy, D. Kothari, A. Gupta and S. M. Gupta, *Appl. Phys. Lett.* **94**, 082505 (2009).

[23]. D Kothari, V. R Reddy, V.G. Sathe, A Gupta, A. Banerjeen and A. M. Awasthi, *J. Mag. Mag. Mat*. **320**, 548 (2008).

[24]. H. Fukumura, H. Harima, K. Kisoda, M. Tamada, Y. Noguchi and M. Miyayama, *J. Magn. Magn. Mater*. **310,** e367 (2007).

[25]. M.K. Singh, H.M. Jang, S. Ryu, M.H. Jo, *Appl. Phys. Lett*. **88**, 42907 (2006).

[26]. P. Jayanta and S. B. Krupanidhi, *J. Appl. Phy.* **104**, 024107 (2008).

[27]. J. R. Teague, R. Gerson, W.J. James, *Solid State Commun.* **8**, 1073 (1970).

[28]. J. B. Neaton, C. Ederer, U. V. Waghmare, N. A. Spaldin, and K. M. Rabe, *Phys. Rev. B*, **71,** 014113 (2005).

[29]. J. B. Neaton, H. Zheng, V. Nagarajan, S. B. Ogale, B. Liu, D. Viehland, V. Vaithyanathan, D. G. Schlom, U. V. Waghmare, N. A. Spaldin, K. M. Rabe, M. Wuttig and R. Ramesh, *Science*, **299** 1719 (2003).

[30]. D. Lebeugle, D. Colson, A. Forget, and M. Viret *Appl. Phys. Lett.* **91**, 022907 (2007).

[31]. Y. V. Shaldin, S. Matyjasik, and A. A. Bush, *Crystallogr. Rep*., **52** 123 (2007).

[32]. M. N. Iliev, A. P. Litvinchuk, and V. G. Hadjiev, M. M. Gospodinov, V. Skumryev and E. Ressouche, *Phy. Rev. B.* **81**, 024302 (2010).

[33]. S. Vijayanand, M. B. Mahajan, H. S. Potdar, and P. A. Joy, *Phy Rev B* **80**, 064423 (2009).

[34]. T J Park, G C. Papaefthymiou, A J. Viescas, A R. Moodenbaugh and S S Wong, *Nano Lett.* **7**, 766 (2007).

[35]. S. Vijayanand, H. S. Potdar and P. A. Joy, *Appl. Phys. Lett.* **94**, 182507 (2009).

[36]. M. K. Singh, W. Prelier, M. P. Singh, R. S. Katiyar and J.F. Scott, *Phys. Rev. B.* **77**, 144403 (2008).

[37]. H. Ootera, T. Oomori, M. Tuda, and K. Namba, *Jpn. J. Appl. Phys.* **33,** 4276 (1994).

[38]. S. T. Zhang, L. H. Pang, Y. Zhang, M. H. Lu, and Y. F. Chen, *J. Appl.Phys.* **100**, 114108 (2006).

[39]. K. Sen, K. Singh, A. Gautam and M. Singh, *Cer. International.* **38**, 243 (2012)**.**

[40]. Du Yi, Z X. Cheng, M. Shahbazi, E W. Collings, S X Dou and X L Wang, *J. Alloys. Compounds.* **490,** 637 (2010).

[41]. B V. Prasad, G. Narsinga Rao, J.W. Chen and D Suresh Babu, *Mat. Res. Bull.* **46**, 1670 (2011)**.**

[42]. A. Z. X. Cheng, X. L. Wang, Y. Du, and S. X. Dou, *J. Phys. D: Appl. Phys.* ***43***, 242001 (2010).

[43]. V V Lazenka, G Zhang, J Vanacken, I I Makoed, A F Ravinski and V V Moshchalkov, *J. Phys. D: Appl. Phys.* **45**, 125002 (2012).

[44]. Z. X. Cheng, A. H. Li, X. L. Wang, S. X. Dou, K. Ozawa, H. Kimura, S. J. Zhang, and T. R. Shrout, *J. Appl. Phys.* **103**, 07E507 (2008).

[45]. A. M. Kadomtseva, Yu. F. Popov, A. P. Pyatakov, G. P. Vorob'ev, A. K. Zvezdin, and D. Viehland, *Phase Transitions* **79**, 1019 (2006).

[46]. G. Le Bras, D. Colson, A. Forget, N. Genand-Riondet, R. Tourbot, and P. Bonville, *Phys. Rev. B* **80,** 134417 (2009).

[47]. N. Wang, J. Cheng, A. Pyatakov, A. K. Zvezdin, J. F. Li, L. E. Cross, and D. Viehland, *Phys. Rev. B* **72**, 104434 (2005).

[48]. A. A. Amirov, A. B. Batdalov, S. N. Kallaev, Z. M. Omarov, I. A.Verbenko, O. N. Razumovskaya, L. A. Reznichenko, and L. A. Shilkina, *Phys. Solid State* **51**, 1189 (2009).

Effect of A-site substitution of RE (La, Gd and Ho) element on the structure, electric and magnetic properties of solid state prepared $BiFeO_3$.

4
Chapter

Abstract:–

In this chapter, we have investigated the effect of rare earth (RE) doping on the structure; electric and magnetic properties of $BiFeO_3$ (BFO) prepared by the conventional solid-state reaction method. The main aim is to stabilize the phase purity of BFO and also to address how the G-type antiferromagnetic spin structure of BFO gets affected by doping with different RE elements. To understand the variations in the magnetic properties, non-magnetic (La) and magnetic (Gd and Ho) rare-earth elements as dopants with different ionic radii are considered.

Detailed XRD analysis on $RE_xBi_{1-x}FeO_3$ (RE = La, Gd and Ho) (x = 0.0 - 0.4 for La, x = 0.0 - 0.35 for Gd and x = 0.0 - 0.2 for Ho) samples revealed a structural phase transition with increase in x. Lanthanum doping results in the huge coercivity, while Gd helps in improving dielectric constant and magnetization. Ho doping results in highest magnetization among all the rare earths studied in the present dissertation. An enhancement in the dielectric constant is observed due to crystal distortion, due to ionic radii mismatch at A-site. Magnetic properties are greatly improved due to the modification of spin cycloid structure since the bond angle Fe-O-Fe and bond length Fe-O reduces with doping. In addition, magnetic RE doped samples have contributions from RE-RE and RE-Fe interactions. The results are discussed in terms of a model consisting of two sublattices coupled antiferromagnetically.

Effect of La doping on the multiferroic properties of $BiFeO_3$

4(a

4.1. Introduction

As discussed in the previous chapter, synthesis of pure $BiFeO_3$ BFO through solid-state reaction method is a challenging task due to the formation of impurity phases like $Bi_2Fe_4O_9$, $Bi_{25}FeO_{40}$. Further, the high leakage current and low magnetic properties are found to be limiting factors for its extensive use [1]. Furthermore, the spiral spin structure of BFO cancels out the ferromagnetic interaction in this system resulting in a very weak magnetization. As reported in the earlier studies, and as well as in chapter. 3, La substitution at A-site of ABO_3 type $BiFeO_3$ improves magnetic properties [2, 3] by suppressing spin cycloid structure. Moreover, La doping results in remarkable improvement of dielectric constant and decreases the leakage current [4]. La doping results in the structural phase transition due to the variation of ionic size. In the literature, a series of structural transitions from rhombohedral *R3c* ($0 < x < 0.06$) to triclinic *P1* ($0.06 < x < 0.24$) and then to orthorhombic *C222* ($0.25 < x < 0.4$) [5] are reported. Zang et.al.,

observed a transition directly from *R3c* ($0 \leq x \leq 0.25$) to orthorhombic *Pbnm* for $x \geq 0.3$ [6]. Where as, Yuan et al., reported a structural change from *R3c* to *P1* for $0.05 < x < 0.15$ and *P4mm, P4/mmm for* $x = 0.2, 0.25$ respectively [7]. Thus, systematic study is required to establish the clarity regarding the structural change with La doping. In this chapter, a two-phase model consisting of *R3c* and *Pbnm* is used to carry out a detailed structural refinement and quantitative estimates of rhombohedral and orthorhombic phases with La doping are reported. The dielectric, and temperature dependent magnetic properties in $La_xBi_{1-x}FeO_3$ (x = 0.0 - 0.4) powders are also presented.

4.2. Experimental details

The synthesis of $La_xBi_{1-x}FeO_3$ (x = 0.0 - 0.4) (LBFO) powders is carried out by solid-state reaction method. The stoichiometric amounts of La_2O_3, Bi_2O_3 and Fe_2O_3 are considered as starting materials for the solid state reaction, discussed in the chapter 3. The pellets of the samples after annealing are characterized for structural, electrical and magnetic properties.

4.3. Results and Discussion

4.3.1. Structural properties

Figure 4.1 shows the XRD pattern of $La_xBi_{1-x}FeO_3$ (x = 0.0 - 0.4) samples. The analysis of XRD patterns of pure $BiFeO_3$ sample reveals the Rhombohedral structure with a space group of *R3c*. XRD peak at 27. 7° indicates the presence of a minor phase $Bi_{25}FeO_{40}$ along with BFO. The introduction of La suppresses the formation of this secondary phase. The XRD patterns clearly show the absence of impurity phase as the La concentration increases beyond x = 0.15. Compared to pure BFO, the peaks in XRD pattern are found to shift to higher angle with increasing La concentration. It is also observed that, with increasing La composition, the doublets at 32° and 57° disappeared and new peaks are observed at 22° and 46°. This confirms a structural phase transition from Rhombohedral to Orthorhombic.

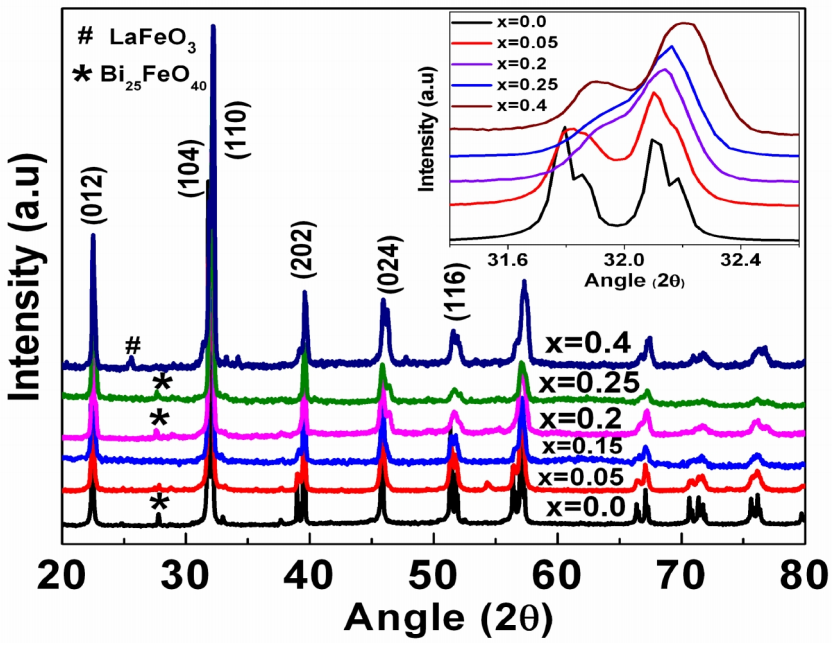

Figure 4.1 XRD of $La_xBi_{1-x}FeO_3$ (x = 0, 0.05, 0.2, 0.25, 0.4) ceramics (Inset highlights the evolution of diffraction peaks at 32° and 57° with x).

XRD data of $La_xBi_{1-x}FeO_3$ is refined with two phases with varying volume fractions as a structural transition is expected with an increase in x. Hence, *R3c* and *Pbnm* input phases are considered for the refinement since pure BFO exists in rhombohedral *R3c*, while pure $LaFeO_3$ exists in orthorhombic *Pbnm* structure [8]. The Rietveld refinement performed on samples for $0.05 \leq x \leq 0.4$ using *R3c+Pbnm* symmetry as depicted in figure 4.2 is found to fit better than other structural models proposed in the literature such as *R3c*, *P1*, *C222*, *R3c+Pnma* and *R3c+Pbnm* [5, 9-10].

It can be noticed from table 4.1 that the calculated lattice constants and unit cell volume decrease systemattically with x. This reduction is due to contraction in spacing between the atomic planes in which the Bi^{3+} having lower ionic radius of 1.14 Å is replaced with La^{3+} ion with 1.22 Å ionic radius. As the La content increase from 5% to 40%, the volume fraction of rhombohedral *R3c* decreases from ~92.4% to ~58.39% while that of orthorhombic *Pbnm* phase increases from ~7.59% to ~41.60%.

Table.4.1 Refined Structural Parameters for $La_xBi_{1-x}FeO_3$ (0, 0.05, 0.2 and 0.4) samples.

Compound	$BiFeO_3$	$La_{0.05}Bi_{0.95}FeO_3$		$La_{0.2}Bi_{0.8}FeO_3$		$La_{0.4}Bi_{0.6}FeO_3$	
Structure	*R3c*	*R3c* (92.4%)	*Pbnm* (7.59%)	*R3c* (77.8%)	*Pbnm* (22.11%)	*R3c* (58.39%)	*Pbnm* (41.60%)
a (Å)	5.6207(3)	5.6137(5)	5.5561(3)	5.6000(8)	5.5400(4)	5.5796(7)	5.4934(8)
b (Å)	5.6207(3)	5.6137(5)	5.5617(7)	5.6000(8)	5.5500(6)	5.5796(7)	5.5384(4)
c (Å)	13.692(13)	13.6467(8)	7.8514(11)	13.6200(4)	7.8400(8)	13.5973(9)	7.5929(6)
V (Å^3)	374.62(7)	371.62(3)	242.04(9)	369.89(9)	241.05(7)	366.60(8)	238.92(5)
Fe-O_2 (Å)	2.20	2.18	2.068	2.13	2.065	2.12	2.058
Fe-O_2-Fe	153.4°	153.25°	156.7°	152.9°	155.3°	152.02°	154.85°
R_{wp} %	2.95	3.01		3.36		3.34	
R_p %	2.12	2.20		2.40		2.50	

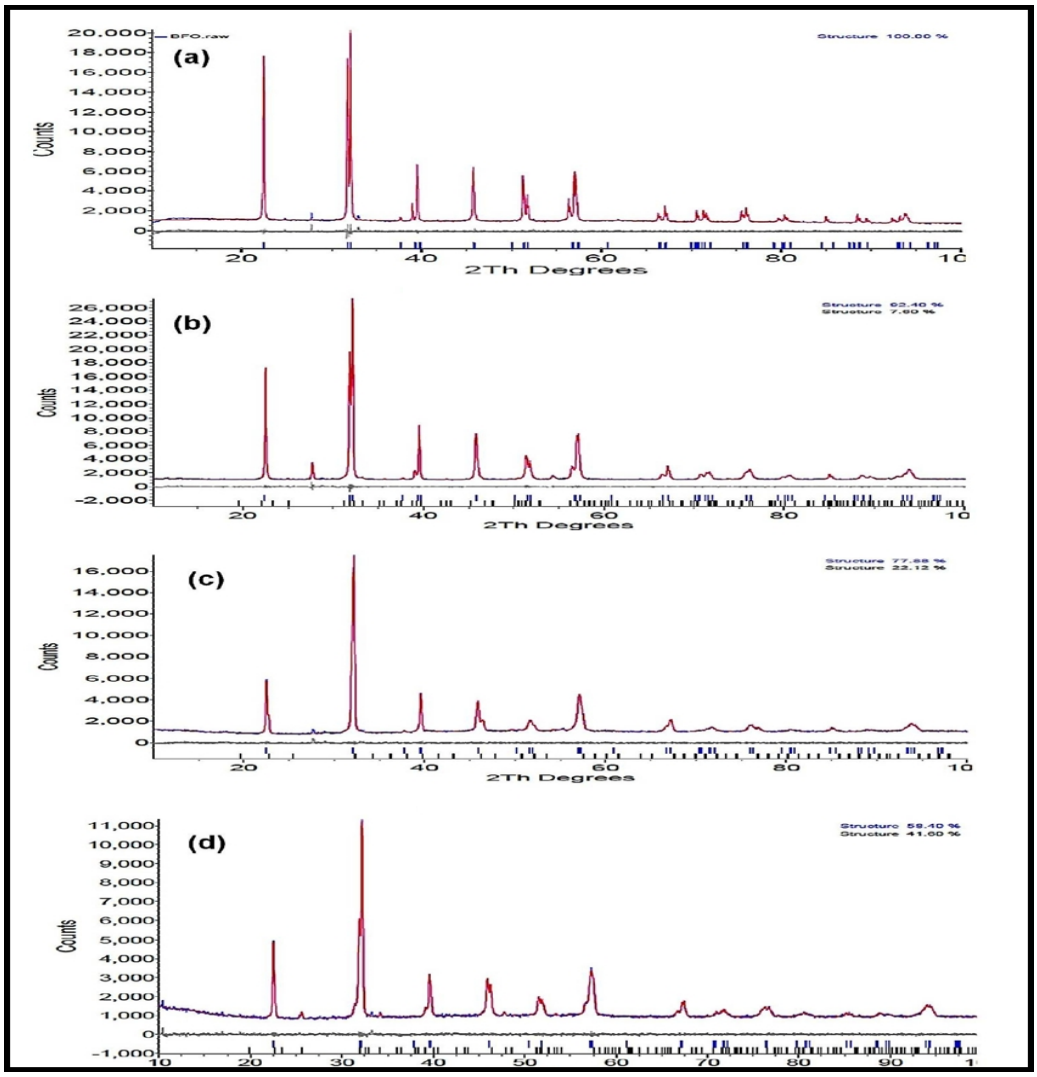

Figure 4.2 Rietveld refinement of the XRD data for LBFO samples (a) $x = 0$ (*R3c*), (b) $x = 0.05$ (*R3c* and *Pbnm*), (c) $x = 0.2$ (*R3c* and *Pbnm*), and (d) $x = 0.4$ (*R3c* and *Pbnm*). Observed (red lines), calculated (blue line), and difference (bottom line) profiles are shown. The Bragg reflections are marked by vertical bars. The upper bars in (b, c and d) correspond to *R3c* phase while the bottom bars to *Pbnm* phase.

4.3.2. Morphological studies

The field emission scanning electron micrograph (FE-SEM) of the LBFO sample is shown in figure 4.3. Microstructure shows an uniform grain distribution for the sample x = 0.05 and a non uniform grain distribution for other compositions x = 0.2, 0.3 and 0.4. The average grain size of the samples is found to be 0.25, 0.1, 0.2 and 0.21 μm. The average grain size of these samples is smaller than the undoped sample. However it is much more interesting if the grain size reduces below 62 nm, which is spin cycliod wave length of BFO. Also, the microstructure shows well densified samples with fewer voids.

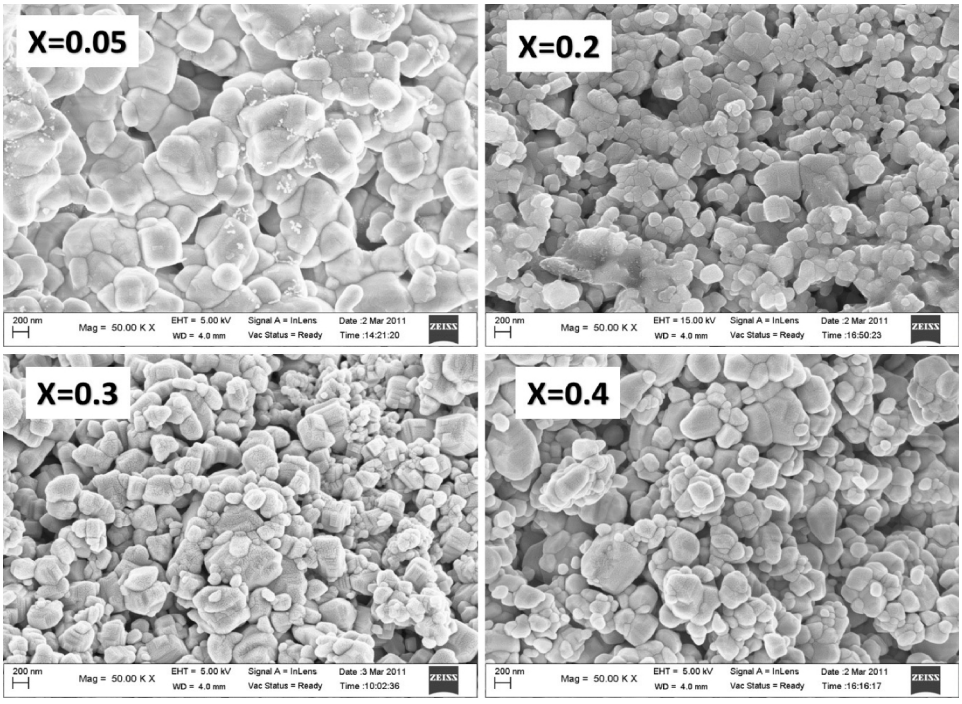

Figure 4.3 FE- SEM Images of LBFO samples.

The EDS spectra and its compositional analysis for these samples are shown in figure 4.4, indicates samples chemical homogenity and absence of any magnetic impurity.

Element	Weight%	Atomic%
O K	23.13	66.55
Fe K	26.17	21.57
La L	6.44	2.14
Bi M	44.26	9.75
Totals	100.00	

$x = 0.2$

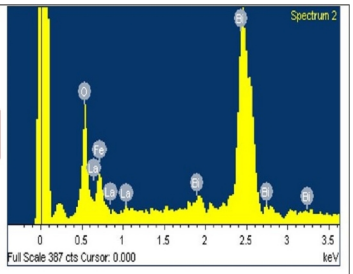

Element	Weight%	Atomic%
O K	16.91	62.54
Fe K	16.67	17.65
La L	7.01	2.99
Bi M	59.41	16.82
Totals	100.00	

$x = 0.3$

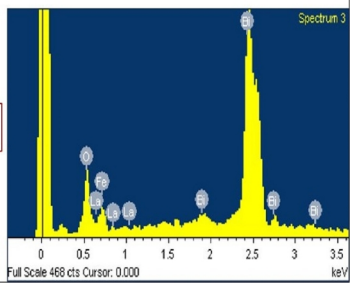

Figure.4.4 Elemental composition for LBFO samples from the EDS measurements.

4.3.3. Raman Spectroscopy

To confirm the systematic structural changes observed in XRD, we performed Raman Scattering measurements on $La_xBi_{1-x}FeO_3$ (x = 0.0 - 0.4). The Raman spectra of LBFO ceramics is shown in figure 4.5. The twelve normal modes of rhombohedral *R*3*c* $BiFeO_3$ sample are identified at 75.6, 136, 169, 215, 256, 278, 330, 367, 438, 465, 552 and 644

cm^{-1}. It is found that a new mode at 92 cm^{-1} is seen in all La doped samples, which is inactive in the sample. For $x > 0.15$, the vibrational modes at 215 and 465 cm^{-1} completely disappear whereas the 438, 552 and 644 cm^{-1} modes of BFO decrease with an increase in x. These changes reflect the change of Bi–O bond length with increasing x.

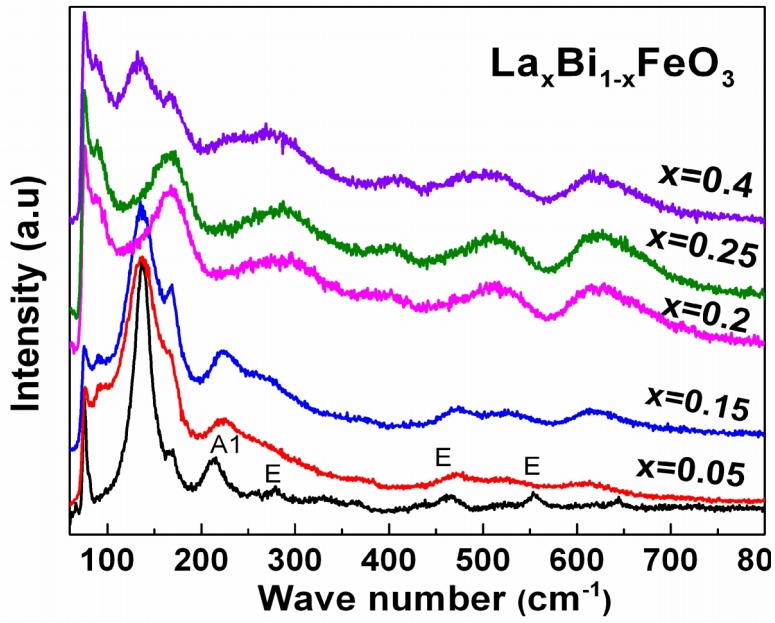

Figure 4.5. Room temperature Raman spectra of $La_xBi_{1-x}FeO_3$ (x = 0, 0.05, 0.2, 0.25, 0.4).

The mode at ~ 136 cm^{-1} is observed in all the samples (except for x = 0.2 and 0.25) which is due to the sizeable signature of *R3c* phase in La doped BFO. For the samples x = 0.2 and 0.25, this mode is inactive. The reoccurrence of 136 cm^{-1} mode in x = 0.4 indicates its active signature in the sample, confirms the presence of *R3c* phase in 40% doped sample is

agreement with the XRD data. Thus, Raman studies reconfirms substitution-induced structural phase transition from rhombohedral to orthorhombic as x increases in $La_xBi_{1-x}FeO_3$ samples.

4.3.4. Dielectric properties

The dielectric constant (ε_r) of $La_xBi_{1-x}FeO_3$ samples at room temperature in the frequency range of 20 Hz – 2 MHz is measured to investigate the variation of ε_r with La doping. The plot of frequency versus dielectric constant is shown in figure 4.6 (Note that the frequency is represented in log scale). ε_r of the undoped $BiFeO_3$ is 68 at 1 kHz and it decreases to 40 at 2 MHz. The ε_r values for LBFO are found to be 143, 90, 127, 160 and 144 for the compositions x = 0.05, 0.15 0.2, 0.25 and 0.4, respectively at the frequency of 1 kHz. Reducing the grain size to nano scale will increase the dielectric constant due to the large number of grain boundaries as scattering centers. However, in the present study, the influence of the grain size on the dielectric constant is not significant in these samples as the average grain size is above the nano scale range. Hence, the changes observed in dielectric constant are primarily due to the lanthanum doping. The improvement in the dielectric constant is due to the change in the structure, especially the variation of Fe–O bond length, which favors the off-centro symmetry with the substitution of lanthanum [11]. The dielectric constant decreases with an increase in

frequency and follows Debye law of frequency dispersion as it is nearly constant at very high frequencies [12]. A systematic enhancement in the dielectric constant is observed with La doping at lower frequencies. As the frequency increases to higher values, there is a crossover in the dispersion curves with doping level. Such a crossover was also seen in previous studies involving La, and Pb doped BFO systems [13, 14]. The inset of figure 4.6 shows the plot of dielectric constant at selected frequencies as a function of La concentration. There is a sudden increase in the dielectric constant for a small doping of x = 0.05. This sample does not show much variation of ε_r with frequency. Further, with an increase in La concentration, a decrease in ε_r is seen, nevertheless, this is higher than the undoped sample. The frequency dispersion of ε_r is higher for x = 0.2 and 0.25 samples.

The dielectric loss curves as a function of frequency are shown in the figure 4.7. It is interesting to note that La doping results the reduction in the dielectric loss due to the reduction in the leakage current in BFO system. The dielectric loss continually decreases as the La doping content increases. The improvement in the dielectric constant with a low dielectric loss for La doped BFO samples make them as a promising candidate for device applications.

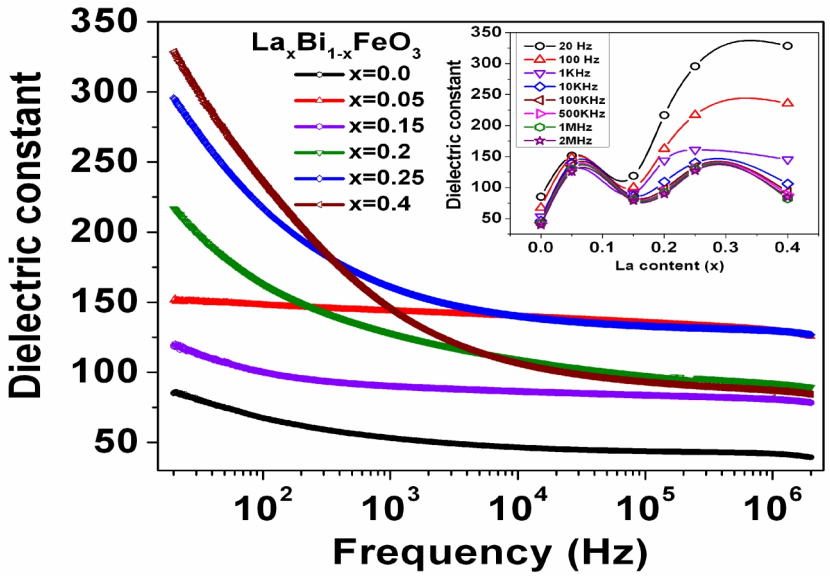

Figure 4.6 Dielectric constant (ε_r) verses frequency of $La_xBi_{1-x}FeO_3$ (x = 0, 0.05, 0.2, 0.25, 0.4) samples at 300 K. Inset shows the variation of ε_r with La content at selected frequencies.

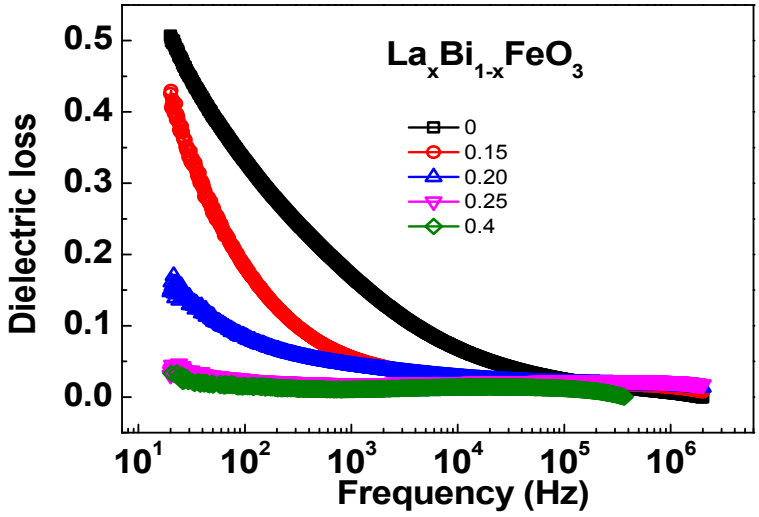

Figure 4.7 Dielectric loss verses frequency of $La_xBi_{1-x}FeO_3$ (x = 0, 0.05, 0.2, 0.25, 0.4) samples at 300 K.

4.3.5. Ferroelectric Measurements

P-E loops of La doped BFO is shown in the figure 4.8 for a particular composition x = 0.15. It is noted that with La substitution, BFO turns into a hard ferroelectric with electrical coercivity of 37 kV/cm and remanance polarization P_r = 2.81 μc/cm^2.

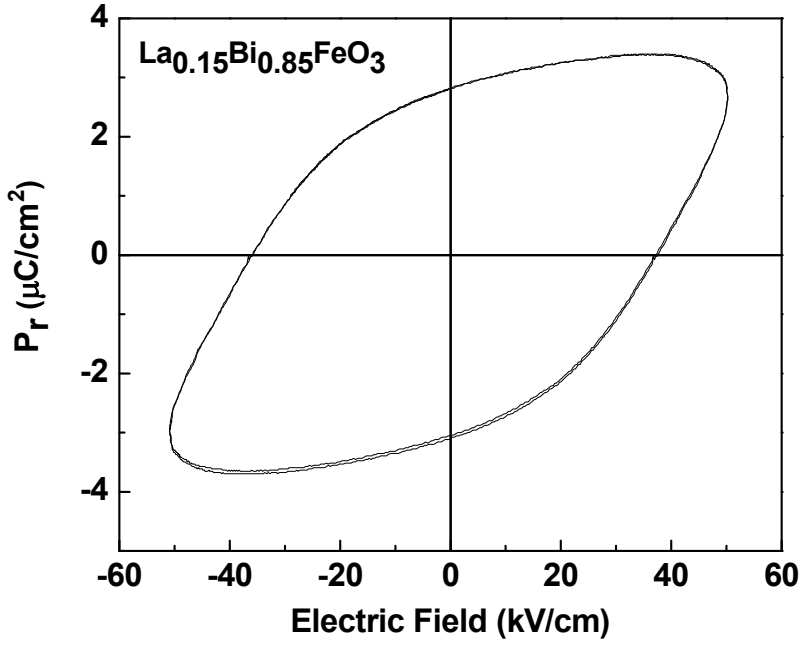

Figure 4.8 P-E loop of $La_{0.15}Bi_{0.85}FeO_3$ sample.

4.3.6. Magnetic properties

Figure 4.9 shows the magnetic hysteresis loops for the undoped and La doped $BiFeO_3$ system at room temperature. The M–H curve of BFO for an applied field of 7 T is nearly a straight line indicating the antiferromagnetic nature of $BiFeO_3$. As already discussed in chapter 3,

the canting of Fe^{3+} sublattice in $BiFeO_3$ results in a small residual magnetic moment but the appearance of ferromagnetism is suppressed by the spiral spin structure [15]. On the other hand, substitution of La into Bi results in weak ferromagnetism in $La_xBi_{1-x}FeO_3$. A significant enhancement in the remenant magnetization (M_r) and coercivity (H_C) is observed for these samples depending on the concentration of doping. As evident from table 4.3, M_r measured at 7 T increases continuously with x and exhibits a peak at x = 0.25. The room-temperature coercivity of pure BFO is 0.3 mT, whereas for doped samples, it is found to be 1.21, 1.39, 1.08 and 1.48 T for x = 0.05, 0.2, 0.25 and 0.4 respectively. A large H_C is observed in the La doped BFO samples. At 5 K (figure. 4.10), the H_C values are found to increase further to 1.34, 1.64, 1.25 and 1.24 T for x = 0.05, 0.2, 0.25 and 0.4 respectively. The increase in the H_C at low temperatures is due to the increase in anisotropy constant of these samples. The value of M_r reaches a maximum for x = 0.25 with a value of 0.3 emu/g and the increase in M_r indicates the alignment of Fe^{3+} magnetic moments with decrease in temperature. The magnetization (M) measured at 7 T increases linearly with x, and it reaches a maximum a value of 0.98 emu/g for x = 0.4. This is found to be slightly higher than the room-temperature value. Weak ferromagnetism can arise in $BiFeO_3$ when the particle/grain size reaches below its spin periodicity of 620 Å. Enhancement in the magnetic properties can also arise due to the

presence of small magnetic impurities. In the present study, the enhancement of the magnetization is intrinsic one as the grain size is much larger than its spin periodicity, and no ferromagnetic impurity is observed in EDS. This enhancement in the magnetization in general is attributed to the modification of spin structure from helical to the linear due to the interaction between Fe-Fe sub lattice, which results from a change in the canting angle arising from the Dzyaloshinskii–Moriya interaction [16, 17]. The Fe - O bond lengths decrease from 2.20 Å for x = 0 to 2.03 Å for x = 0.25 and the bond angle Fe-O-Fe decreases from 153.4° for x = 0.0 to 152.8° for x = 0.25. Due to this reduction in the bond lengths and bond angles between Fe and O, the spin structure of pure BFO gets modified in the doped samples. Similar results were observed by Rai et. al [18], where they attribute the occurrence of high H_C values to the structural distortion caused by canting effect or uncompensated anti-parallel sublattice magnetization with La doping . The huge coercivity of the order of 1-2 Tesla at room temperature is also observed in the other dopant systems [19, 20]. The high H_C of our samples can be due to the magnetocrystalline anisotropy, arising from the deformation of Fe sublattice due to the La doping [17]. Besides magneto crystalline anisotropy, the contribution from the magnetoelastic anisotropy [3], may also lead to the variation of H_C values with La concentration.

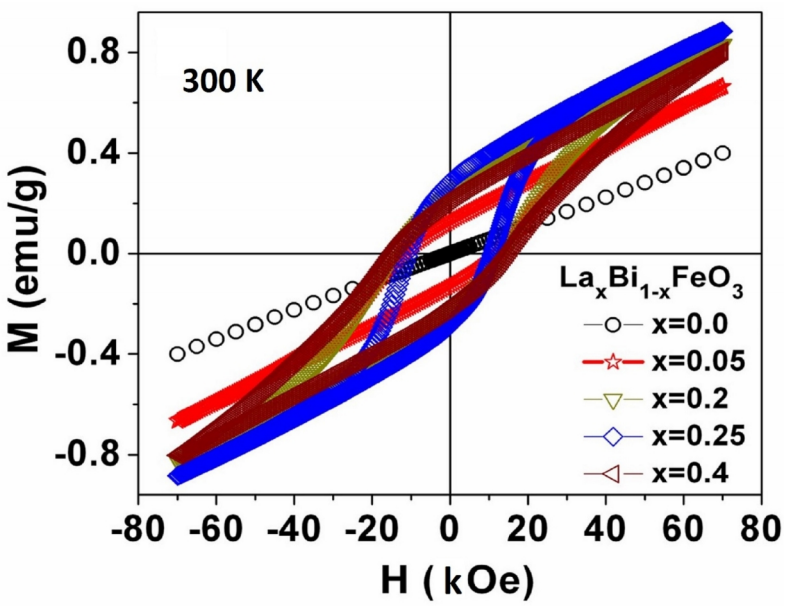

Figure 4.9 M-H loops of $La_xBi_{1-x}FeO_3$ (x = 0, 0.05, 0.2, 0.25, 0.4) at 300 K.

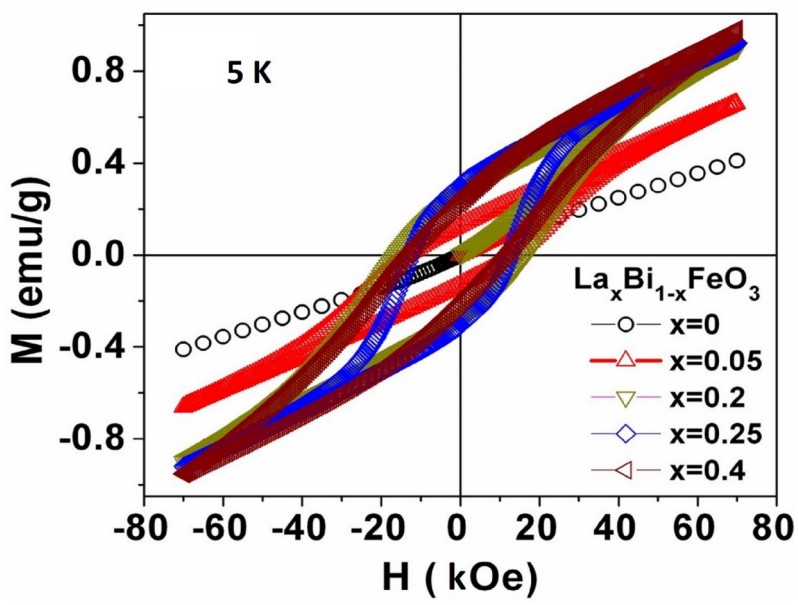

Figure 4.10 M-H loops of $La_xBi_{1-x}FeO_3$ (x = 0, 0.05, 0.2, 0.25, 0.4) at 5 K.

Table.4.3 Magnetic parameters for $La_xBi_{1-x}FeO_3$ samples at 5 K and 300 K.

Compound	H_C (T)		M_r (emu/g)		M at 7T (emu/g)	
	5 K	300 K	5 K	300 K	5 K	300 K
$x = 0$	$5x10^{-4}$	$3 x10^{-4}$	$6 x10^{-4}$	$5 x10^{-4}$	0.41	0.40
$x = 0.05$	1.34	1.21	0.13	0.13	0.66	0.66
$x = 0.2$	1.64	1.39	0.27	0.24	0.90	0.83
$x = 0.25$	1.25	1.08	0.30	0.28	0.92	0.88
$x = 0.4$	1.24	1.48	0.22	0.21	0.98	0.81

The 'field cooled' (FC) and 'zero field cooled' (ZFC) magnetization curves for LBFO samples are measured from 5 K - 300 K and also from 300 K - 850 K using high temperature oven option of PPMS to determine the effect of La doping on the ordering temperature. Figure 4.11 shows the M-T curve in the low temperature region 5 K - 300 K for an applied field of 500 Oe. It is clearly seen that magnetization increases as the temperature decreases for all the samples. Unlike pure BFO, La doped samples shows irriversability in this temperature region. A change in the slope of the curve is observed near 50 K in both ZFC and FC. A cusp at 50 K is observed in all the doped samples and also in the undoped BFO. This cusp can be attributed to the change in the spin configuration. That means the ferro magnetic component is increasning more as the system goes to lower temperatures. This is seen as the steep increase in magnetization below 50 K.

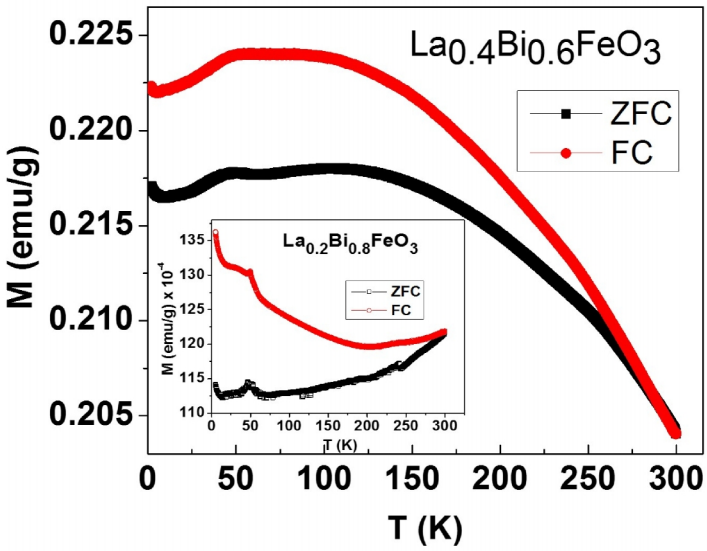

Figure 4.11 M-T curve of LBFO sample from 5 K-300 K.

The high-temperature ZFC-FC magnetization measured at 500 Oe is shown in figure.4.12. The magnetic transition is clearly seen in the M-T curves. Néel temperature (T_N) of the BFO is found to be 651 K. The value of T_N increases to 658.3 K for x = 0.2 sample. The increase in T_N is approaching the Néel temperature of $LaFeO_3$ (738 K) [21] with La doping (table.4.4), consistent with the reported ones [22]. In agreement with the low-temperature magnetization data, there is an increase in the magnetization with La doping content. All the samples show a large magnetic irreversibility M_{irr} given by (M_{FC} –M_{ZFC}) from the ordering temperature to room temperature.

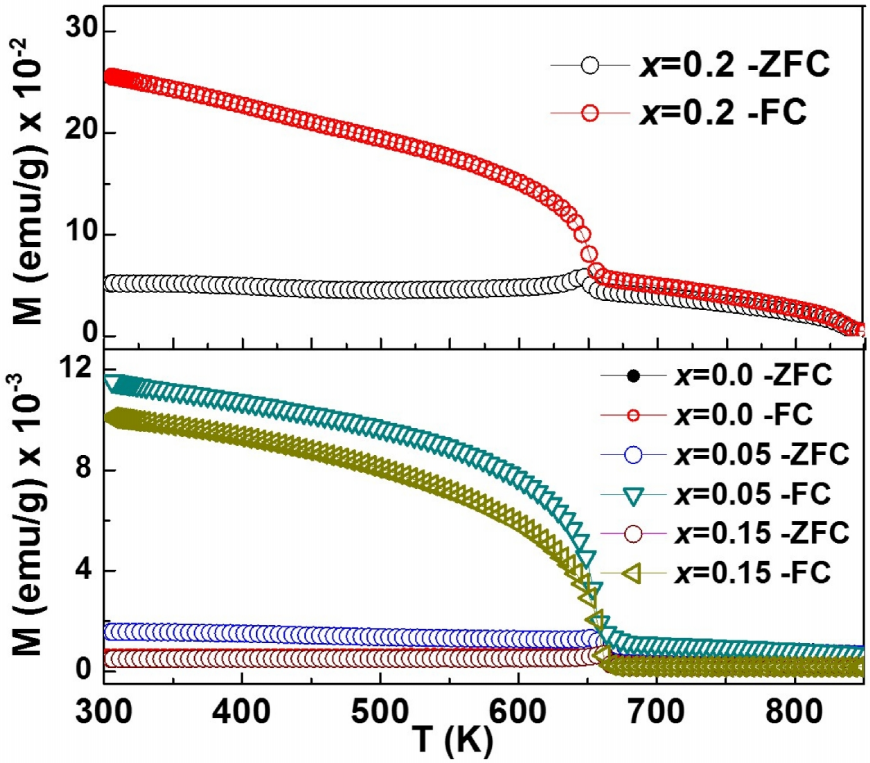

Figure 4.12. Temperature dependent magnetization curves (M-T) from 300 K to 850 K for $La_xBi_{1-x}FeO_3$ (x = 0, 0.05, 0.15 and 0.2) samples.

Table.4.4. T_N values for $La_xBi_{1-x}FeO_3$ samples.

Composition	T_N (K)
x = 0	651.0
x = 0.05	659.4
x = 0.15	662.6
x = 0.2	658.3

Conclusions

La doping helps in stabilizing the phase of BFO and results into a structural transition. Enhancement in dielectric constant with low dielectric loss is found with La doping. La improves the magnetic properties due to structural changes and modification of spin cyclic structure. T_N of the BFO samples increases as La doping content increases.

Effect of Gd doping on the multiferroic properties of $BiFeO_3$

4(b)

4.4. Introduction

The doping of a foreign atom at A-site of the ABO_3 structured BFO lattice plays a vital role in improving its properties. For example, as seen in the previous section, substitution of Bi^{3+} with rare-earth element La^{3+} results in phase stabilization, reduced dielectric loss, remarkable improvement of the dielectric and magnetic properties of BFO, which eventually leads to the enhancement of magneto electric effect. Among RE elements, Gd^{3+} ($4f^7$) is a magnetically active ion (μ = 7.8 μ_B) and has the largest number of unpaired electrons. Doping with Gd^{3+} in BFO is remarkable as it results in a huge structural distortion due to the large ionic radii mismatch at A-site and introduces additional magnetic interaction between Gd^{3+} and Fe^{3+}, improving magnetic properties even for small doping concentration. In the literature, Khomchenko et al [23] found a structural modification in $Gd_xBi_{1-x}FeO_3$ (GBFO) with Gd composition as *R3c*→*Pn21a* for $x \sim 0.1$ and *Pn21a*→*Pnma* for $0.2 < x < 0.3$. It is also reported [24] that GBFO has *R3c* structure for $x < 0.08$, *Pbnm*

structure for $x \geq 0.3$ and both the phases coexist for $0.08 < x < 0.3$. Furthermore, a two phase structural model is used to quantify the structural changes in Gd doped BFO nanoparticles [25, 26]. However, a detailed structural analysis on phase transition and the quantitative details of the phases present in the bulk system with the Gd doping are still lacking. Hence it is proposed to investigate the quantitative refinement of the phases and its influence on the dielectric and magnetic properties of GBFO samples.

The present section is aimed to understand (i) the structural transition with respect to the Gd content, (ii) the dielectric properties and (iii) enhanced magnetic behaviour of these compounds. To achieve above mentioned objectives, we have prepared the GBFO samples and used the two phase structural model by considering the (*R3c*+*Pn21a*) and (*R3c*+*Pnma*) to refine the structure for the bulk samples and estimated the quantitative results of these phases of $Gd_xBi_{1-x}FeO_3$ (x = 0.0 - 0.35). The observed structural changes are correlated with Raman, dielectric and magnetic studies on these samples.

4.5. Experimental Details

The ceramics of $Gd_xBi_{1-x}FeO_3$ (GBFO) for x = 0, 0.05, 0.1, 0.15, 0.2, 0.25, 0.3 and 0.35 were prepared by conventional solid-state reaction method. Stoichiometric ratios of Bi_2O_3, Gd_2O_3 and Fe_2O_3 powders were used as the starting chemicals to synthesis through solid state reaction.

The pellets of the samples after annealing are characterized for structural, electrical and magnetic properties.

4.6. Results and Discussion

4.6.1. Structural Analysis and Morphology

The effect of the Gd doping on the BFO structure is analyzed using X-ray diffraction (XRD). The obtained XRD pattern of $Gd_xBi_{1-x}FeO_3$ for x = 0 - 0.35 samples are shown in figure 4.13. The pure BFO is easily indexed as rhombohedral with the space group of *R3c*. As the Gd concentration increases, noticeable features are observed in the diffraction pattern. The enlarged XRD pattern between 31°- 34° is presented in the inset of figure 4.13, which shows the split reflections of (1 0 4) and (1 1 0) merge into a single broad peak with a shift towards higher 2θ value. This is a clear indication of structural modification due to the lattice distortion caused by Gd doping. Similarly, additional peaks corresponding to the new phase of $GdFeO_3$ are also observed in the XRD pattern (marked by hash #). Besides, a small secondary phase corresponding to $Bi_{25}FeO_{40}$ is present in the entire diffraction pattern (marked by asterisk *) which is not ferromagnetic in nature at room temperature [27]. Our observations are consistent with recently reported rare earth doped BFO systems [28, 29]. Rietveld refinement of the XRD patterns (figure 4.14) of these samples was carried out and the structural

parameters obtained are listed in table 4.5. For pure BFO (x = 0), the structure is directly refined by considering the single input model of *R3c* symmetry resulting in the refined lattice parameters, $a = b$ = 5.6207 Å, c = 13.6923 Å and the corresponding cell volume (V) is found to be 374.62 $Å^3$. A similar refinement result as of the pure BFO is obtained for x = 0.05 but the lattice parameters are slightly reduced and listed in table 4.5.

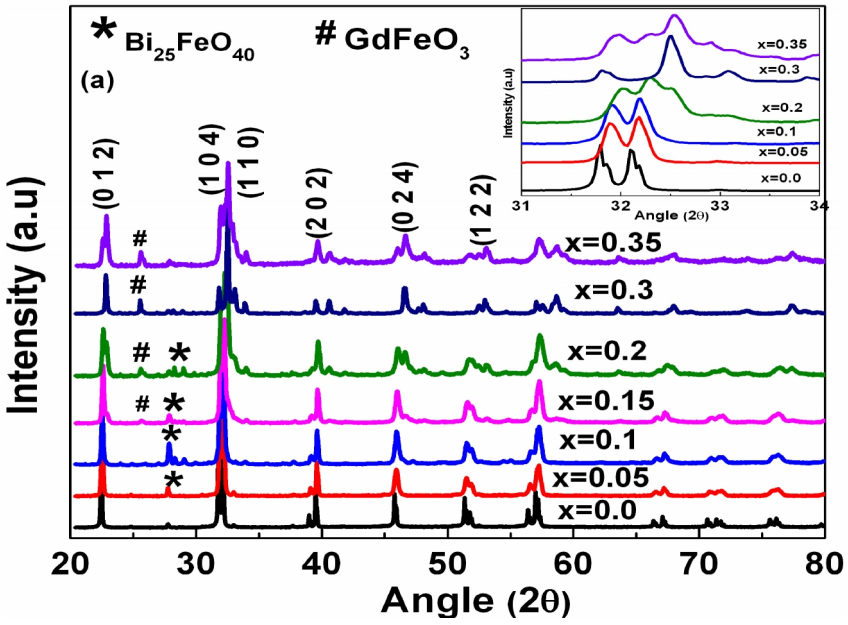

Figure 4.13. XRD data for GBFO samples (Inset shows the magnified data around 32°).

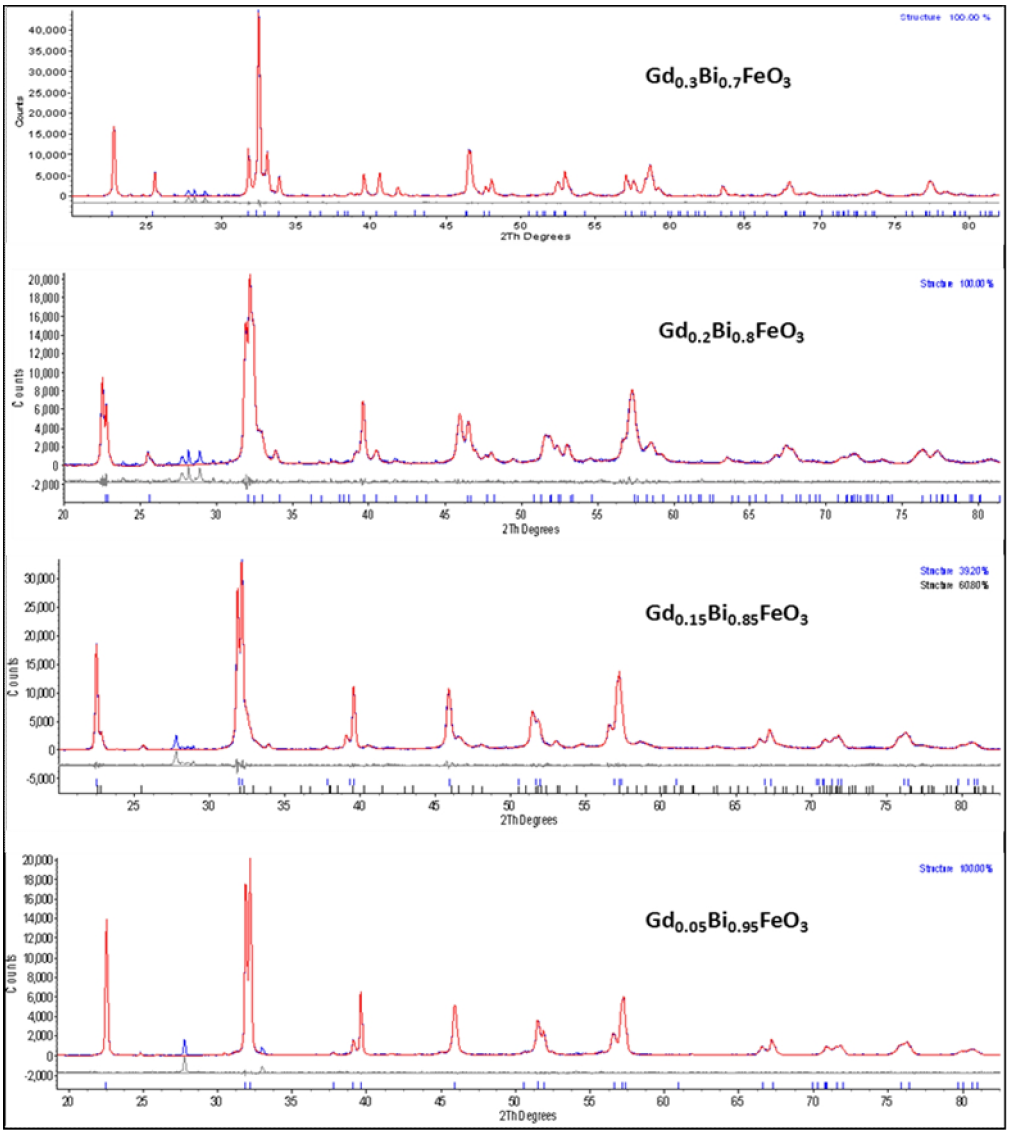

Figure 4.14 Rietveld refinement of the XRD data for GBFO samples. Observed (red lines), calculated (blue line), and difference (bottom line) profiles are shown. The Bragg reflections are marked by vertical bars. The bars correspond to structure phase.

However, the structure started modifying from rhombohedral (*R3c*) to orthorhombic for $0.1 \leq x \leq 0.15$. Samples with higher composition, i.e. for $x \geq 0.1$ are refined with a two-phase model, because a structural change in GBFO is anticipated from rhombohedral (*R3c*) to orthorhombic (either *Pn21a* or *Pnma*) as the end compound, $GdFeO_3$ exists in orthorhombic structure. Hence along with the *R3c* phase, *Pn21a* and *Pnma* phases are considered for refinement. However, the two phase input model with *R3c*+*Pn21a* was found to fit better than *R3c* as well as *R3c*+*Pnma* structure models for $0.1 \leq x \leq 0.15$. For $x = 0.1$, the *R3c* phase is prominent with ~77% and *Pn21a* phase is ~22%. Further for $x = 0.15$, the *Pn21a* phase is prominent with ~60% and the *R3c* phase decreases to ~39%. The *Pn21a* and *Pnma* structure models fits better for $x = 0.2$, 0.3 and 0.35 respectively. The phase transition in the BFO with Gd can be understood from the lattice contraction caused by the low ionic radii of Gd^{3+} (r = 1.05 Å) over Bi^{3+} (r = 1.14 Å). These structural classifications are in accordance with earlier reports [25, 26, 30].

Lattice parameters and volume of the GBFO system obtained from the Rietveld refinement method are plotted in figure 4.15 as a function of Gd content. The lattice parameter '*c*' is slightly varying up to $x = 0.1$ and later it rapidly decreases for further Gd content. The lattice parameter '*b*' increases to higher values from $x = 0.1$ whereas the lattice parameter '*a*' is almost constant when compared to '*b*' and '*c*'. The

variations of the lattice parameters resulted in the volume collapse of the structure as Gd content increases as shown in the inset of figure 4.15.

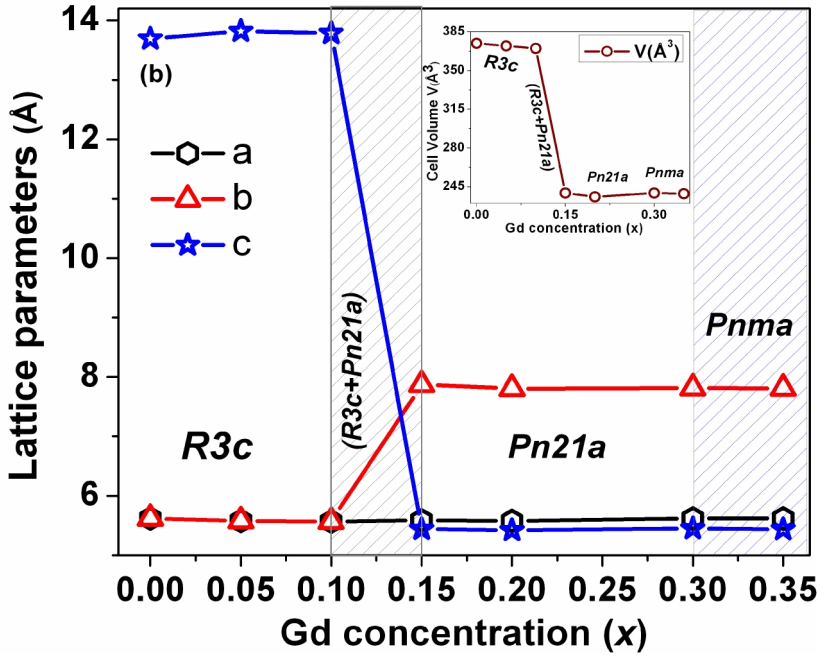

Figure 4.15 Lattice parameters verses Gd content plot for $Gd_xBi_{1-x}FeO_3$ (x = 0, 0.05, 0.1, 0.15, 0.2, 0.3 and 0.35).

The increase in the lattice parameter '*b*' indicates the presence of Gd-Bi and Gd-Fe interactions brought by Gd in the structures whereas the reduction in the c values can be attributed to the low ionic radius of Gd when compared to Bi. It is clearly seen from the figure 4.15, that $a = b \neq c$ is modified to $a \neq b \neq c$ and the reduction in the volume is a clear signature of the structural transition.

Table 4.5. Refined structural parameters for $Gd_xBi_{1-x}FeO_3$ (0, 0.05, 0.1, 0.15, 0.2,0.3 and 0.35) samples.

Compound	Structural Model	*a*(Å)	*b*(Å)	*c*(Å)	*V*(Å^3)	Fe-O_2-Fe (°)	Bi-O_2 (Å)
x = 0.0	*R3c*	5.620(3)	5.620(3)	13.69(8)	374.62(5)	153.42	2.88
x = 0.05	*R3c*	5.577(6)	5.577(6)	13.82(4)	372.3(3)	153.02	2.85
x = 0.1	*R3c* (77.64 %)	5.567(8)	5.567(8)	13.78(7)	370.02(9)	152.81	2.82
	Pn21a (22.35 %)	5.592(7)	7.879(3)	5.443(8)	239.84(3)	158.42	2.54
x = 0.15	*R3c* (39.19 %)	5.562(6)	5.562(6)	13.73(4)	368.1(5)	152.04	2.80
	Pn21a (60.80 %)	5.587(8)	7.87(12)	5.439(9)	239.23(7)	157.36	2.31
x = 0.2	*Pn21a*	5.57(13)	7.805(7)	5.418(2)	235.79(3)	156.44	2.26
x = 0.3	*Pnma*	5.620(8)	7.81(16)	5.44(19)	239.28(4)	148.58	2.15
x = 0.35	*Pnma*	5.619(9)	7.810(8)	5.43(10)	238.63(6)	143.02	2.20

4.6.2. Microstructural properties

In order to find the grain size distribution in Gd doped BFO, the morphology of GBFO has been studied using FE-SEM. The microstructure for different Gd compositions is shown in figure 4.16(a). It is observed that all the samples are granular and dense. For x = 0.1, the sample is homogeneous with rectangular grains having an average grain size of 1.2 μm. This grain size reduces to ~ 0.5 μm for x = 0.15 and 0.2. For $x \geq 0.3$, the clusters were aggregated and the size of the grain increased to ~ 2.1 μm. It is clear that the grain growth found to be suppressed up to certain concentration (x = 0.2) and on the further increase in x, grains start growing and helps in densification. The

chemical compositions of pure and doped BFO samples were determined using EDS technique and presented in figure 4.16(b). Besides the obvious signals for O, Bi, and Fe elements, the EDS spectra shows a weak signal of Gd in the doped samples. Moreover, the EDS analysis confirms that the chemical composition of GBFO is nearly in stoichiometric ratios.

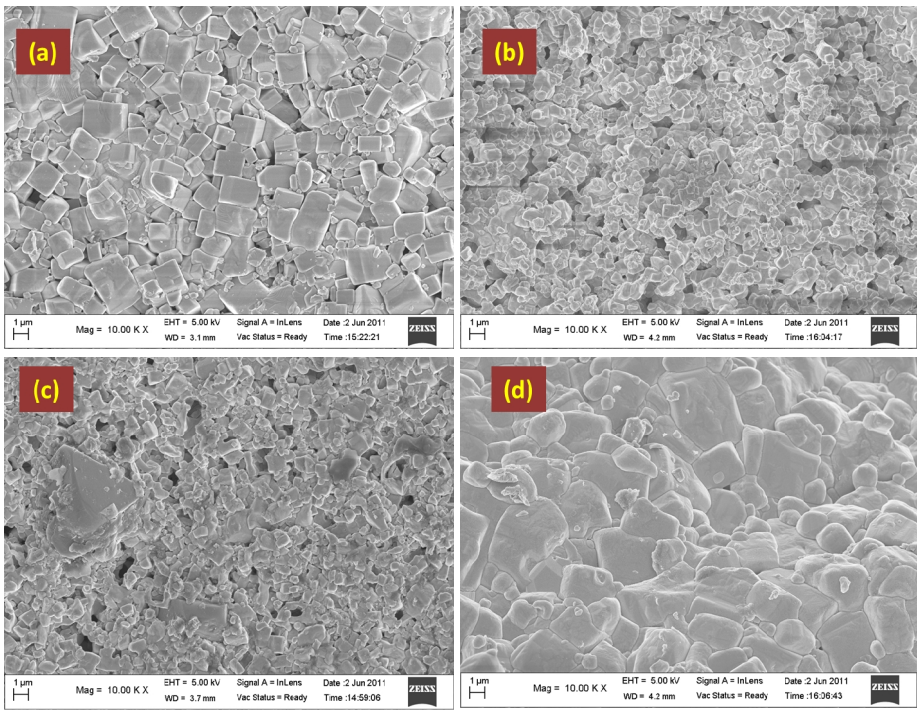

Figure 4.16(a) FE- SEM Images of $Gd_xBi_{1-x}FeO_3$ (a). x = 0.1, (b) x = 0.15, (c) x = 0.2 and (d) x = 0.35.

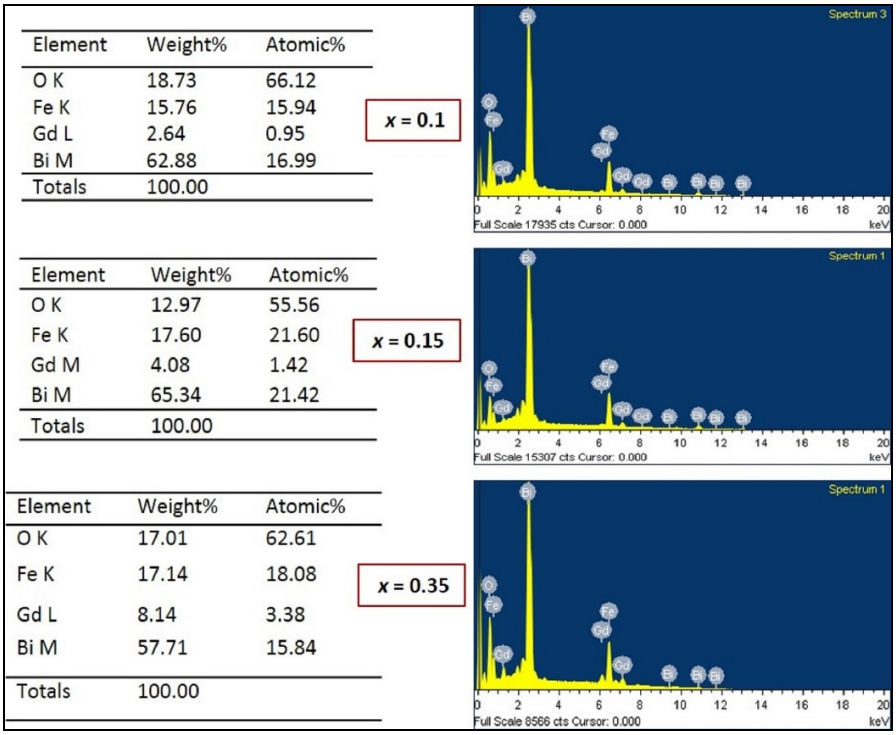

Figure 4.16(b) EDS spectra and elemental composition of GBFO samples.

4.6.3. Raman Spectroscopy

The Raman spectra of GBFO for different Gd concentrations are shown in figure 4.17. Twelve active Raman modes are observed for $x = 0$, which are assigned as $4A_1 + 8E$ phonon modes. The four A_1 modes are assigned to 136 (M3), 169 (M4), 215 (M5) and 438 (M11) cm^{-1}. The eight E modes are assigned to 75 (M1), 256 (M6), 278 (M7), 330 (M9), 367 (M10), 465 (M12), 552(M13) and 644 (M14) cm^{-1}. All the mode frequencies as a function of Gd content are plotted in figure 4.18. It is observed that some of the modes M1, M5, M6, M7, M9, M11 and M12 of parent phase found

to disappear as Gd concentration increases and only seven ($3A_1$+ 4E) modes are present in the GBFO samples. It is noted that new mode frequencies at 95 (M2) and 300 (M8) cm^{-1} are observed in all the samples. The modes M3, M14 and M13 decrease with the Gd content, whereas the modes M4 and M10 increase. The low-frequency modes M1, M2, M3 and M5 are attributed to the Bi-O bonds; the intensity of these modes decreases with increasing Gd concentrations.

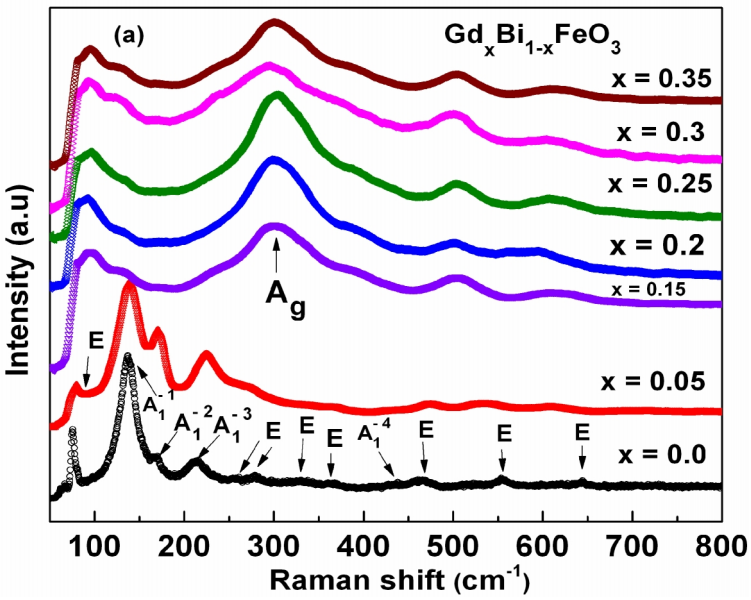

Figure 4.17. Raman spectra of $Gd_xBi_{1-x}FeO_3$ (x = 0, 0.05, 0.15, 0.2, 0.25, 0.3 and 0.35) samples.

The shift in the M3 mode is due to the decrease in Bi-O bond length (see table 4.5) with an increase in x. The disappearing of the M1 and M3 modes indicates that some of Bi-O bonds are missing due to the

introduction of Gd. Due to the presence of Gd, a new peak (A_g) with high scattering intensity around 300 cm^{-1} is observed for all the doped samples, which is related to $GdFeO_3$ orthorhombic phase [31, 32]. The shift in the Raman peaks and appearance of new modes suggest that the structural phase transition occur from rhombohedral to orthorhombic phase as Gd substitutes Bi, which confirms the XRD results.

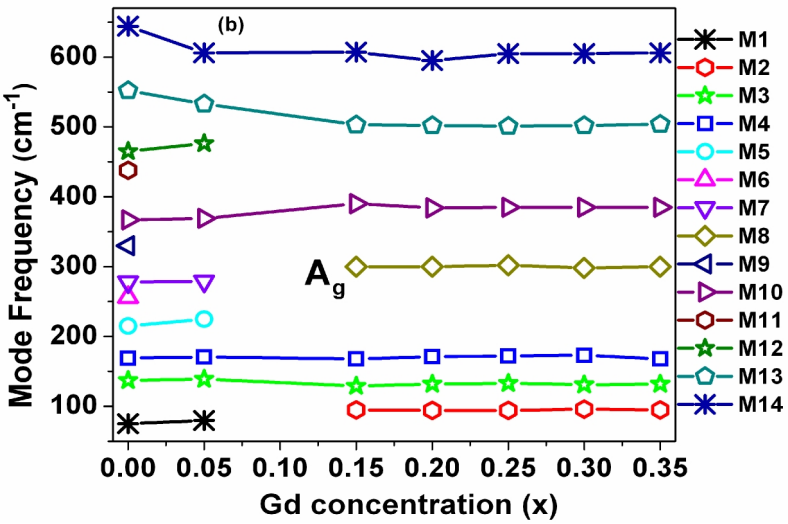

Figure 4.18 Raman mode frequency verses Gd concentration of $Gd_xBi_{1-x}FeO_3$ (x = 0, 0.05, 0.15, 0.2, 0.25, 0.3 and 0.35) samples.

4.6.4. Dielectric properties

Figure 4.19 shows the variation of dielectric constant (ε_r) of GBFO samples as a function of frequency from 20 Hz to 2 MHz. The dielectric constant of all the samples decreases with an increase in frequency and

follows the general relaxation. There is a remarkable enhancement in the value of the dielectric constant with increasing Gd substitution. The dielectric constant increases to 200 at 1 kHz for x = 0.05 which is four times higher than that of pure BFO. As Gd^{3+} content increases, the dielectric constant also increases and reaches the maximum value of 900 at 1 kHz for x = 0.1. However, a non-systematic increase in ε_r is observed with x. The enhancement in dielectric constant can be understood in terms of the ferroelectric off-centering distortion. The ferroelectric off-centering distortion is due to the change in crystal structure brought about by the Gd ions whose ionic radius is smaller than Bi^{3+} ion. This leads to the change in the Fe-O bond length and hence the distortion of FeO_6 octahedron cage. The distortion in FeO_6 cage is predominantly responsible for the increase in polarization; thereby increase in dielectric constant [11]. GBFO sample with doping concentration, x = 0.1 has the highest value of dielectric constant compared with other samples. The maximum ε_r is due to the presence of (*R3c*+*Pn21a*) polar phase. On the further increase in Gd content to $x \geq 0.3$, ε_r decreases, this is due to reduction of the unit cell volume and thereby causes less freedom of Fe^{3+} electron displacement in the FeO_6 octahedron [13]. This is also due to the non-polar *Pnma* symmetry for x = 0.3 and 0.35. The inset of figure 4.19 shows the compositional dependence of dielectric constant in $Bi_{1-x}Gd_xFeO_3$ (x = 0 - 0.35) ceramics. As described above the dielectric

constant is maximum for x = 0.1 and minimum for x = 0.3, and the compositional dependence has the same trend for all the frequencies.

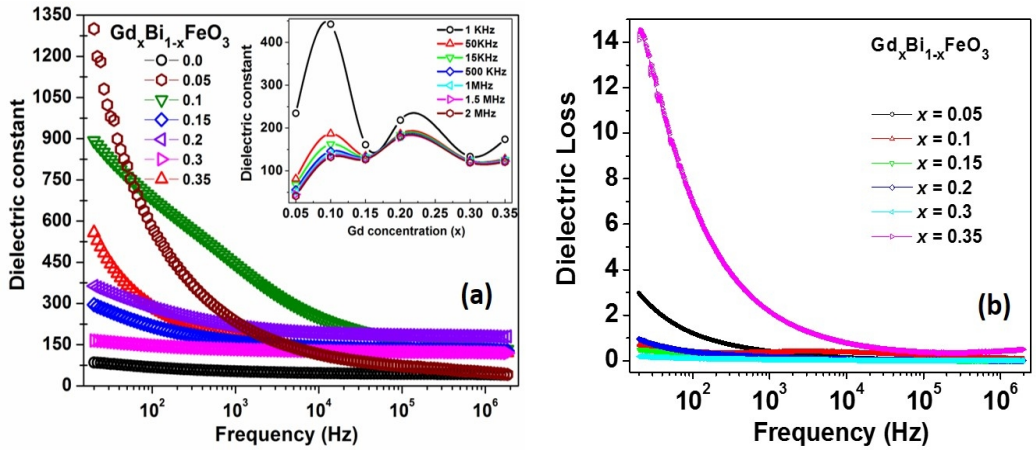

Figure 4.19 (a). Dielectric constant vs. frequency and (b). Dielectric loss vs. frequency of $Gd_xBi_{1-x}FeO_3$ (x = 0, 0.05, 0.1, 0.15, 0.2. 0.3 and 0.35) samples at 300 K (Inset of figure shows dielectric constant verses Gd doping concentration for different frequencies).

The dielectric loss of these samples shown in the figure 4.19(b) reveals that as compared with the undoped BFO system, the loss is more for Gd doped samples. This trend is opposite to the behavior of La doped samples, where a decrease in the dielectric loss is observed. Thus, even though Gd improves the dielectric constant, it also increases the loss which is undesirable for the device applications.

Temperature dependent dielectric measurements on the sample x = 0.05 is shown in the figure 4.20. As the temperature increases the dielectric constant increases and a change in slope is observed for all the

frequencies around 370 °C. This temperature corresponds to the T_N of BFO. That means an indirect coupling between the spin and electric field is seen in this system. This is observed for all other doping concentrations, revealing the presence of magneto electric effect in these samples.

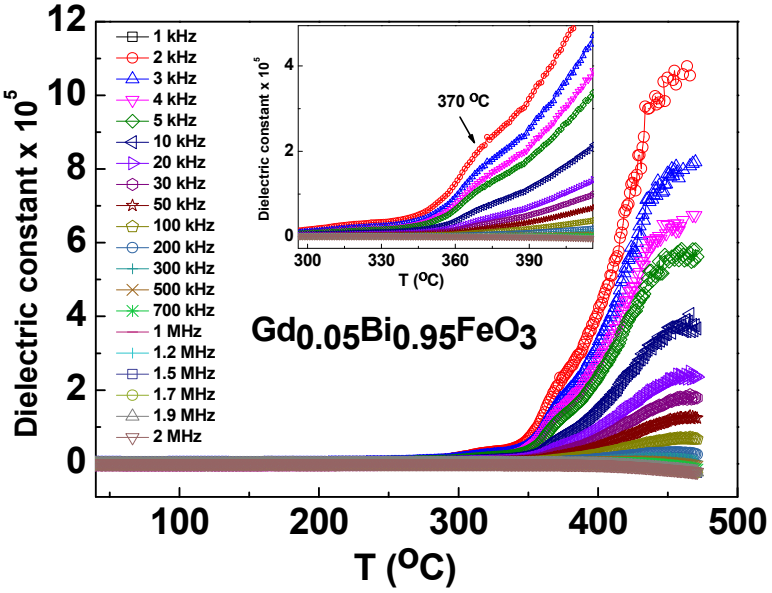

Figure 4.20 Dielectric constant versus Temperature for different frequencies.

4.6.5. Ferroelectric measurements

The electric field induced polarization of these samples x = 0.1 – 0.3 are measured and corresponding loops are shown in figure 4.21. The polarization increases remarkably with Gd doping. The remnant polarization increases to 2.26 μC/cm² for x = 0.1, which is maximum and

for 30 % Gd a decrease in the P_r value to 1.13 μC/cm² is observed. The variation of the polarization with respect to the Gd doping content is in accordance with the dielectric results and the same explanation is valid here.

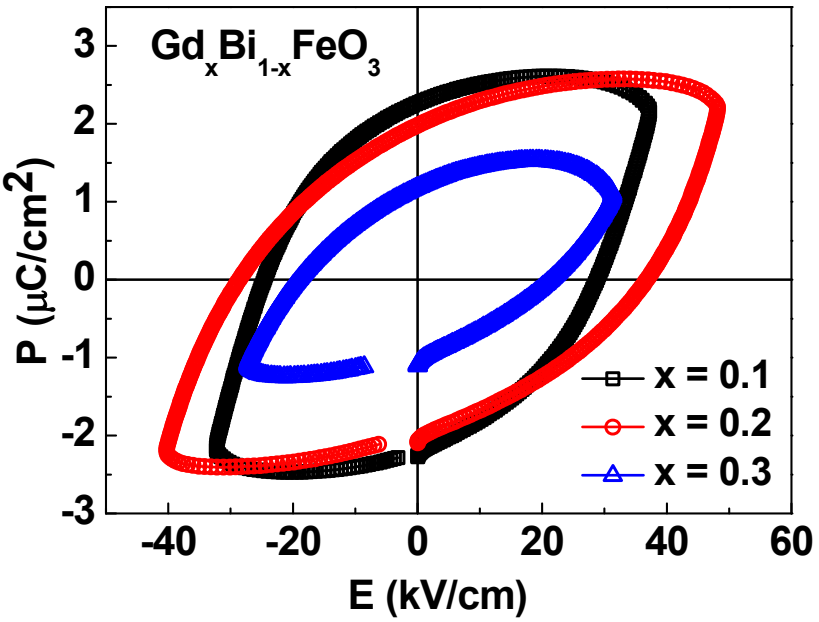

Figure 4.21 P-E loops of $Gd_xBi_{1-x}FeO_3$ samples (x = 0.1, 0.2 and 0.3).

4.6.6. Magnetic properties

The field and temperature dependent magnetic properties of GBFO are measured as a function of Gd content to understand the different magnetic interactions involved in the system. The magnetic hysteresis loops recorded for an applied field of 5 T at 300 K are shown in figure 4.22(a). The hysteresis loop for the pure BFO is almost a straight line

indicating its antiferromagnetic behaviour and the M_r value is 5.08 x 10^{-5} emu/g. Since Gd has a high magnetic moment of 7.8 μ_B, a small amount of Gd doping introduces additional magnetic contributions to the existing interactions between Gd-Fe ions and Gd-Gd ions in pure BFO. These interactions bring dramatic changes in the M-H hysteresis loops. A remarkable enhancement in the magnetization is observed for x = 0.05 and the value of M_r increases to 0.15 emu/g and H_C to 0.2 T. A decrease in the magnetization is observed for further doping levels up to x = 0.15. When x = 0.2, the magnetization increases and reaches a maximum value of 0.255 emu/g (see figure 4.22(a)). Although saturation of magnetization is not observed even up to 5 T magnetic field, the antiferromagnetic nature of BFO turns to the ferromagnetic as values of M_r as well as H_C enhance with Gd doping. The enhancement in the magnetization is primarily due to the modification of the spiral spin structure into linear caused by the decrease in the Fe-O-Fe bond angles (table 4.5). The interaction between Gd^{3+} and Fe^{3+} also contributes for the higher magnetization values in comparison to the other non-magnetic rare earth doping systems. The low temperature magnetic hysteresis loops recorded at 5 K are shown in figure 4.22(b). The magnetic moment is greatly enhanced at 5 K compared to 300 K due to the ordering of the spins. The magnetic moment at 5 T increases to 36.3 emu/g for x = 0.05 and reaches a maximum of 36.9 emu/g for x = 0.3, these are similar to the

trends observed at 300 K. The magnetization values of the present study are higher than the earlier reports on Gd doped BFO [33].

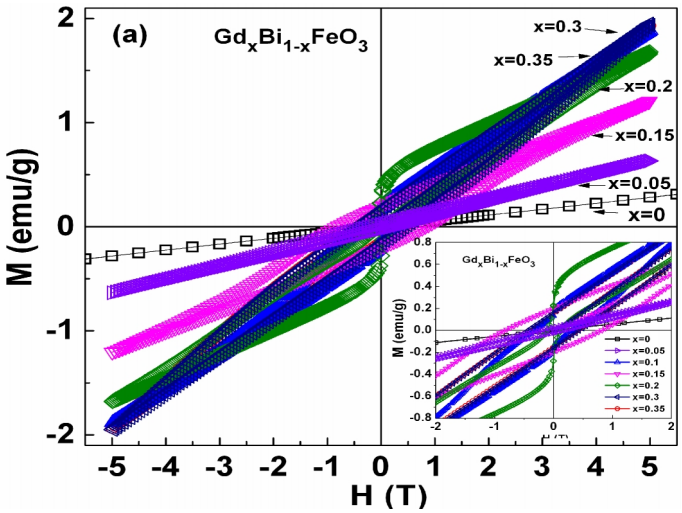

Figure 4.22(a) M-H loops of GBFO (x = 0, 0.05, 0.1, 0.15, 0.2, 0.3 and 0.35) at 300 K.

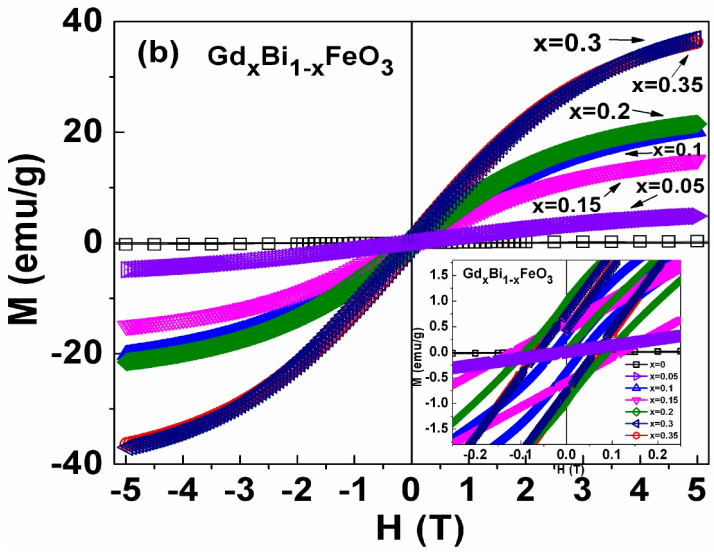

Figure 4.22(b). M-H loops of GBFO (x = 0, 0.05, 0.1, 0.15, 0.2, 0.3 and 0.35) at 5K.

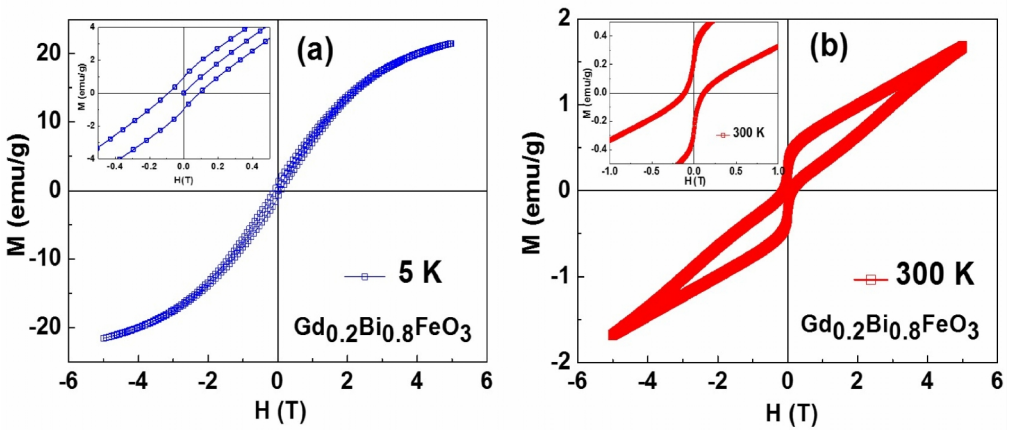

Figure 4.23. M-H loops of $Gd_xBi_{1-x}FeO_3$ (x = 0.2) at (a) 5K and (b) 300 K.

Figure 4.23 shows an enlarged M-H loops for the x =0.2 sample. An interesting double hysteresis loop is observed at RT for this sample with a minimum H_C value of 1.15 kOe. This double hysteresis kind of loop is not observed for the loops measured at 5 K. In general, such kind of loops is typical to the orthoferrites as the structure changes to *Pnma* [34].

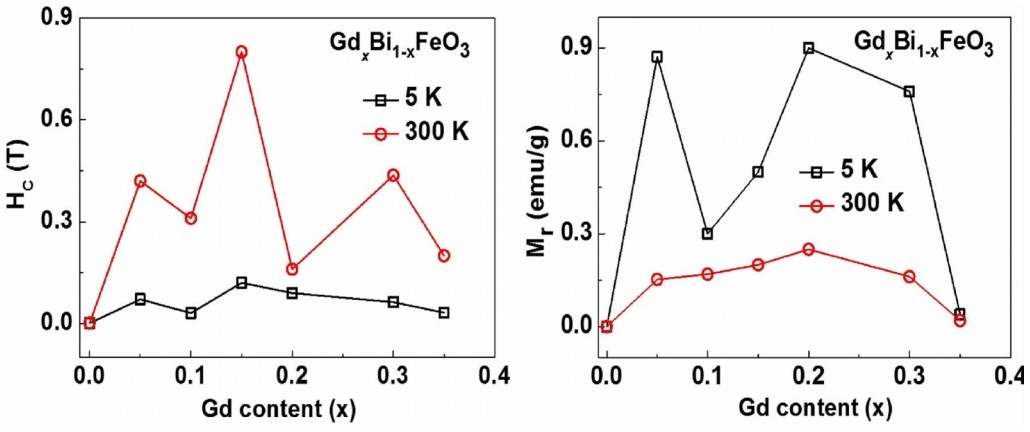

Figure 4.24 Variation of H_C and M_r for different doping levels in $Gd_xBi_{1-x}FeO_3$.

The variation of H_C at 5 K and 300 K as a function of Gd doping composition is shown in the figure 4.24. From the figure, two phenomenological observations are made; firstly, non-uniform variation of H_C with the doping level at both temperatures and secondly, the value of H_C is higher at 300 K compared to 5 K. This can be understood in terms of sub lattice model, which will be discussed at the end of this chapter.

The ZFC and FC measurements are carried out in two different temperature ranges namely 5 K - 300 K (figure 4.25(a)) and 300 K - 850 K (figure 4.27) in an applied field of 500 Oe. A sudden upturn in the magnetization is observed below 50 K for all the samples. This can be attributed to the ordering of magnetic moment of Gd^{3+}. Similar results are observed in the previous studies [23, 26]. The value of the magnetization increases from 0.015 emu/g for x = 0 to 0.89 emu/g for a small amount of Gd doping, x = 0.05, and it reaches a maximum of 1.31 emu/g for x = 0.3 at 5 K. These variations in the magnetization can be attributed to the change in Fe-O-Fe bond angle and the contribution from the canted antiferromagnetic moments of Fe sub lattice arising due to the change in the crystal structure. Our refinement results show a decrease in the bond angle and bond lengths with x (table 4.5) indicating the structural transformation.

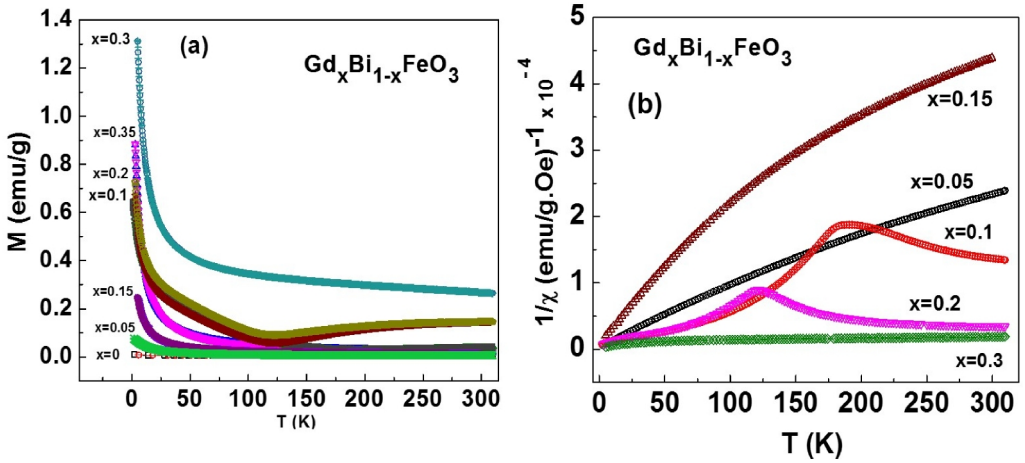

Figure 4.25 (a). M-T curve at an applied field of H = 500 Oe. (b). $1/\chi$ versus T graph for GBFO samples.

The careful observation of the M-T curves shows a minimum at 180 K and 140 K for the x = 0.1 and 0.2 respectively. This is seen more clearly as a hump in the $1/\chi$ versus T curves (figure 4.25 (b)). The frequency dependent on these samples at an ac amplitude of 10 Oe is investigated and a representative figure for x = 0.2 is depicted in figure 4.26. Ac susceptibility measurements do not show any slope changes in the magnetization curve and no frequency dependence is observed, which rules out the possibility of observation of spin glass nature in this system.

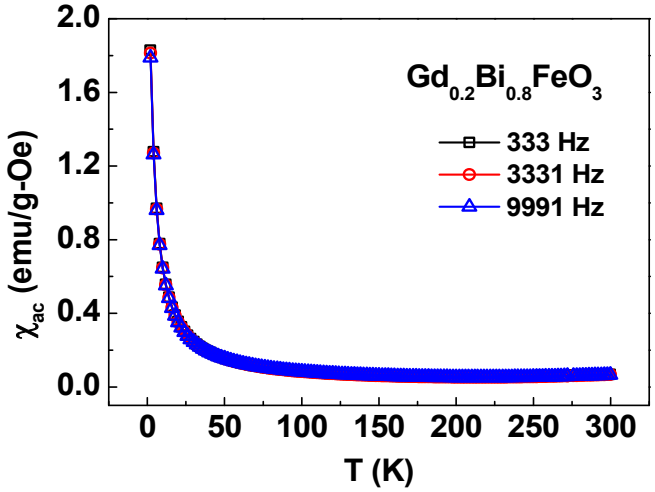

Figure 4.26 ac susceptibility of GBFO for x = 0.2.

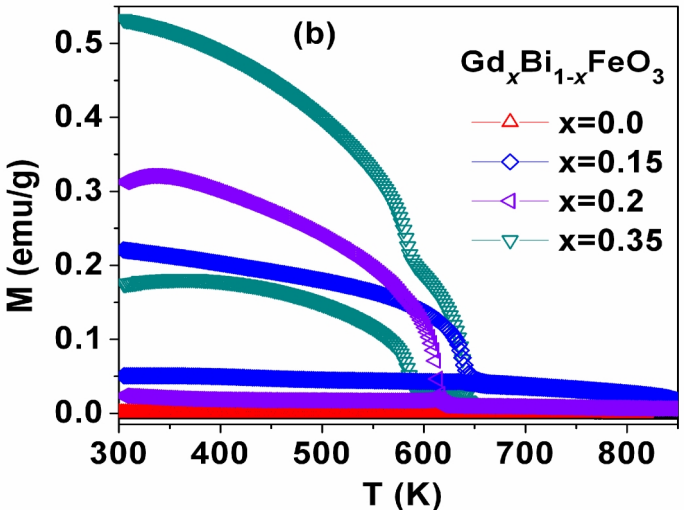

Figure 4.27 Magnetization in the temperature region 300 K to 850 K for $Gd_xBi_{1-x}FeO_3$ (x = 0, 0.15, 0.2, and 0.35) samples at an applied field of H = 500 Oe.

The previous reports [33] of FC and ZFC measurements at below 300 K do not show any irreversibility (which is also true in the present

study) as the ZFC magnetization in these measurements are carried out by cooling the sample only from 300 K and do not reflect the true ZFC measurements as the T_N is much above the room temperature. In order to investigate the irreversibility in these systems, the ZFC measurements need to be carried out by cooling the sample in zero fields from above T_N. So as to investigate the true nature of irreversibility M-T measurements are carried out in ZFC-FC mode by cooling the sample from above T_N. Unlike the M-T curve in the low temperature region, the M-T curve measured from 300 K - 850 K (figure 4.27) shows a strong irreversibility in these samples. The magnitude of irreversibility (which is estimated as $M_{FC} - M_{ZFC}$) increases with an increase in x. The onset of irreversibility temperature (T_{irr}) initially rises with an increase in x and T_{irr} decreases for $x = 0.35$ for which a reduction in magnetization is also observed. The plot between $1/\chi$ vs. T for $T > T_N$ (figure 4.28) is non-linear indicating the presence of short range magnetic correlations even for temperatures much beyond T_N.

The T_N of BFO with Gd content shows an opposite trend compared to La doped samples (table 4.4). Table 4.6 shows the T_N dependence on Gd content, from the figure; the T_N reduces with increase in Gd content.

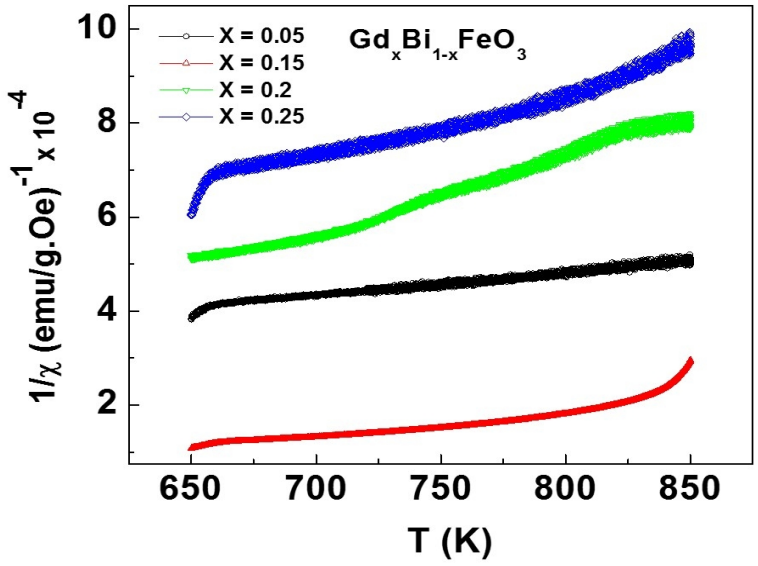

Figure 4.28 $1/\chi$ vs. T plot for GBFO samples in the region $T > T_N$.

Table 4.6, Variation of T_N with Gd content.

Composition	T_N (K)
$x = 0$	651.0
$x = 0.05$	640.9
$x = 0.15$	635.9
$x = 0.2$	612.7
$x = 0.25$	632.4

Conclusions

Gd doping in BFO results into a series of structural phase transitions with Gd content. The both dielectric constant and loss increases with Gd. An indirect evidence of linear magneto-electric effect is observed in temperature dependent dielectric constant. Magnetic properties are very much improved with Gd element. The minimum in magnetization seen for x = 0.1 and 0.2 samples can be understood in terms of a two sublattice model which will be discussed at the end of next section.

Effect of Ho doping on the multiferroic properties of $BiFeO_3$

4(c)

4.7. Introduction

The doping of Ho, which has the highest magnetic moment of 10.6 μ_B among all the rare earths is interesting as it results in a huge structural distortion due to the large ionic radii mismatch at Bi-site and induces additional magnetic interactions that can enhance the magnetic properties. In the present study, we report the systematic structural, Raman, dielectric and magnetic properties in low and high temperatures of $Bi_{1-x}Ho_xFeO_3$ (x = 0, 0.05, 0.1, 0.15 and 0.2) ceramics prepared by solid-state reaction method.

4.8. Experimental Details

$Bi_{1-x}Ho_xFeO_3$ (x = 0, 0.05, 0.1, 0.15 and 0.2) powders were synthesized using conventional solid-state reaction method taking the stoichiometric amounts of Ho_2O_3, Bi_2O_3 and Fe_2O_3. The samples thus obtained are used for further characterization.

4.9. Results and discussion

4.9.1. X-Ray Diffraction (XRD)Analysis

The XRD pattern of $Ho_xBi_{1-x}FeO_3$ (x = 0, 0.1, 0.15 and 0.2) ceramics carried out using Co K_α = 1.7887 Å is shown in figure 4.29. The introduction of Holmium (Ho) in BFO found to suppress the formation of the secondary phases. The XRD patterns clearly show the absence of impurity phase as the Ho concentration increases beyond x = 0.1. Compared to pure BFO the peaks in XRD pattern found to shift to higher angle as x increases. The inset of figure 4.29 shows magnified XRD pattern around 37° show the split reflections (1 0 4) and (1 1 0) try to merge into a single broad peak with a shift towards higher angles. The shift in the diffraction peak positions towards higher angles confirms substitution effects and indicates a structural change due to the lattice distortion caused by the Ho doping. The new peaks are noticed in the diffraction pattern for x = 0.2 around 37°. This peak corresponding to $HoFeO_3$, that means the rhombohedral phase of BFO is transforming to orthorhombic phase. To confirm this, we have performed Rietveld refinement on all the samples. The calculated lattice parameters for pure BFO is a = 5.62 Å and c =13.69 Å. These are reduced to a = 5.55 Å and c = 13.58 Å for x = 0.15 as the ionic radius of Bi^{3+} (1.14 Å) is greater than Ho^{3+} (1.015 Å). The detailed refinement results are tabulated in table 4.7.

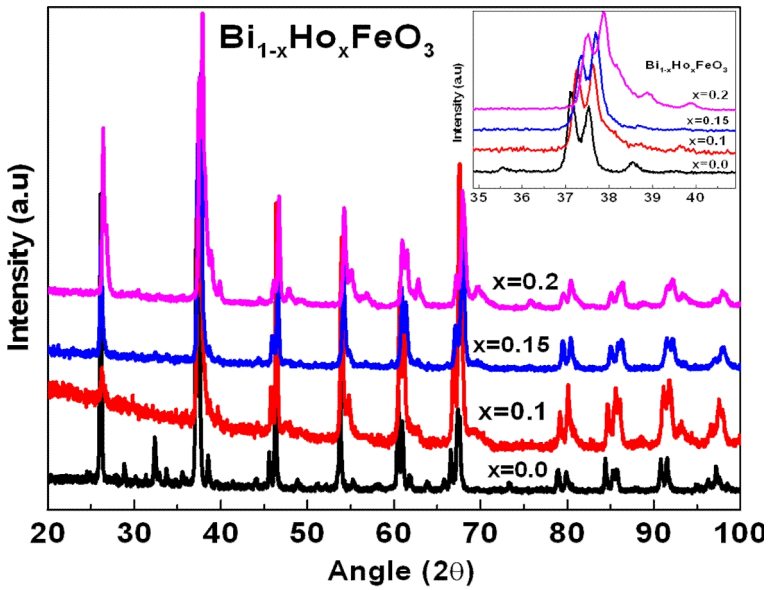

Figure 4.29 X-ray diffraction pattern of $Ho_xBi_{1-x}FeO_3$ (x = 0, 0.05, 0.15 and 0.2). Inset shows the diffraction peaks at 37°.

Table 4.7. Refined Structural Parameters for $Ho_xBi_{1-x}FeO_3$ samples.

	$x = 0$	$x = 0.05$	$x = 0.1$	$x = 0.15$	$x = 0.2$
Structure	*R3c*	*R3c*	*R3c*	*R3c*	*Pnma*
***a* (Å)**	5.620	5.600	5.582	5.554	5.615
***b* (Å)**	5.620	5.600	5.582	5.554	7.840
***c* (Å)**	13.692	13.620	13.612	13.586	5.461
***V* (Å³)**	374.62	369.89	367.34	363.02	240.40
Fe-O_2 (Å)	2.20	2.198	2.185	2.181	2.172
Fe-O_2-Fe (°)	153.4	153.31	153.03	152.82	152.4
R_{wp} %	2.95	3.36	5.34	9.02	8.23
R_p %	2.02	2.14	3.35	6.85	6.54

4.9.2. Microstructural properties

The microstructure of Ho doped samples is shown in figure 4.30. Similar to La and Gd doped samples all the Ho doped samples are dense and granular. For x = 0.05, the sample has a larger grain growth having an average grain size of 1.6 μm. This grain size reduces slightly for x = 0.1(0.8 μm). However, addition of 15% Ho in BFO results in the aggregation of these clusters and grain size increases to 1.5 μm with an irregular shape. For x = 0.2 grain growth again decreases (0.7 μm). The Ho doping up to certain concentration prevent the grain growth and on the further increase in x, grains start growing and helps in densification.

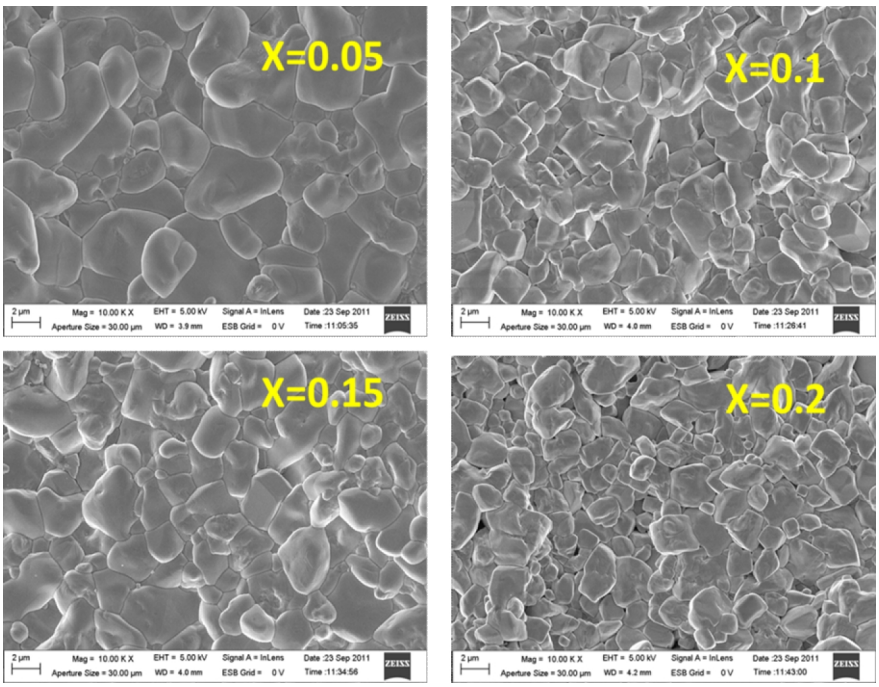

Figure 4.30 FE- SEM images of $Ho_xBi_{1-x}FeO_3$ (x = 0.05, 0.1, 0.15 and 0.2) samples.

Thus, FE-SEM observations show that morphology changes with the doping, but the size of the grains is greater than the spin cycloid wave length of BFO, 62 nm.

The Energy Dispersive Spectra (EDS), performed on the pure and doped samples, shows the major signal corresponding to O, Bi and Fe and a weak signal of Ho for doped samples. This confirms that all the samples are pure, and no secondary magnetic impurity is detected (See table in the figure 4.31).

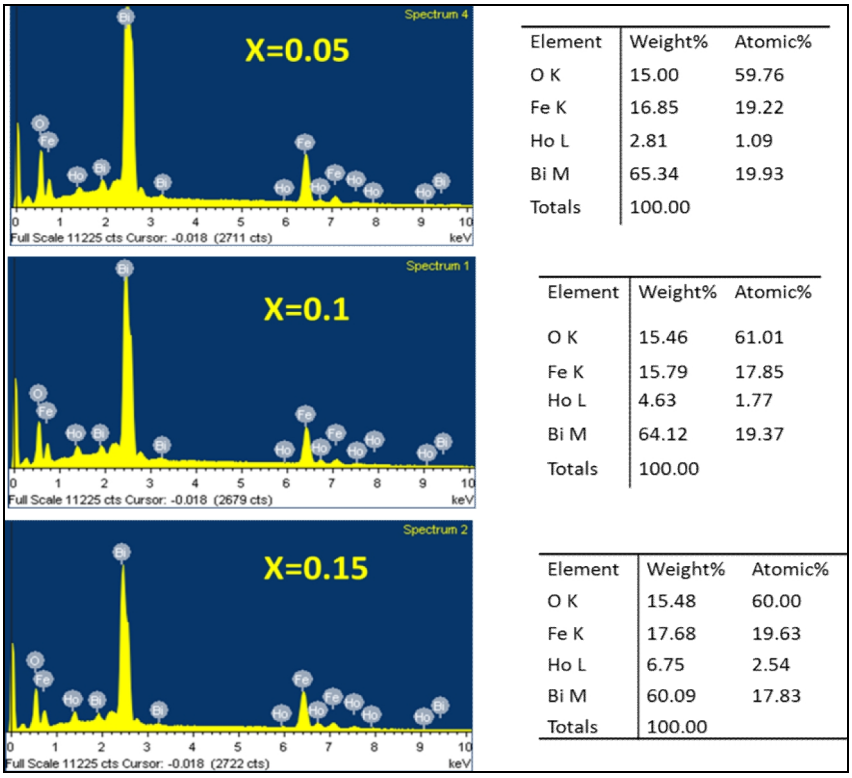

Element	Weight%	Atomic%
O K	15.00	59.76
Fe K	16.85	19.22
Ho L	2.81	1.09
Bi M	65.34	19.93
Totals	100.00	

Element	Weight%	Atomic%
O K	15.46	61.01
Fe K	15.79	17.85
Ho L	4.63	1.77
Bi M	64.12	19.37
Totals	100.00	

Element	Weight%	Atomic%
O K	15.48	60.00
Fe K	17.68	19.63
Ho L	6.75	2.54
Bi M	60.09	17.83
Totals	100.00	

Figure 4.31 The EDS for $Ho_xBi_{1-x}FeO_3$ (x = 0.05, 0.1, and 0.15) samples.

4.9.3. Raman spectroscopic studies

The room temperature (RT) Raman scattering spectra on the samples under present study are shown in the figure 4.32. It clearly shows a systematic structural transition in accordance with the results of XRD. The modes which are observed for pure BFO exist even for Ho doped samples with a slight shift toward higher frequencies. The modes gradually decrease with increase in Ho content. However, the intensity of the low-frequency modes corresponding to the pure BFO sample reduces, and new peaks at 329 cm^{-1} and 475 cm^{-1} emerges as x increases. These peaks are also observed for other dopant systems [25]. The new peaks may result from $HoFeO_3$ orthorhombic phase.

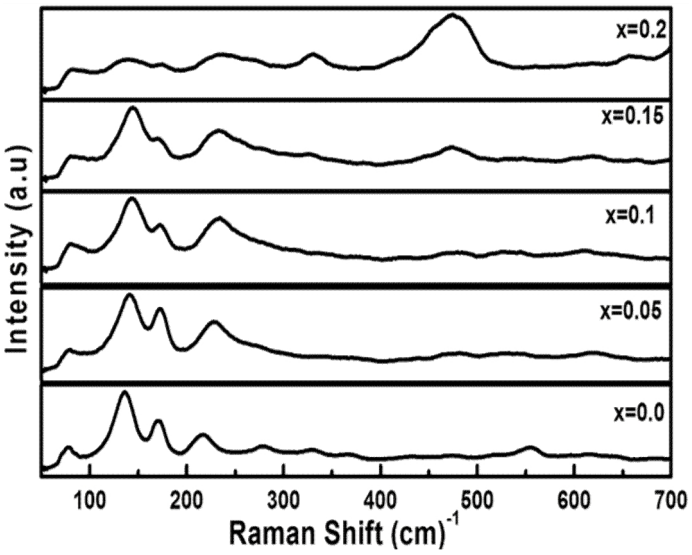

Figure 4.32 Raman spectra of $Ho_xBi_{1-x}FeO_3$ (x = 0, 0.05, 0.15, 0.1 and 0.2) samples.

The low-frequency modes are related to Bi atoms of perovskite layer. The modes located at high frequencies are caused by internal vibration of FeO_6 octahedra. The changes in Raman modes can be attributed to the change in the occupation of bismuth at different sites by holmium within the perovskite units and the change in the Bi-O covalent bonds due to the Ho doping. Hence the structural phase transition modifies the Raman modes.

4.9.4. Dielectric Properties

The dielectric constant (ε_r) of $Bi_{1-x}Ho_xFeO_3$ samples in the frequency range of 20 Hz – 2 MHz is measured at room temperature to investigate the variation of ε_r with Ho doping. The plot of dielectric constant versus frequency is shown in figure 4.33. The dielectric constant decreses with an increase in frequency and follows Debye law of frequency dispersion as it is nearly constant at very high frequencies [12]. ε_r of the undoped BFO is 68 at 1 KHz and it is decreased to 40 at 2 MHz. The ε_r values for $Bi_{1-x}Ho_xFeO_3$ are found to be 67, 88, and 49 for the compositions x = 0.05, 0.1, and 0.15 respectively at the frequency of 1 KHz. The enhancement in dielectric constant can be understood in terms of the ferroelectric off-centering distortion brought by the difference in the atomic radii of Ho and Bi. This leads to the change in the Fe-O bond length in the FeO_6 octahedron cage which in turn is responsible for the

increase in polarization and hence the dielectric constant [11]. On further increase in Ho content to x = 0.15, ε_r decreases but it possesses a maximum values of dielectric constant for x = 0.2, where a structural transition is observed.

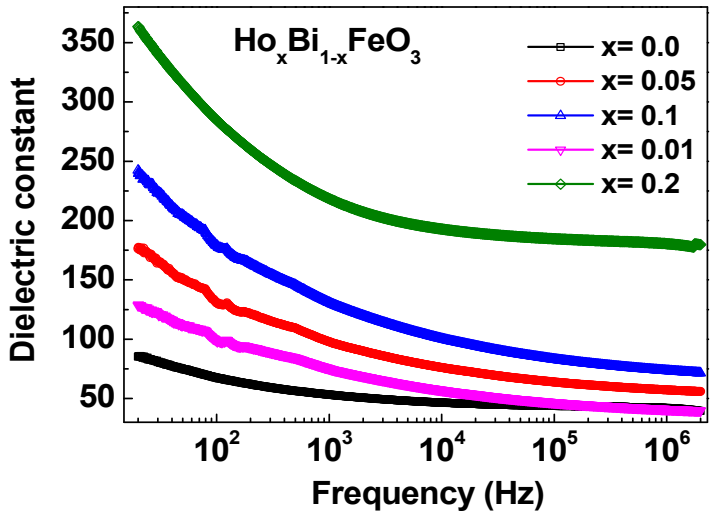

Figure 4.33 Dielectric constant (ε_r) versus frequency $Ho_xBi_{1-x}FeO_3$ (x = 0 – 0.2) samples at 300 K.

The variation of dielectric constant as a function of temperature at different frequencies for x = 0.05 sample is plotted in figure 4.34. Dielectric constant increases as the temperature increases and exhibit higher values for lower frequencies. At higher frequencies, electric dipoles have shorter time to follow the applied field and hence dielectric constant decreases. A clear transition is observed around 377 °C, which is more prominent for low frequencies. This corresponds to an

antiferromagnetic transition of Ho doped BFO and the T_N is found to increase slightly compared to the BFO.

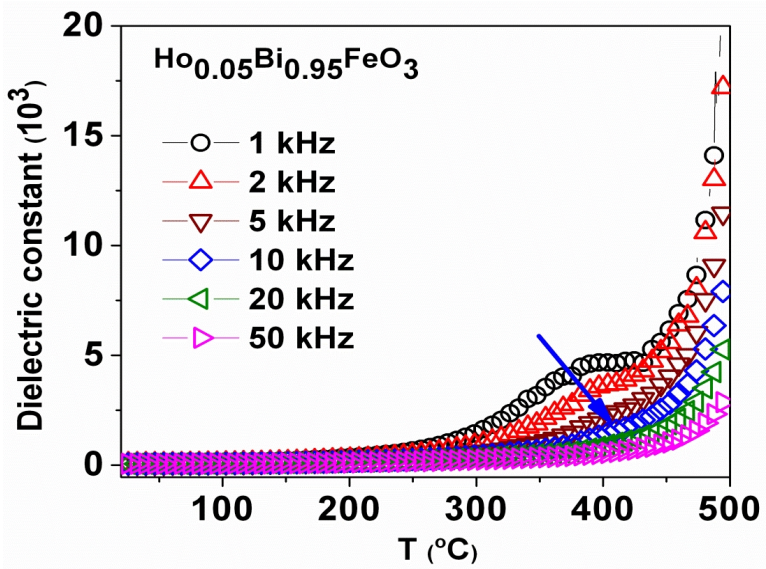

Figure 4.34 Dielectric constant (ε_r) verses temperature $Ho_xBi_{1-x}FeO_3$ (x = 0.05) samples at different frequencies.

4.9.5. Ferroelectric measurements

Polarization hysteresis loops on the HBFO samples measured at a maximum applied field of 40 kV/cm are shown in the figure 4.35. The remnant polarization (P_r) as well as saturation polarization (P_S) values are found to increase with Ho substitution. This increase in polarization values is due to the crystal distortion caused by the doping of the dissimilar ions, which decreases the Fe-O bond length and favours the growth of polarization vector. Polarization parameters for HBFO samples are tabulated in table 4.8. As the Ho content increases, similar to

the observed trend in dielectric measurements, polarization values increases with x except for 0.15. For x= 0.2, P_r exhibits a maximum value of 2.16 μC/cm².

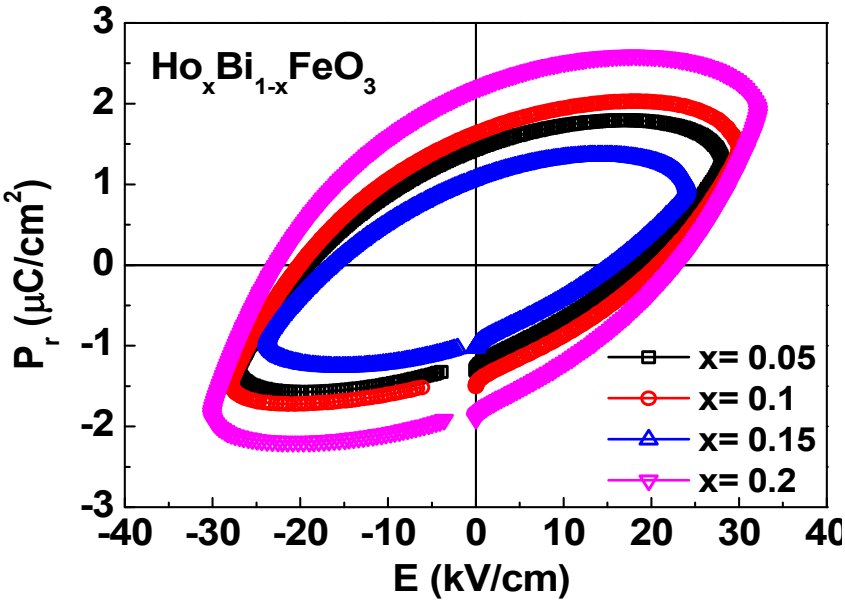

Figure 4.35 Polarization verses Electric field loops for HBFO samples at RT.

Table 4.8 Polarization parameters for HBFO samples.

Ho content	P_r (μC/cm²)	E_C (kV/cm)
x = 0.0	1	39
x = 0.05	1.44	18.5
x = 0.1	1.62	19.8
x = 0.15	1.06	15.5
x = 0.2	2.16	23

4.9.6. ac conductivity measurements

Conductivity measured at different frequencies and temperatures σ_{ac} (f, T) is used to investigate the conduction mechanism in many different systems. Ac conductivity is calculated using the expression,

$$\sigma' = Y'(t/A) = [\frac{Z'}{(Z'^2 + Z''^2)}](t/A) \qquad (4.1)$$

where Z' and Z'' are the real and imaginary parts of impedance, Y' the real part of the admittance, 't' the thickness (m) and A the area (m^2) of the sample, respectively. Temperature was stabilized (± 0.5 °C) at 10°C intervals, while sweeping Z* as a function of frequency.

A typical plot of the ac conductivity (σ') derived from Eq. (4.1) is shown in figure 4.36 as a function of f at temperatures 35 ≤ T ≤ 450 °C measured in the frequency range of 100 Hz- 1 MHz. The ac conductivity, σ' (f, T), is generally described using Jonscher's power laws, which were found to be universal in many materials such as disordered solids and ionic conducting glasses.

$$\sigma'(f) = \sigma_{dc}[1 + (\frac{\omega}{\omega_p})^n] \qquad (4.2)$$

where σ_{dc} is the dc conductivity, ω and ω_p are the applied frequency and the relaxation frequency in radians, respectively, and n is an exponent.

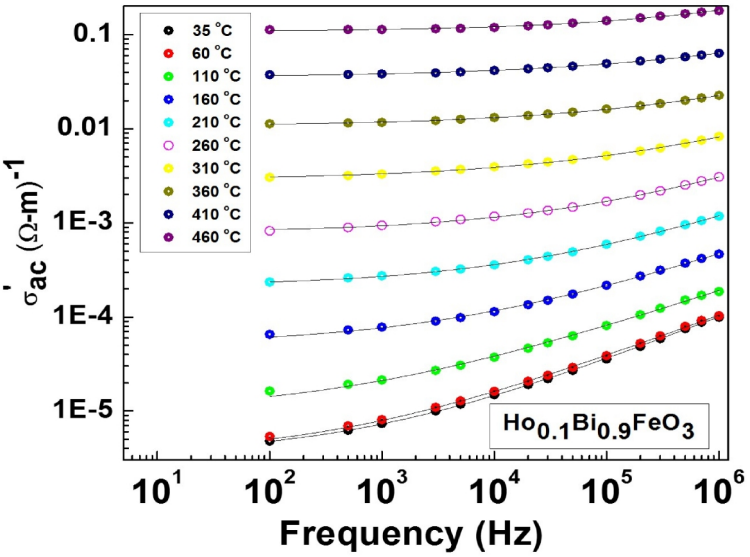

Figure 4.36 Ac conductivity as a function of frequency at different temperature for Ho doped BFO, Lines are fits based on Eq. (4.2).

A long-range hopping of mobile charges will occur at high temperatures and low frequencies, resulting in a Jonscher-type hopping conduction. Depending on the variation of the conductivity with frequency in general two regimes are found in the literature, for frequencies $f < f_p$, the ion hopping termed as "diffusive", leading to a frequency-independent conductivity σ_{dc}. For $f > f_p$, the frequency dependent dispersion in the conductivity is observed due to the inhomogeneous potential distribution. For RE doped BFO in the entire measured temperature range of RT to 450 °C the conductivity increases with T and also with increase in frequency. The frequency dependency is described by Eq. (4.2) and the fits based on this equation are shown in

figure 4.36, with n value lying between 0.4 and 0.6 for the measured temperature range depending on the system and concentration of RE doping. The value of the conductivity exponent depends on the type of conduction mechanism. In this study it is found that n lies between $0 < n < 1$ indicating that the conduction to be of translational hopping motion.

4.9.7 Magnetic Properties

The detailed M-H measurements of $Ho_xBi_{1-x}FeO_3$ (0.05 - 0.2) are carried out at various temperatures up to a field of 9 T in order to investigate the effect of Ho doping on the magnetic properties. Figure 4.37 (a) shows the M-H loop for x = 0.05 measured in the temperature range of 2 K - 300 K. As expected, remarkable increase in M is observed at RT for this sample compared to x = 0. With decrease in temperature, the magnetization at 9 T field increases systematically from its value of 1.39 emu/g at RT to 5.62 emu/g at 2 K. It can be also seen from the figure that there is a gradual increase in curvature of M-H loops with decrease in temperature, tending towards saturation. However, even the M-H at 2 K is far from saturation for fields up to 9 T. In order to estimate the magnetic parameters such as H_C, M_r and also observe the nature of M-H loop clearly, the M-H loops measured at 2 K and 300 K are plotted in figure 4.37 (b and c). The inset shows the enlarged picture indicating the finite coercivity observed at these temperatures. It can be noticed

immediately that there is huge increase in Hc with increase in Temperature (which is counter intuitive). But this behavior is also seen in few other samples studied in this work such as the parent BFO, La doped BFO for x = 0.4 and Gd doped BFO and also La, Gd co-doped samples (will be discussed in chapter 5).

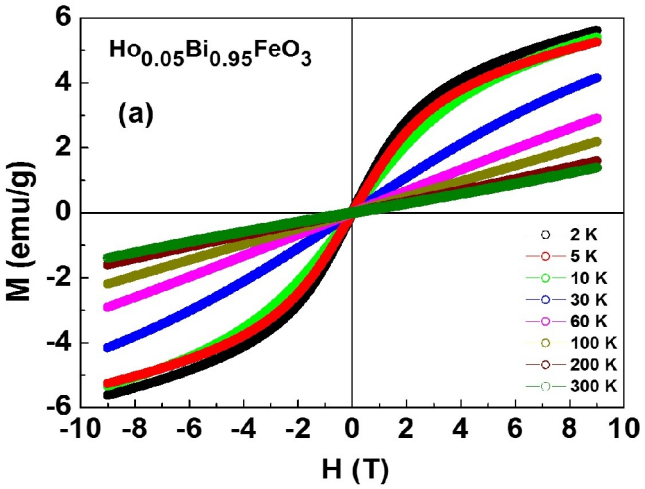

Figure 4.37 (a) M-H loops of HBFO (x = 0.05) at different temperatures.

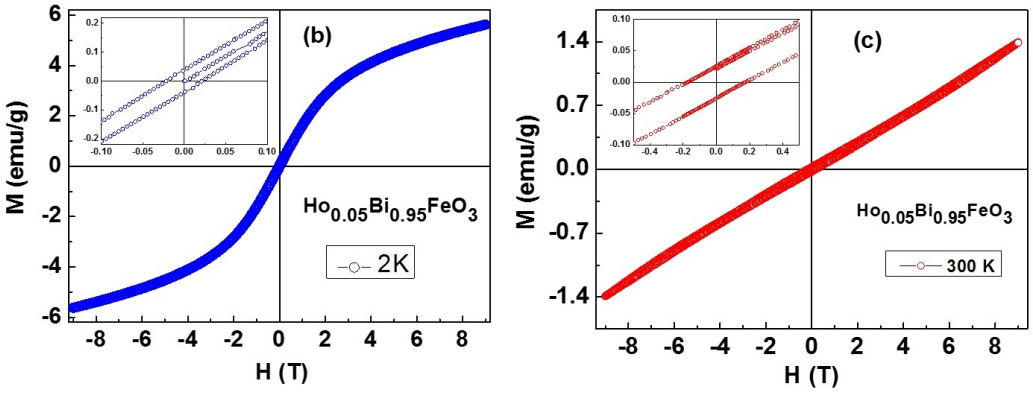

Figure 4.37 (b, c) M-H loops of HBFO (x = 0.05) at (b) 2 K and (c) 300 K.

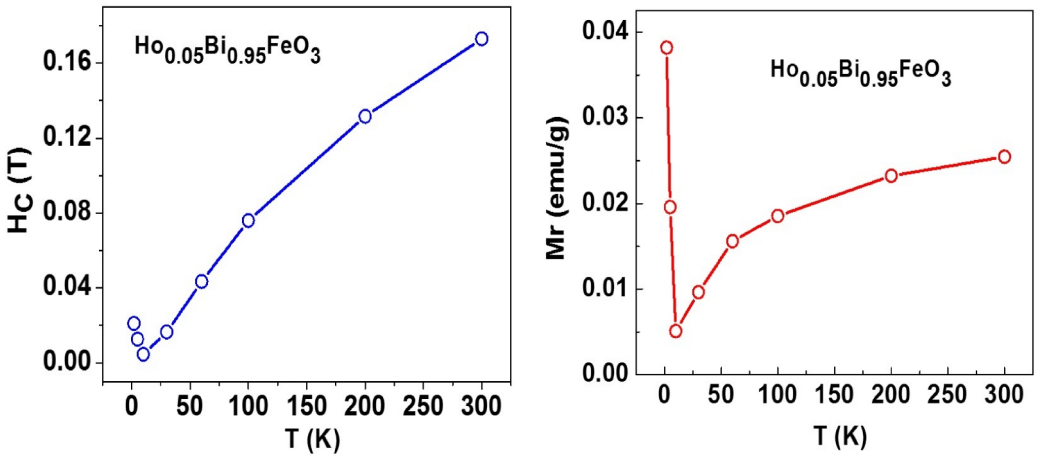

Figure 4.38 Variation of H_C and M_r with temperature for HBFO (x = 0.05).

The variation of H_C and M_r are plotted in figure 4.38. At 2 K, H_C has a value of 210 Oe and there is decrease with increase in T up to 10 K and reaches a value of 46 Oe as expected for normal ferromagnetic materials whereas with further increase in T, Hc increases almost linearly and reaches a value of 1720 Oe at 300 K. Even though the increase in H_C is seen for undoped BFO and La doped BFO for x = 0.4, the variation of H_C in these samples is very small. But both in Gd doped samples and also for this Ho doped sample with x = 0.05, there is a huge increase in H_C. The increase in H_C with T is not completely understood at present. The temperature variation of M_r is similar to that of H_C where in M_r decreases initially from 2 K to 10 K and with further increase in T, M_r increases.

The M-H loops for x = 0.1 are shown in figure 4. 39 (a) in the entire measured temperature range of 2 K – 300 K. With increase in Ho content the magnetization increases and has a value of 2.37 emu/g at RT. There is a systematic increase in M with decrease in T and reaches a maximum value of 10.91 emu/g at 2 K. The selected M-H loops at 2, 60 and 300 K are shown in figure 4.39 (b, c, d). The shape of M-H changes quite remarkably with change in temperature. At 2 K, M-H shows the ferromagnetic loop with a H_C of 2020 Oe and with increase in T, the shape turns towards antiferromagnetic loop with a narrow waist thereby decreasing the H_C. The inset shows the enlarged view of the hysteresis close to H = 0. The temperature dependence of the H_C and M_r are shown in figure 4.40. H_C decreases initially with decrease in T up to 30 K and shows a peak at 60 K (H_C ~ 620 Oe) beyond which decreases with increase in temperature and reaches a value of 358 Oe at RT. The temperature dependence of M-H loop shape and H_C can be understood in terms of a model which will be discussed later. M_r decreases sharply up to 30 K and beyond which there is a small decrease with increase in temperature.

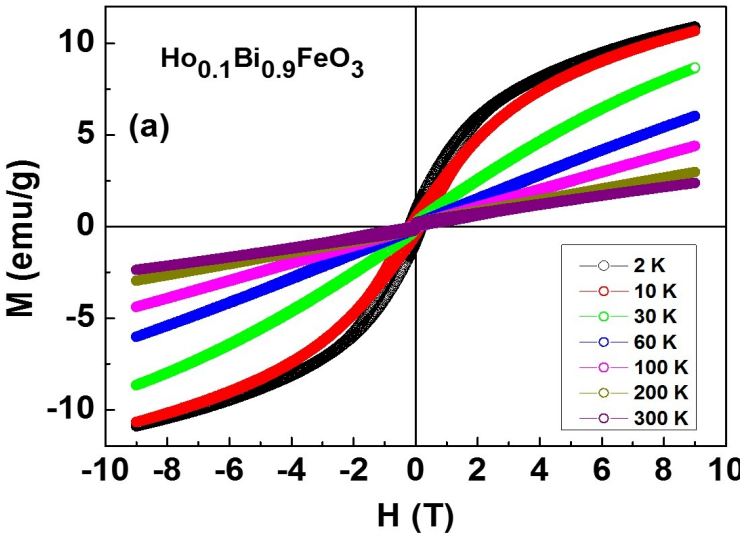

Figure 4.39 (a) M-H loops of HBFO (x = 0.1) at different temperatures.

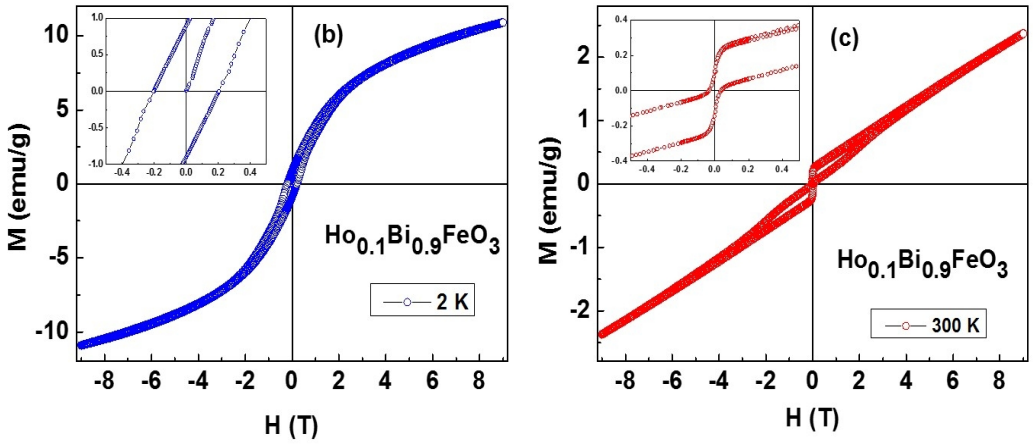

Figure 4.39 (b, c) M-H loops of HBFO (x = 0.1) at (b) 2 K and (c) 300 K.

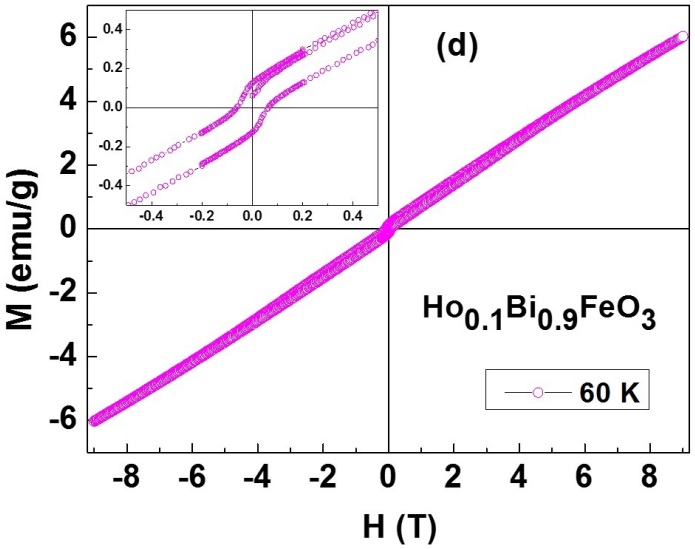

Figure 4.39 (d) M-H loops of HBFO (x = 0.1) at 60 K.

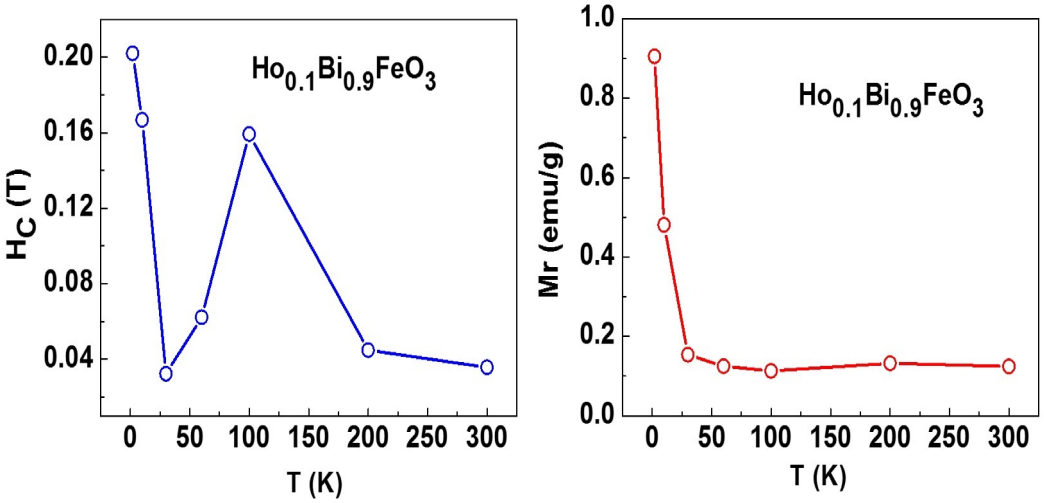

Figure 4.40 Variation of H_C and M_r with temperature for HBFO (x = 0.1).

The M-H loops measured at various temperatures in range of 2 K - 300 K for x = 0.15 are shown in figure 4. 41 (a). Similar to x = 0.1, even in the case of x = 0.15, the magnetization increases with increase in Ho content and has a value of 3.81 emu/g at RT for 9 T field. With decrease in T, the magnetization increases systematically and reaches a value of 14.4 emu/g at 2 K. The curvature of M-H is more pronounced in comparison to x = 0.05 and 0.1 indicating the increase in the ferromagnetic component. The M-H at 2 K still has a large high field susceptibility indicating that the magnetization is far from saturation even at a field of 9 T. The magnified M-H loops at a few selected temperatures (2 K, 80 K and 300 K) are shown in figure 4.41 (b, c, d). Similar to x = 0.1, in this case also the shape of the loops changes dramatically with increase in T. At low temperatures the M-H exhibit the ferromagnetic behavior but with increase in T, the curves exhibit the so called double hysteresis loops with a pinching close to H = 0. The variation of H_C and M_r with T are plotted in figure 4. 41. H_C has a maximum value of 1380 Oe at 2 K and with increase in T, H_C decreases and reaches ~ 400 Oe at 20 K (we do not have M-H at 30 K in this case) but with further increase in T, H_C starts increasing and has a peak at 80 K with a value of ~ 1360 Oe which is close to the H_C at 2 K. The H_C decreases with further increase in T and reaches a value of 63 Oe at RT. The decrease in H_C above 80 K reflects the pronounced pinching

observed above this temperature. The variation of M_r with T is shown in figure 4.42. M_r decreases sharply from 2.4 emu/g at 2 K to 0.22 emu/g at 80 K and with further increase in T a slight increase is observed at 150 K and finally decreases to a RT value of 0.24 emu/g. At 80 K, the H_C has a peak whereas M_r has a minimum value. M-T measurements at low fields also show corresponding changes at this temperature, which can be explained by a model which is discussed at the end of this section.

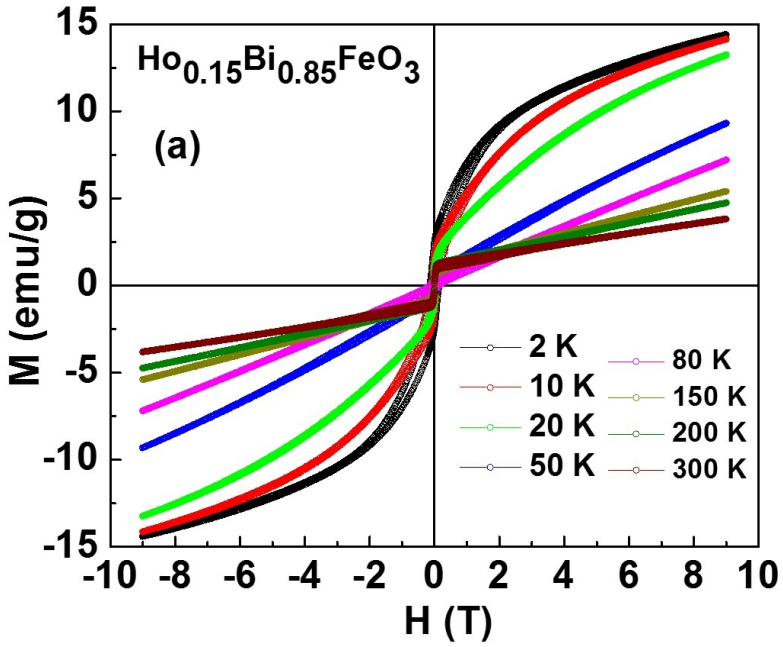

Figure 4.41 (a) M-H loops of HBFO (x = 0.15) at different temperatures.

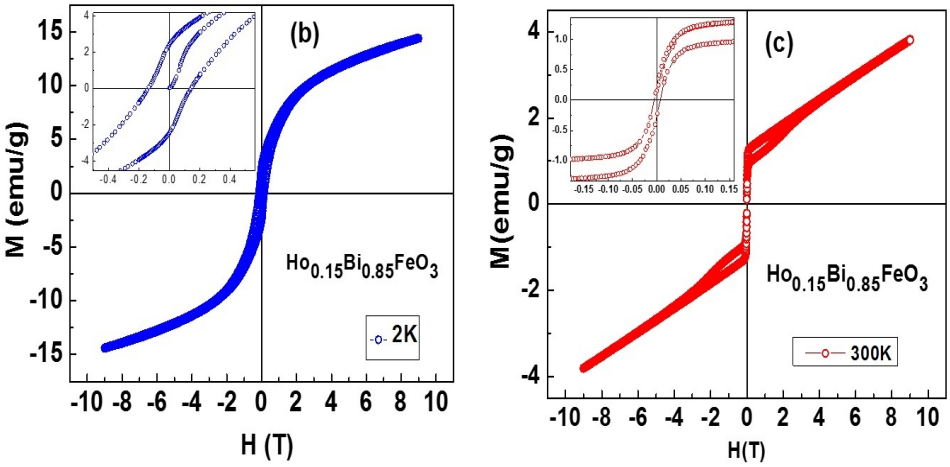

Figure 4.41(b, c) M-H loops of HBFO (x = 0.15) at (b) 2 K and (c) 300 K.

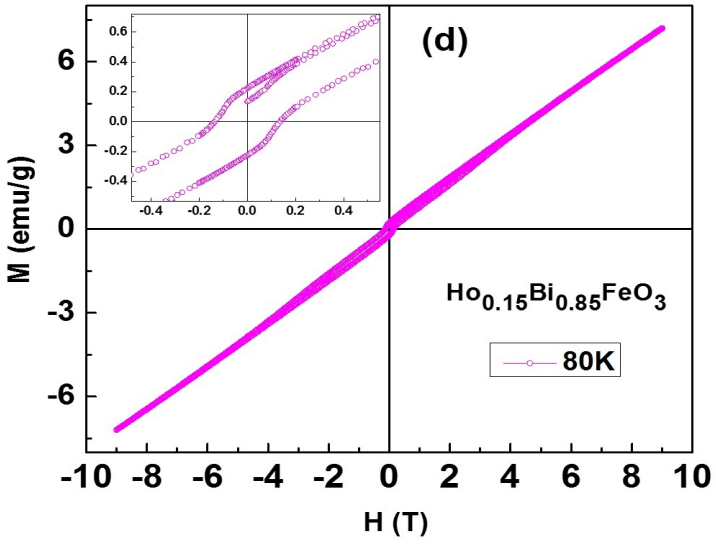

Figure 4.41 (d) M-H loops of HBFO (x = 0.15) at 80 K.

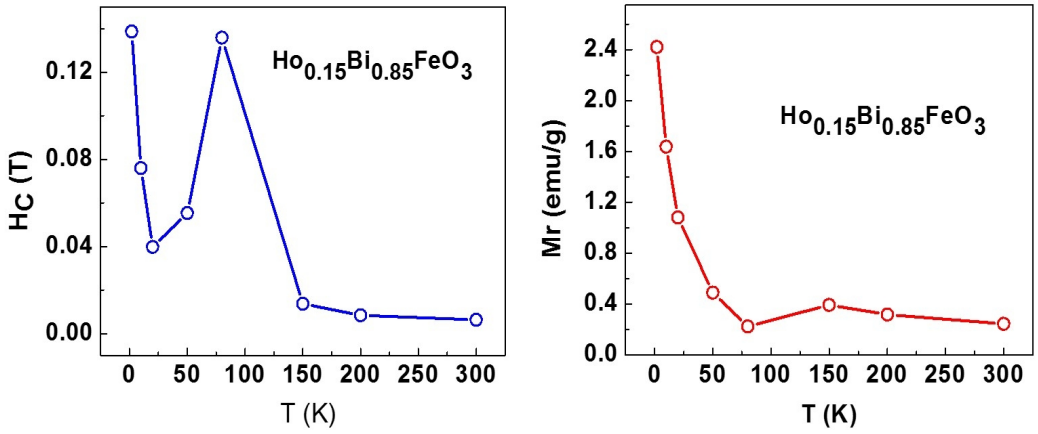

Figure 4.42 Variation of H_C and M_r with temperature for HBFO (x = 0.15).

Finally, the M-H behavior for x = 0.2 where a structural transition from *R3C* to *Pnma* occurs is discussed. The M-H loop measured at different temperatures is shown in figure 4.43 (a, b, c and d). As the Ho concentration increases, the value of M (9T) at 300 K increases to 5.67 emu/g and with decrease in T, high field magnetization, M_{9T} increases systematically and reaches a value of 17.9 emu/g at 2 K. The increase in M as well as increase in curvature of M-H indicates the increase in ferromagnetic component with increase in Ho content. But, even for x = 0.2, the M-H loops do not saturate even for 9 T field. Similar to the other two compositions of x = 0.1 and 0.15, in this case also M-H loop changes quite a bit with increase in temperature. The M-H loops exhibit a beautiful ferromagnetic loop at 2 K but at high temperatures, the loop exhibits pinching close to H = 0, giving rise to double hysteresis loop. The variation of H_C and M_r are plotted in figure 4.44. Both H_C and M_r

behave exactly similar to those observed for x = 0.15. In this case, Hc has a maximum value ~ 1558 Oe at 2 K and decreases to 331 Oe at 2 K, with a peak value of 1208 Oe at 80 K and finally decreasing to 463 Oe at RT.

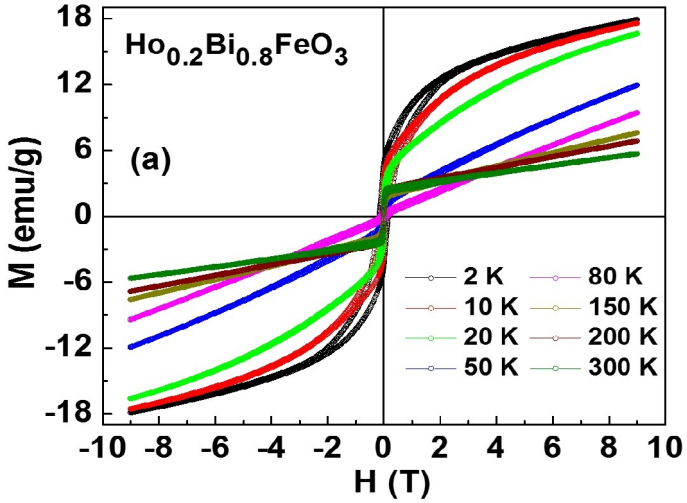

Figure 4.43 (a) M-H loops of HBFO (x = 0.2) at different temperatures.

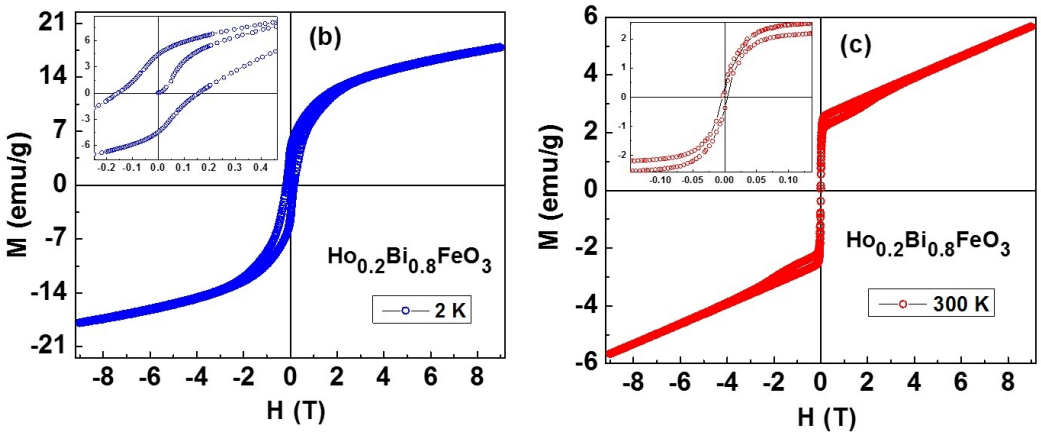

Figure 4.43 M-H loops of HBFO (x = 0.2) at (b) 2 K and (c) 300 K.

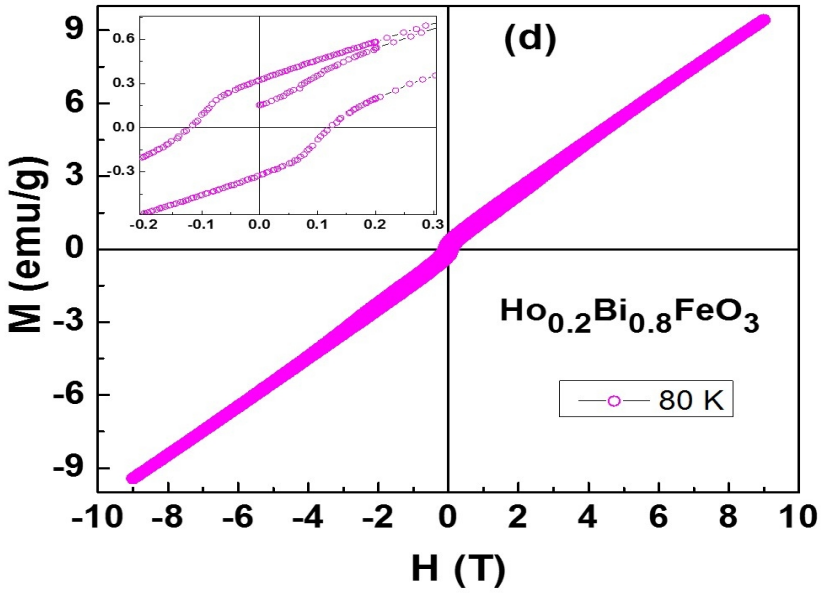

Figure 4.43 (d) M-H loops of HBFO (x = 0.2) at 80 K.

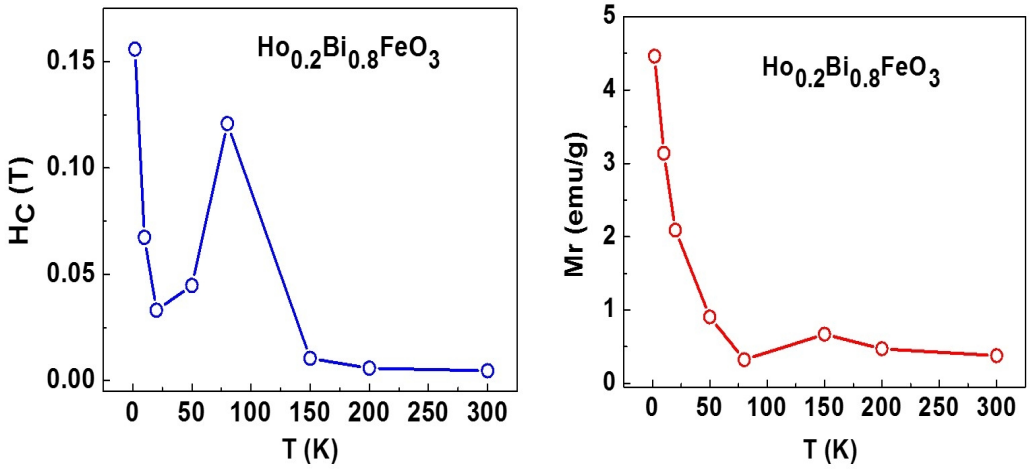

Figure 4.44 Variation of H_c and M_r with temperature for HBFO (x = 0.2).

The variation of Magnetization at 9T as a function of Temperature is plotted in figure 4.45 for all the Ho concentrations ($0.05 \leq x \leq 0.2$) which shows an increase in M with Ho concentration.

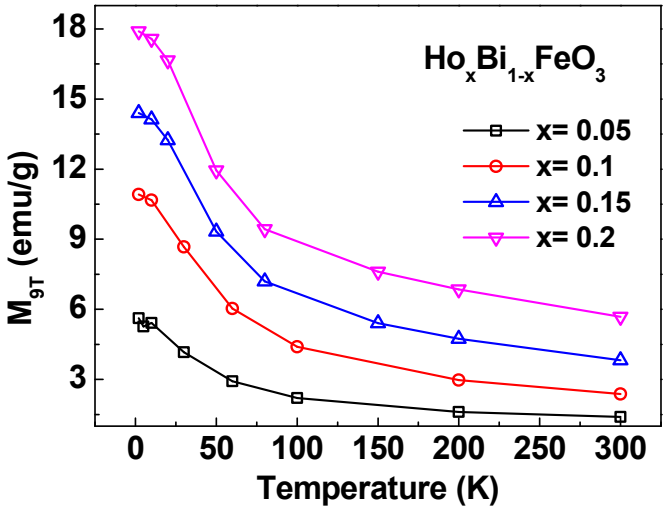

Figure 4.45 Temperature dependence of Magnetization measured at 9 T for HBFO.

4.9.7.1. Low temperature M-T studies

Magnetization as a function of temperature in both zero field cooled (ZFC) and field cooled (FC) modes are measured for all the samples at H = 500 Oe and 1 kOe. Figure 4. 46 (a) shows the M-T for x = 0.05. The Magnetization increases continuously with decrease in T for both the fields and also ZFC and FC curves overlap throughout the temperature range. Figure 4.46 (b) shows $1/\chi$ versus T and shows a nonlinear behavior in the entire temperature range. The M-T data for x =

0.1 measured at H = 500 Oe and 1 KOe in ZFC and FC modes is shown in figure 4.47. The magnetization decreases from RT with decrease in temperature up to 95 K (denoted as Θ_C) for 500 Oe field and up to 82 K (Θ_C) for 1 kOe in both ZFC and FC indicating the antiferromagnetic nature of the system. Beyond this temperature both FC and ZFC increases sharply indicating the ferromagnetic nature. ZFC and FC start bifurcating at T = 41 K for H = 500 Oe and the irreversibility increases with decrease in temperature. The M-T for H = 1 kOe, below the minimum in FC and ZFC is quite different in comparison to the 500 Oe field case. The ZFC and FC increases and reaches a peak at 16 K and 13 K respectively before decreasing with further decrease in temperature. This complete M-T behavior can be explained in terms of two sublattice model which will be explained in the next section.

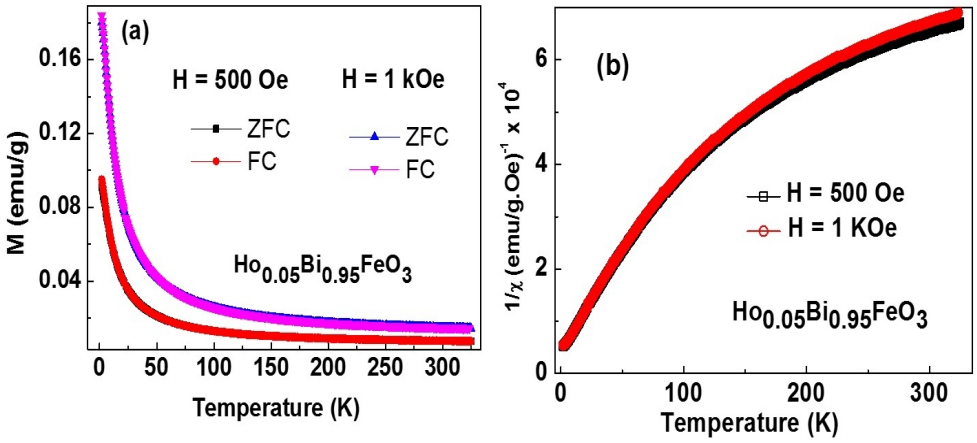

Figure 4.46 (a). M-T curves for HBFO (x = 0.05) sample at different fields and (b). $1/\chi$ versus T

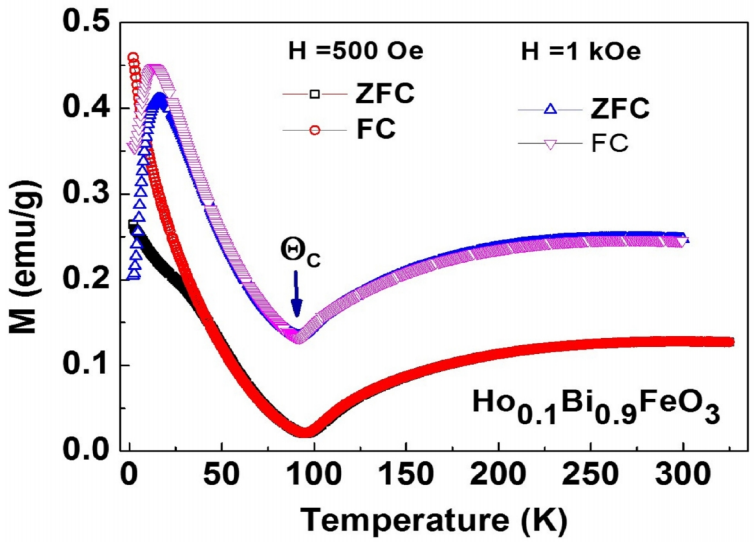

Figure 4.47 M-T curves for HBFO (x = 0.1) sample at different fields.

The overall behavior for M-T for x = 0.15 (figure 4.48) and 0.2 (figure 4.49) are very similar to x = 0.1 but there are certain differences. In both these cases, the magnetization decreases from RT to Θ_C. The value of Θ_C for H = 500 Oe is 82 K and for H = 1 kOe it is 79 K, which is the same for both x = 0.15 and 0.2. It can be noted that Θ_C for both these samples is smaller than that of x = 0.10. As the temperature is decreased further below Θ_C the magnetization increases and shows a bifurcation between ZFC and FC at lower temperatures. Similar to x = 0.1, ZFC shows a peak at 17 K for x = 0.15 and at 15 K for x = 0.2 in the case of H = 500 Oe whereas the FC continues to increase albeit with a change in slope.

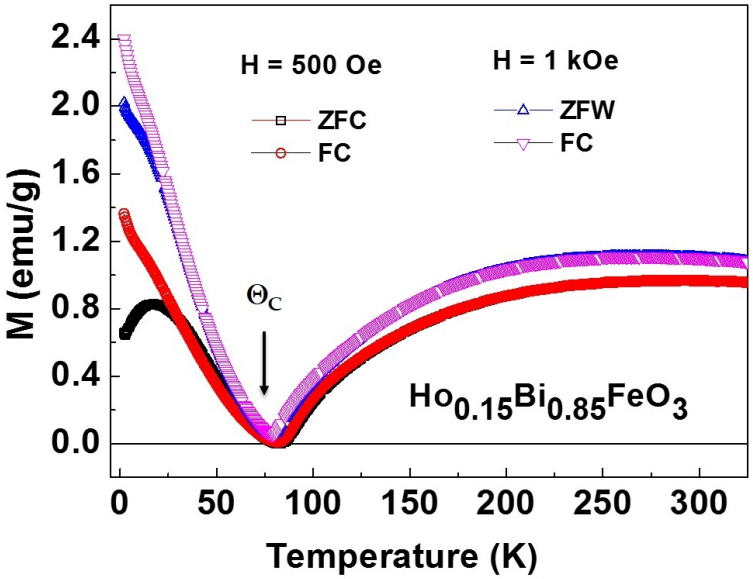

Figure 4.48 M-T curves for HBFO (x = 0.15) sample at different fields.

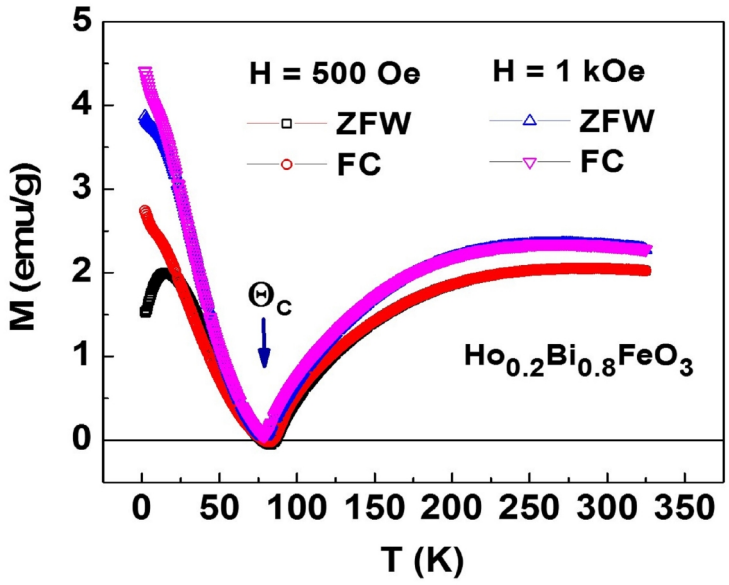

Figure 4.49 M-T curves for HBFO (x = 0.2) sample at different fields.

For H = 1 kOe field both the ZFC and FC increases with decrease in temperature and the irreversibility in magnetization sets in at 30 K for x = 0.15 and it shifts to a lower temperature of 23 K for x = 0.2. The temperature and field dependence of magnetization and the significance and shift of Θ_C with respect to Ho concentration and applied field will be discussed in the next section.

4.9.7.2. ac susceptibility studies

To investigate the dynamics of temperature dependence of magnetization in Ho doped samples, the ac susceptibility measurements are carried out in zero dc field with an ac amplitude of 10 Oe at various frequencies. The representative figure of frequency and temperature dependence of ac susceptibility measurements carried out on x = 0.15 is shown in figure 4.50. The ac susceptibility data mimics the low field dc magnetization data carried out on the same sample where the ac susceptibility decreases with decrease in temperature up to Θ_C ~ 75 K and beyond which there is an increase and reaches a peak close to 30 K. With further decrease in temperature, ac susceptibility decreases with a minimum at 15 K beyond which a sharp rise in susceptibility is seen. Important point to know from this measurement is the fact that there is absolutely no frequency dependence in any of the features observed in magnetization including that of Θ_C.

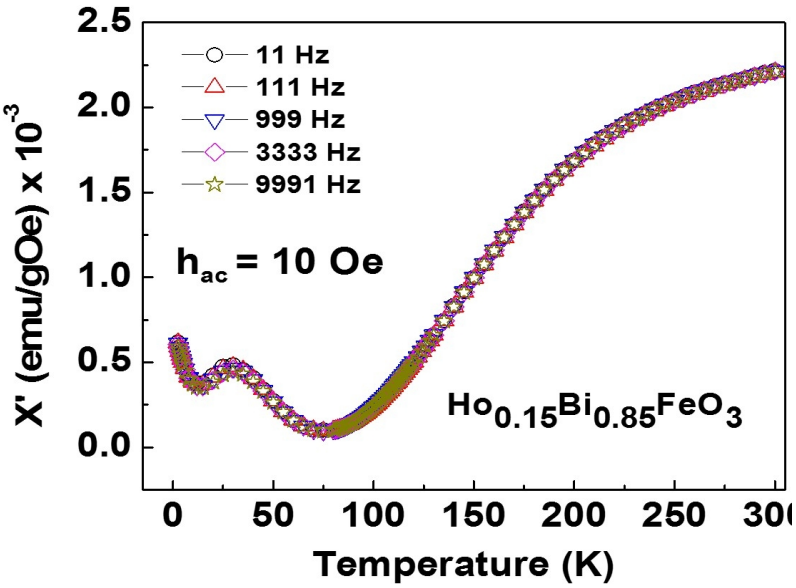

Figure 4.50 ac susceptibility as a function of Temperature at h_{ac} = 10 Oe for HBFO (x = 0.15) sample.

4.9.7.3. High temperature M-T studies

In order to investigate the magnetic transition and also to study the composition dependence on the Nèel temperature (T_N), temperature dependence of magnetization is measured between RT and 850 K using high temperature oven option of the PPMS. All the samples show a magnetic transition from AFM to PM which is shown in figure 4.51 and composition dependence of T_N is given in table 4.9. It can be seen that the T_N decreases with increase in x up to 0.15 and beyond which T_N increases for x = 0.2. This is presumably due to the change in crystal structure from *R3c* to *Pnma*. The inverse susceptibility versus

temperature is non-linear even above the T_N indicating the presence of short range magnetic correlations up to a very high temperature.

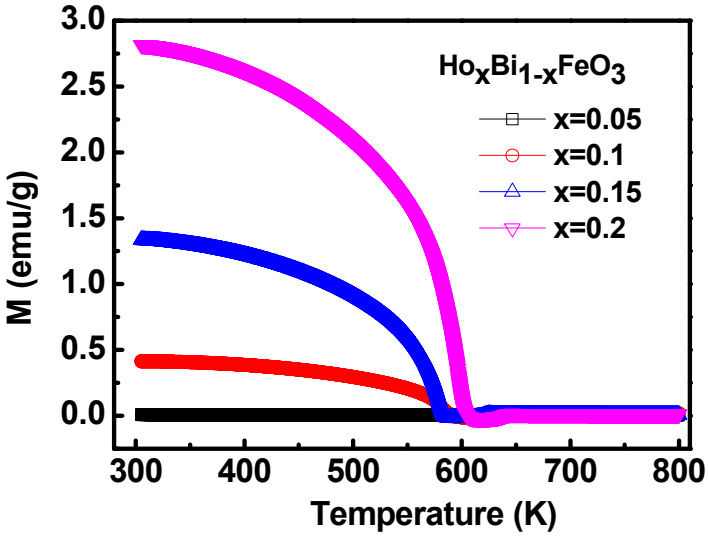

Figure 4.51 Field cooled M-T curves for HBFO samples at 500 Oe.

Table 4.9 Variation of T_N with Ho content.

Composition	T_N (K)
$x = 0$	651
$x = 0.05$	641
$x = 0.1$	605
$x = 0.15$	596
$x = 0.2$	617

4.10. A simple model to explain the temperature, field and concentration dependence of magnetization in Ho doped BFO system.

The magnetization of the rare earth substituted BFO can be understood in terms of two sublattices with an antiferromagnetic coupling between them. The two sublattices primarily consistes of a rare-earth (RE) ferromagnetic sublattice and a canted antiferromagnetic Fe sublattice (which again can be considered as a combination of two FM sublattices). Typically at low temperatures the rare-earth magnetization dominates whereas at high temperatures, the canted antiferromagnetic Fe sublattice magnetization is largest. At some intermediate temperatures the two sublattice magnetizations are equal and opposite resulting in zero net magnetization and the temperature at which it occurs are know in general as a compensation temperature Θ_C. The overall magnetization at any temperature is the vector sum of the individual sublattice magnetizations. The temperature dependence of each subalttice magnetization is very complex and essentially decided by the temperature dependece of effective anisotropy seen by the sublattice.

If we consider the present results, for undoped and low concentration (x = 0.05), the M-H curves and the M-T curves are very

similar and that is decided by mainly the temperature dependece of canted antiferromagnetic sublattice magnetization. With the increase in Ho concentration, due to the effect of RE ferromagnetic sublattice, the complexity increases and the M-H loops at RT and up to almost close to Θ_C show a complicated double hysteresis loops with pinching close to H = 0, where the magnetization is determined by both the canted AFM Fe sublattice and ferromagnetic RE sublattice coupled antiferromagnetically. But below Θ_C, the magnetization is mainly decided by the ferromagnetic Ho sublattice and weakly ferromagnetic Fe subalattice there by increasing the H_C and sharp increase in magnetization. The M-H loops in this temperatue region essentially show the ferromagnetic character of the system.

The temperature dependence of H_C can also be very well explained using the above model. For x = 0.05, H_C increases with increase in T, similar to the undoped sample. The increase in H_C with temperature is seen in 40% La doped sample and also in all the Gd doped samples. So this increase may not be due to the RE sublattice but mostly due to the complicated temperature dependence of the anisotropy. But for x = 0.1, 0.15 and 0.2, H_C decreases initially from RT indicating the AFM nature of the Fe sublattice and close to Θ_C the coercivity tends increases since there is no net magnetization to be acted upon by a magnetic field as $H_C = 2K/M_S$. The decrease in remanent

magnetization close to Θ_C can also be seen from the expanded view of M-H loops and temperature dependence of remanent magnetization. Just below Θ_C, there is an increase in H_C due to the increase in magnetization. As the temperature is decreased further, at low temperatures, the ferromagnetic component of magnetization from the RE sublattics dominates and a weak ferromagnetism is induced in the Fe sublattice. The total magnetization as well as the total anisotropy of the system will increase resulting in an increase in the H_C.

The concentration and field dependence of Θ_C can be explained using this model. The decrease in Θ_C with concentration and also the field is due to the increase in FM component of RE sublattice magnetization.

This two sublattice model can also explain the magnetic properties of Gd doped BFO system, wherein a minimum in magnetization (M-T curve) is seen for x = 0.1 and 0.2. This model can also be extended to explain the magnetic properties of La and Gd co-doping system which is the topic of the next chapter.

4.11. SUMMARY

In summary, we have successfully synthesized $La_xBi_{1-x}FeO_3$ (x = 0.0 - 0.4) ceramics using solid state reaction method. The phase relations of these samples were investigated by XRD. The compositional

dependence of the lattice parameters, unit-cell volumes of the samples were obtained. Rietveld refinement shows a continuous structural evolution of orthorhombic *Pbnm* phase as the La doping increases. The quantitative estimates of the *R3c* and *Pbnm* phases as a function of *x* are reported. Dielectric constant is enhanced with the lanthanum doping. M-T curve shows an anomaly at 50 K, a spin transition temperature of these samples. M-H loops show a huge coercivity which may be due to the high anisotropy in LBFO samples. The enhancement in both dielectric and magnetic properties is attributed due to the structural changes caused by the lanthanum doping. The Néel temperature (T_N) of the BFO increases with La doping.

$Gd_xBi_{1-x}FeO_3$ (x = 0 - 0.35) ceramic samples were successfully synthesized through solid-state reaction method. XRD and Raman measurements reveal a structural phase transition with *x*. The rhombohedral phase with *R3c* symmetry of BFO sustains up to the doping level of x = 0.05, and then it exhibits a mixed structure (*R3c*+ *Pn21a*) up to $0.1 \leq x \leq 0.15$. The structure transforms to *Pn21a* for x = 0.2 and beyond that the structure transforms to orthorhombic *Pnma*. Dielectric constant increases to three folds with Gd doping. Great enhancement in the remnant magnetization (M_r) and H_C values over the undoped system is observed in Gd doped samples and is due to the destruction of spin cycloid structure and the interactions between Gd^{3+}

and Fe^{3+}. The effect of increase in ε_r and M on the magneto-electric effects needs to be investigated in these samples.

We have also successfully synthesized $Bi_{1-x}Ho_xFeO_3$ (x = 0 - 0.2) ceramic samples through solid-state reaction method. XRD and Raman measurements reveal a structural phase transition for x = 0.2. The rhombohedral phase with *R3c* symmetry of BFO sustains up to the doping level of $x \leq 0.15$ and beyond that the structure changes to orthorhombic *Pnma*. Dielectric constant increases twice with Ho doping content x = 0.05. Great enhancement in the remnant magnetization (M_r) and H_C values over the undoped system is observed in Ho doped samples and is due to the destruction of spin cycloid and the new interaction between Ho^{3+} and Fe^{3+}.

REFERENCES

[1] R. Ramesh and N. A. Spaldin, *Nature Materials* **6**, 21 (2007).

[2] A. Z. Simões, E. C. Aguiar, A. H. M. Gonzalez, J. Andrés, E. Longo and J. A. Varela, *J. Appl. Phys.* **104,** 104115 (2008).

[3] G. LeBras, P. Bonville, D. Colson, A. Forget, N. Genand-Riondet and R. Tourbot, *Physica B* **406** 1492 (2011).

[4] S. Y. Wang, X. Qiu, J. Gao, Y. Feng, W. N. Su, J. X. Zheng, D. S. Yu and D. J. Li, *Appl. Phys. Lett.* **98** 152902 (2011).

[5] Z. V. Gabbasova, M. D. Kuz'min, A. b. Zvezdin, I. S. Dubenko, V.A. Murashov, D. N. Rakov and I. B. Krynetsky, *Physics Letters A* **l58** 491 (1991).

[6] S. T. Zhang, Y. Zhang, M. H. Lu, C. L. Du and Y. F. Chen et al, *Appl. Phys. Lett.* **88**, 162901 (2006).

[7] G. L. Yuan, S. W. Or and H. L. Chan, *J. Phys. D: Appl. Phys.* **40** 1196 (2007).

[8] M.A. Ahmed, S.I. El-Dek, Materials Science and Engineering B 128, 30 (2006)

[9] V. A. Khomchenko, I. O. Troyanchuk, M. V. Bushinsky, O. S. Mantytskaya, V. Sikolenko and J. A. Paixão, *Materials Letters* **65** 1970 (2011).

[10] S. T. Zhang, L. H. Pang, Y. Zhang, M. H. Lu, and Y. F. Chen, *ceramics J. Appl. Phys.* **100** 114108 (2006).

[11] Y. Du, Z. X. Cheng, M. Shahbazi, E. W. Collings, S. X. Dou and X. L. Wang, *J. Alloys Compd.* **490** 637 (2010).

[12] K. J. Andrew, *J. Phys. D: Appl. Phys.* **32** R57 (1999).

[13] K. Sen, K. Singh, A. Gautam and M. Singh, *Ceram. Inter.* **38** 243 (2012).

[14] R. Mazumder and A. Sen, *J. Alloys Compd.* **475** 577 (2009).

[15] D. Lebeugle, D. Colson, A. Forget, M. Viret, A. M. Bataille and A. Gukasov, *Phys. Rev. Lett.* **100** 227602-1. (2008).

[16] J. Wang, A. Scholl, H. Zheng, S. B. Ogale, D. Viehland, D. G. Schlom, N. A. Spaldin, K. M. Rabe, M. Wuttig, L. Mohaddes, J. Neaton, U. Waghmare, T. Zhao and R. Ramesh, *Science* **307** 1203b (2005).

[17] V. A. Khomchenko, D. A. Kiselev, J. M. Vieira, L. Jian, A. L. Kholkin, A. M. L. Lopes, Y. G. Pogorelov, J. P. Araujo and M. Maglione, *J. Appl. Phys.* **103** 024105 (2008).

[18] R. Radheshyam, S. K. Mishra, N. K. Singh, S. Sharma and L. A. Kholkin, *Appl. Phys.***11** 508 (2011).

[19] Z. X. Cheng, X. L. Wang, Y. Du and S. X. Dou, *J. Phys. D: Appl. Phys.* **43** 242001 (2010).

[20] Y. J. Zhang, H. G. Zhang, J. H. Yin, H. W. Zhang, J. L. Chen, W. Q. Wang and G. H. Wu, *J. Magn. Magn. Mater.* **322** 225 (2010).

[21] Y. H. Lin, Q. Jiang, Y. Wang, C. W. Nan, L. Chen and J. Yu, *Appl. Phys. Lett.* ***90*** 172507 (2007).

[22] P. Thakuria and P. A. Joy, *Appl. Phys. Lett.* **97** 162504 (2010).

[23] V. A. Khomchenko, V. V. Shvartsman, P. Borisov, W. Kleemann, D. A. Kiselev, I. K. Bdikin, J. M. Vieira, and A. L. Kholkin, *Acta Materialia* **57**, 5137 (2009).

[24] J. B. Li, G. H. Rao, Y. Xiao, J. K. Liang, J. Luo, G. Y. Liu, and J. R. Chen, *Acta Materialia* **58,** 3701 (2010).

[25] R. Guo, F. Liang, D. Wen, F. Zheng, and M. Shen, *J. Phys. Chem. C.* **114**, 21390 (2010).

[26] W. Hu, Y. Chen, H. Yuan, G. Li, Y. Qiao, Y. Qin, and F. Shouhua, *J. Phys. Chem. C.* **115,** 8869 (2011).

[27] Y. Chen, Q. Wu, and Z. Jing, *J. Alloys Compd.* **487**, 599 (2009).

[28] S. Karimi, I. M. Reaney, Y. Han, J. Pokorny, and I. Sterianou, *J. Mater. Sci.* **44**, 5102 (2009).

[29] L. G. Singh and N. K. Verma, *J. Nanopart.* Res**. 14**, 742 (2012).

[30] V. A. Khomchenko, D. A. Kiselev, I. K. Bdikin, V. V. Shvartsman, P. Borisov, W. Kleemann, J. M. Vieira, and A. L. Kholkin, *Appl. Phys. Lett.* **93**, 262905 (2008).

[31] G. K. Rozenberg, M. P. Pasternak, W. M. Xu, L. S. Dubrovinsky, S. Carlson, and R. D. Taylor, *Europhys. Lett.* **71**, 228 (2005).

[32] H. C. Gupta, M. K. Singh, and L. M. Tiwari and J. Raman *Spectrosc.33***, 67** (2002).

[33] V. V. Lazenka, G. Zhang, J. Vanacken, I. I. Makoed, A. F. Ravinski, and V. V. Moshchalkov, *J. Phys. D: Appl. Phys.* **45,** 125002 (2012).

[34] S. Mathur, M. Veith, R. Rapalaviciute, S. Hao, F. G. Gerardo, F. W. L. Martins, and S. B. Thelma, *Chem. Mater.* **16**, 1906 (2004).

Effect of (La, Gd) co-doping on multiferroic properties of $BiFeO_3$

5
Chapter

Abstract:–

The single site doping of $BiFeO_3$ (BFO) by La at A-site is effective in stabilizing the perovskite *R*3*c* phase, reducing dielectric loss and improving the H_C. Similarly, doping with Gd results in the observation of high magnetization along with the improvement in dielectric constant of BFO. Hence, improvement in the electric and magnetic order parameters can be achieved by co-doping of these two ions at A-site of ABO_3 type perovskite BFO. Hence, the ceramics of $La_xGd_yBi_{0.8}FeO_3$ (LGBFO) for (*x, y)* = (0.05, 0.15); (0.1, 0.1); (0.15, 0.05) are prepared through solid state reaction method. XRD show that as La content increases, the impurity phases reduce and stabilizes the phase of BFO. Whereas, Gd doping is not effective for phase stabilization. There is no structural phase transition observed within the compositional range of doping. The morphology shows that the density of the samples increases monotonically and reaches about 92 % for the $x = 0.15$ sample. The Raman modes show significant changes in the mode frequencies confirming the changes in Bi-O and Fe-O bonds due to substitution at Bi^{3+}. A maximum value in dielectric constant is achieved with low dielectric loss for a particular composition of $x, y = 0.1$. M-H loops at 9 T show the presence of ferromagnetic and antiferromagnetic (AFM) contribution. M_r and M_{9T} increases with Gd content but H_C increases with La. A minimum in the M-T curve is observed in the 100 Oe field, around 290 K, which is caused due to the two sub lattice interactions.

5.1. Introduction

There are many reports on the single site doping (doping either at A-site or B-site) in $BiFeO_3$ (BFO) [1-3] in which the improvement in the electric and magnetic properties is achieved effectively subject to the type of element and doping site. The control over both the order parameters can also be achieved by co-doping method. In this context, recently, A and B sites co-doped BFO such as Bi^{3+} ions by La^{3+} or Nd^{3+} and Fe^{3+} ions by Mn^{4+}, V^{5+}, Ti^{4+} have paid a growing interest as they seem to improve the electric and magnetic properties, simultaneously [4, 5]. So far, there have been reports on the co-doping simultaneously at A and B sites of BFO, focusing on the phase stabilization, leakage current and improvement in magnetic properties. In such co-doping, the electric properties are governed by the A-site element whereas the B-site element is responsible for the improvement in the magnetic properties. But, dilution of Fe with any other transition metal leads to reduction of d^n electrons, which are responsible for exhibiting the magnetization. But, A-site co-doping by some ions with similar ionic radius can induce more decrease in the Fe–O–Fe bond angle accompanying the structural changes leading to improved multiferroicity at room temperature. In this respect, there are few reports on the A-site co-doping such as La^{3+} and V^{5+}, enhance the dielectric and ferroelectric properties of BFO ceramic [5]. Singh *et al* [6] and Cheng *et al* [7] reported that both the BFO

films co-doped with La and Ni^{2+}, and with La^{3+} and Nb^{5+}, respectively, had reduced leakage current and improved ferroelectric properties. However, there are very few reports on the improvement of the both electrical and magnetic properties of the A-site co-doped BFO. In the literature, it is well established that the substitution of La in Bi is effective in stabilizing the perovskite phase [8], reducing leakage current [9] and enhancing the magnetic properties of BFO [10]. On the other hand, Gd, a rare earth magnetic element is very effective to increase the magnetization along with electrical properties compared to other rare earth elements when doped at A-site of BFO [11, 12]. Therefore, it is interesting to investigate the effect of A-site co-doping with La and Gd on the electrical and magnetic properties of the BFO material in order to combine the advantages of La and Gd dopings. Hence, in this chapter, a systematic study on the effect of La and Gd co-doping in BFO is carried out. Here La^{3+} and Gd^{3+} partially substitute for Bi^{3+} at the A-site of BFO such that the stoichiometry of A-site doping (La+Gd) is always maintained at 20% thereby the stoichiometry of Bi is fixed at 80%. The role of each dopant on the structure, electric and magnetic properties is discussed in detail.

5.2. Experimental details

The ceramics of $La_xGd_yBi_{0.8}FeO_3$ (LGBFO) for (x, y) = (0.05, 0.15); (0.1, 0.1); (0.15, 0.05) were prepared by the conventional solid state reaction method by taking the stoichiometric ratios of Bi_2O_3, La_2O_3, Gd_2O_3 and Fe_2O_3 powders as precursors. All the characterization techniques mentioned in the experimental section (chapter 2) are used to characterize the material to study their properties.

5.3. Results and discussion

5.3.1. Structural Analysis

The obtained XRD pattern of LGBFO for x = 0.05, 0.1 and 0.15 samples are shown in figure 5.1. The secondary phases, which are present in undoped BFO (not shown in the figure) exists in all the XRD patterns shown in the figure 5.1. However, a careful observation of the XRD spectra reveals that with increase in La doping, the percentage of this impurity phase gets suppressed that means La stabilizes the single phase BFO. This is also observed in our previous studies on La doped BFO samples as discussed in chapters 3(b) and 4(a). Whereas, Gd doping is not effective for phase stabilization as the impurity peaks still exists with Gd doping. To further investigate the influence of La^{3+}, Gd^{3+} doping on the structure of LGBFO, magnified XRD pattern near 32° is shown in the inset of figure 5.1. It can be clearly seen that with increasing x, the split reflections (1 0 4) and (1 1 0) shifted to a higher

diffraction angle. This indicate a gradually decreased lattice distance of these planes caused by the crystal distortion of the samples due to varying doping concentrations and different ion radii between La^{3+}(1.22 Å) and Gd^{3+}(1.05 Å) compared with Bi^{3+}(1.14 Å).

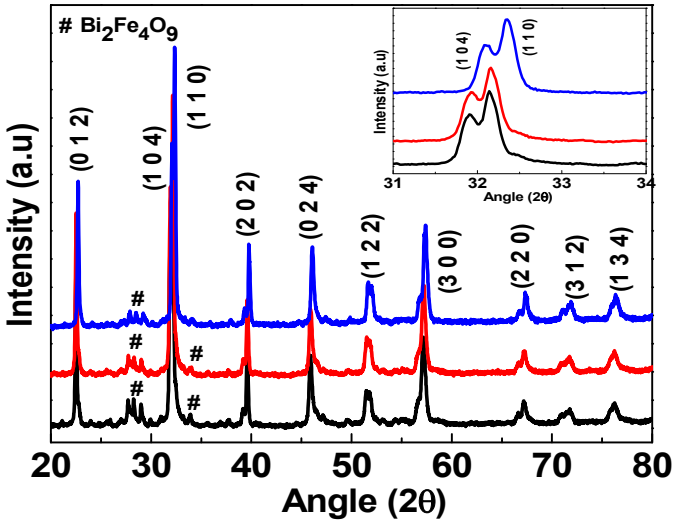

Figure 5.1 XRD of $La_xGd_yBi_{1-x-y}FeO_3$ (x = 0.05, 0.1, and 0.15) ceramics. Inset shows the magnified view of the diffraction peaks at 32°

Detailed Rietveld refinement of these XRD data depicted in figure 5.2 reveal that these systems belong to rhombohedral structure with *R3c* space group and structural parameters thus obtained are tabulated in table 5.1. In comparison to the pure sample, the refined lattice parameters, $a = b \neq c$ and the corresponding cell volume (V) and also bond angle Fe-O-Fe (°) found to decrease systematically as x increases, indicating the distortion in the crystal lattice. In our previous work

(chapter 4), A-site doping of La results a mixed structure of (*R3c+Pbnm)* for the concentrations 5 % - 40 %, whereas a structural transition to (*R3c*+ *Pn21a)* is observed for 15% Gd doping concentration. But in the present study, no such structural transition to either *Pbnm* or *Pn21a* is observed over all the doping range. This is because La with higher ionic radius and Gd with lesser ionic radius than Bi occupy the same Bi-site and presumably maintain the structure in *R3c* phase.

Table 5.1. Refined structural parameters for $La_xGd_yBi_{0.8}FeO_3$ samples.

Composition	*a*(Å)	*b*(Å)	*c*(Å)	*V*(Å^3)	Fe-O_2-Fe (°)	Bi-O_2 (Å)
BFO	5.620(7)	5.620(7)	13.692(4)	374.62(5)	153.42	2.889
x=0.05,	5.5829(5)	5.5829(5)	13.825(9)	373.20(8)	153.04	2.858
x=0.1,	5.4634(8)	5.4634(8)	13.641(7)	352.64(3)	152.49	2.813
x=0.15,	5.3860(3)	5.3860(3)	13.406(6)	336.81(9)	152.14	2.794

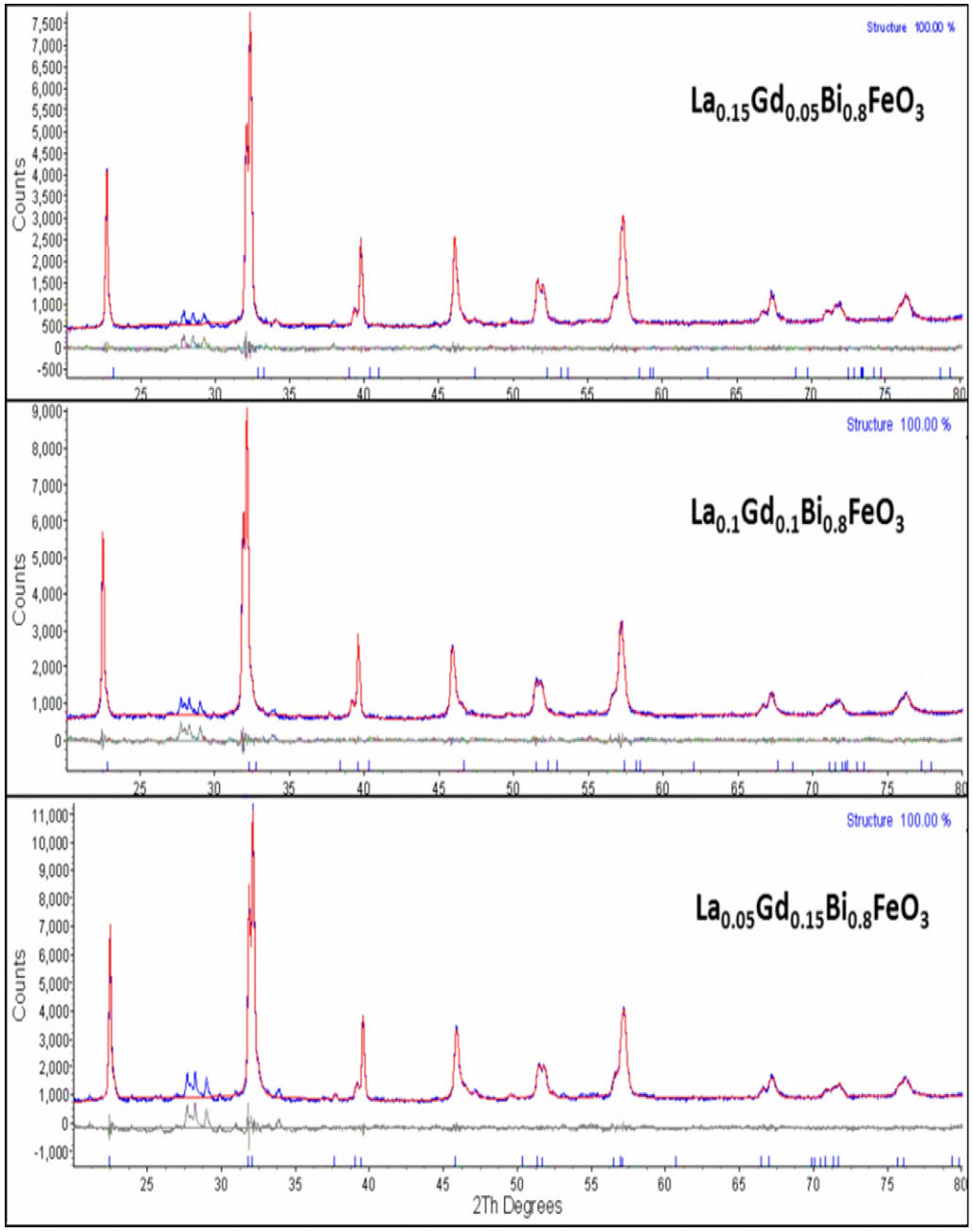

Figure 5.2. Rietveld refinement of the XRD data for LGBFO samples. Observed (red lines), calculated (blue line), and difference (bottom line) profiles are shown. The Bragg reflections are marked by vertical bars corresponds to *R*3*c* phase.

5.3.2. Surface morphology

In order to find the grain size distribution in these samples, the morphology of LGBFO has been studied. The typical FE-SEM images of the samples at different La (x), Gd (y) compositions are shown in figure 5.3. It can be found that the grain size becomes larger as the La doping concentration increases and the distribution of the grain size is inhomogeneous. The estimated average grain size is about ~ 1 μm, 1.2 μm, and 1.4 μm for the samples with compositions x = 0.05, 0.1 and 0.15, respectively. The FE-SEM image also show that some porosity exists among the loosely connected grains especially for the low concentrations of the La doped samples. With the increase in the grain size, the density of the samples increases monotonically and reaches about 92% for the x = 0.15 sample.

The energy dispersive x-ray (EDS) analysis carried out show observable signals for O, Bi, and Fe elements while weak signals for La and Gd confirming the chemical homogeneity of the samples. The composition of the La and Gd varies in accordance with the doping level. The EDS spectra of the sample with x = 0.15 has the estimated ratio between La, Gd, Bi and Fe at different places is approximately 0.13: 0.06: 0.9: 1, revealing the compositional homogeneity of the sample.

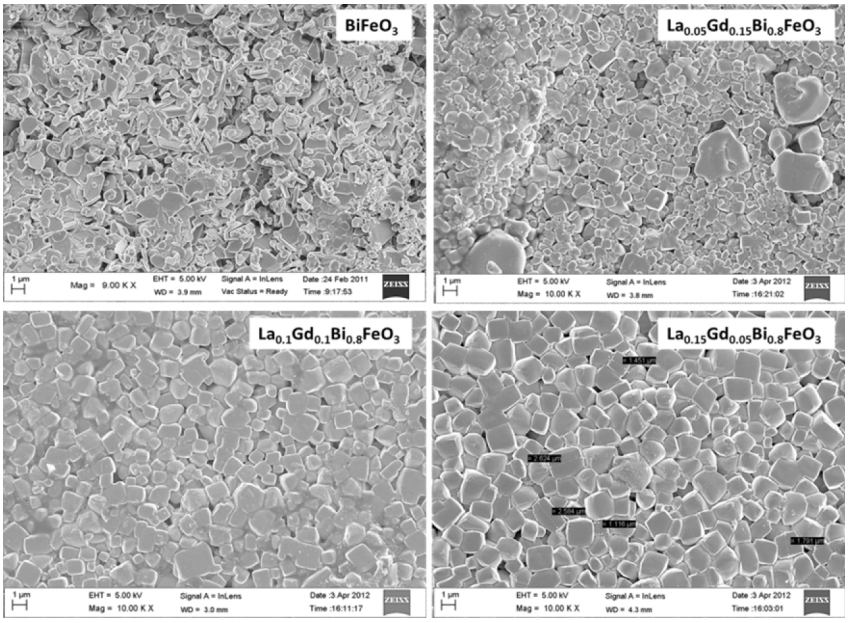

Figure 5.3 FE- SEM Images of $La_xGd_yBi_{1-x-y}FeO_3$ samples.

5.3.3. Raman Spectroscopy studies

In order to understand the effect of co-doping on the lattice dynamics, the vibrational modes of the samples under present study are recorded by Raman spectroscopy at room temperature. The variation in the Raman modes with respect to La and Gd content level will provide the information about the structural changes. The Raman modes of LGBFO with different doping concentrations are plotted in figure 5.4(a). The decrease of low frequency A_1 mode intensities (136, 169, 215 and 438 cm^{-1}) of the LGBFO confirms La^{3+} and Gd^{3+} substitution at the Bi^{3+} site.

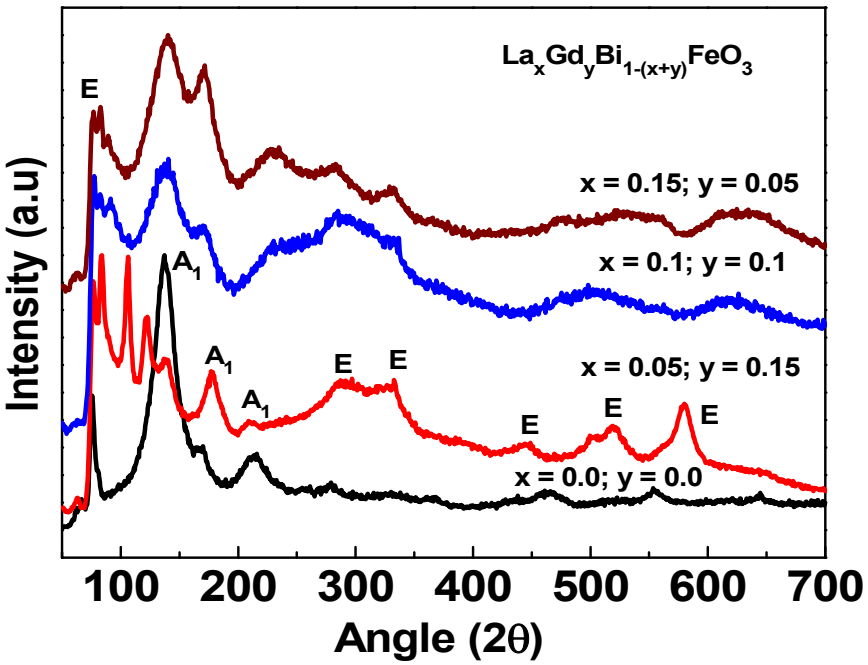

Figure 5.4 (a) Raman spectra of $La_xGd_yBi_{0.8}FeO_3$ samples.

Raman mode frequencies as a function of La content are plotted in figure 5.4 (b). From the figure, it is clear that some of the modes related to parent compound disappear with doping and a new mode at 90 cm^{-1} is observed in all the co-doped samples. The shift in the modes below 200 cm^{-1} is due to the decrease in Bi-O bond length (table 5.1) with an increase in x. The disappearing of the low frequency modes indicate that some of Bi - O bonds are missing due to the introduction of La and Gd. In our previous studies on Gd doped BFO, a peak (A_g) with high scattering intensity at 300 cm^{-1} is observed, which correspond to $GdFeO_3$

orthorhombic phase [13]. But this peak is absent in the present case even for the highest Gd doping (y = 0.15) suggesting the absence of a structural phase transition to orthorhombic phase in co-doped samples.

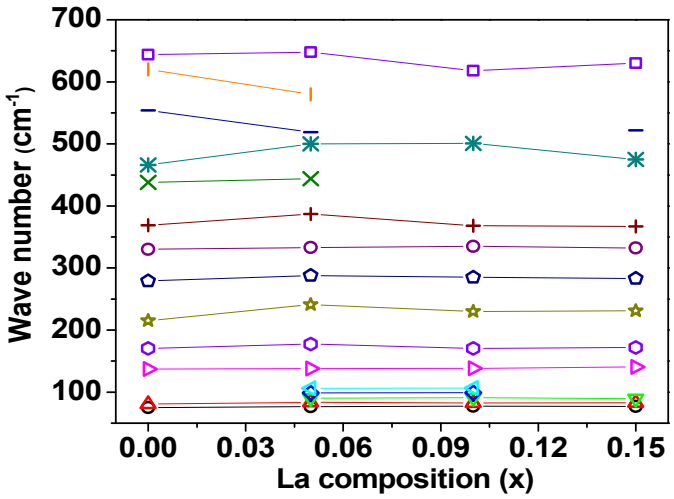

Figure 5.4(b) Raman mode frequency verses La concentration of $La_xGd_yBi_{0.8}FeO_3$ (x = 0, 0.05, 0.1 and 0.15) samples.

5.3.4. Dielectric properties

Figure 5.5 shows the measured dielectric constant and dielectric loss at room temperature for a frequency range of 20 Hz- 2 MHz. It is observed that the dielectric constant of the bismuth ferrite is greatly improved with a decrease in the dielectric loss due to co-doping. The value of the dielectric constant for pure BFO at 1 MHz is found to be 60, which increases to a maximum value of 135 for a particular composition of x, y = 0.1. For this composition, dielectric loss also reduces but the

lowest loss is found for the highest doping concentration of La (x = 0.15, y = 0.05). The improvement in the dielectric constant is due to crystal distortion brought about by co-doping which favors the polarization. Also, the substitution of Gd^{3+} can compensate for the oxygen vacancies if any, since the bond dissociation energy of the Gd-O bond (719±6 kJ/mol) is stronger than that of the Bi-O bond (337±12 kJ/mol) [14, 15].

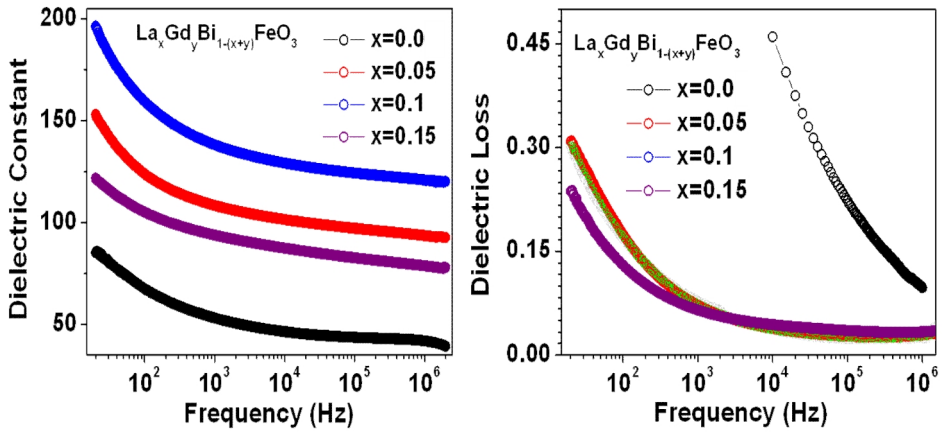

Figure 5.5. Dielectric constant vs. frequency of $La_xGd_yBi_{0.8}FeO_3$ (x = 0, 0.05, 0.1 and 0.15) samples at 300 K. Right panel shows dielectric loss verses frequency for different doping levels.

5.3.5. Magnetic properties

The M–H hysteresis loops of the LGBFO samples at different temperatures are shown in figures 5.6, 5.8 and 5.10. It is clear that a non-zero remnant magnetization (M_r) and coercive field (H_C) are observed for all samples. The magnetization curve at 2 K for x = 0.05 tends to

saturate (figure 5.6(b)) whereas all the other M-H loops do not saturate even with the field as high as 9 T showing the long range antiferromagnetic (AFM) correlations present in these samples. Magnetic parameters obtained from the M (H) loops with the LGBFO samples are summarized in table 5.2. Compared to the undoped BFO sample, the co-doping of La^{3+} and Gd^{3+} ions in BFO greatly improves the magnetization.

Table 5.2. Derived magnetic parameters of $La_xGd_yBi_{0.8}FeO_3$ samples at different temperatures.

Sample		2 K			300 K	
	M at 9 T (emu/g)	H_C (T)	M_r (emu/g)	M at 9T (emu/g)	H_C (T)	M_r (emu/g)
x = 0.0	0.41	0.0005	0.0006	0.40	0.0003	0.0005
x = 0.05	12.43	0.08	0.51	1.68	0.88	0.19
x = 0.1	10.09	0.082	0.43	1.47	0.91	0.17
x = 0.15	6.90	0.112	0.35	1.33	1	0.18

A closer look at the M-H loops measured at 2 K and 300 K show that the loops have a clear opening with a good coercivity even at 300 K. The temperature dependence of H_C and M_r for x = 0.05, 0.1 and 0.15 are shown in figures 5.7, 5.9 and 5.11 respectively. The H_C increases with an increase in temperature for all the samples, whereas a sharp drop in M_r is seen for all samples at low temperatures.

The doping of La and Gd independently in $BiFeO_3$ known to effectively modify its space modulated spin structure and liberate the magnetization locked within the cycloid resulting in a remarkable enhancement in H_C and M_r [16, 17]. In these co-doped samples, the dilution of the spin cycloidicity and the decrease in the bond lengths (Bi-O), bond angle (Fe–O–Fe) is a result of distortion created by the La^{3+} and Gd^{3+} co-doping. This may also be a possible reason for the enhancement in magnetization as these changes in oxide systems generally influence the magnetic properties, having indirect exchange interactions [18-20]. Moreover, Gd doping brings additional magnetic interactions into the system. Hence, as the concentration of Gd (y) increases, a noticeable and systematic increase is observed in the remnant magnetization (M_r) and high field magnetization (M_{9T}) exhibiting the maximum values for the highest Gd doping composition of y = 0.15 in the entire temperature region. In contrast, the value of H_C follows an opposite trend as it decreases systematically with Gd content (i.e. x increases) and possesses a maximum H_C of 1 T for x = 0.15. This is due to the high coercivity exhibited by the La doped BFO compared to Gd doped BFO. That means La controls the H_C while Gd is responsible for the enhancement in M_r and M_{9T}. However, more thorough studies are needed to differentiate between each element contribution. The M versus H curves tends to approach the saturation at 2 K and show a high field

susceptibility at 300 K, and the magnetization curves do not show any tendency to saturate even at 9 T, which is due to the uncompensated antiferromagnetic nature persisting in the samples. But interestingly the H_C value increases as the temperature of the sample increases for all the compositions. Thus, it is evident that at room temperature these compounds have noticeable ferromagnetic contribution along with usual AFM. Thus, the coexistence of two magnetic phases such as ferromagnetism and anti-ferromagnetism results in the appearance of the unsaturated hysteresis loops with high coercivity.

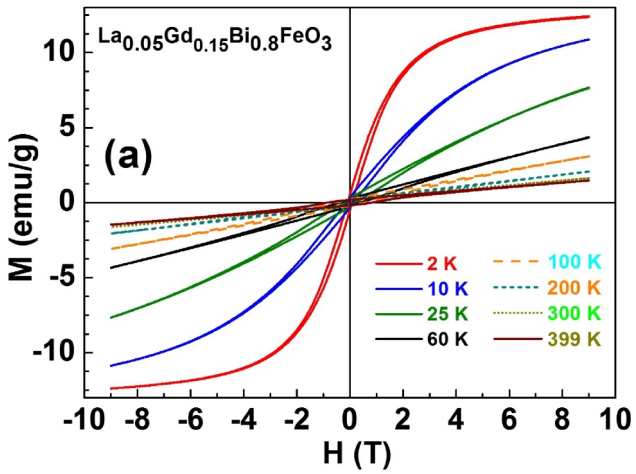

Figure 5.6 (a) M-H loops of $La_xGd_yBi_{0.8}FeO_3$ for x = 0.05 at different temperatures.

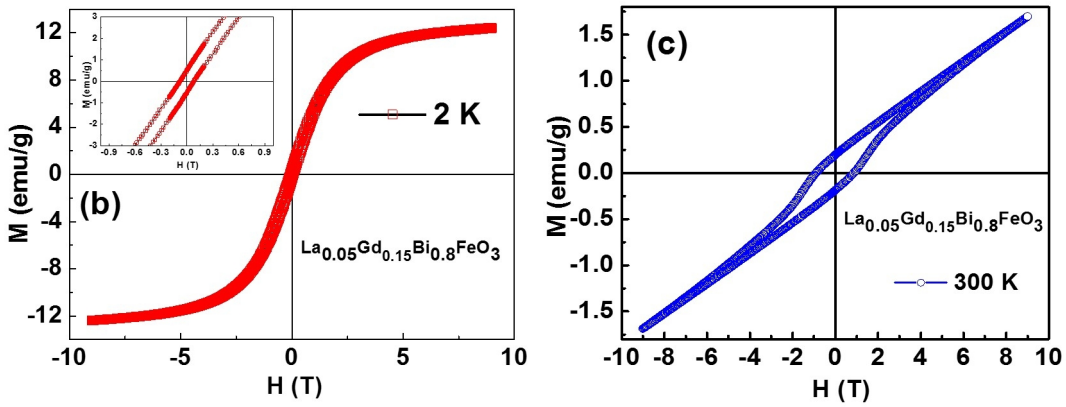

Figure 5.6 (b, c) M-H loops of $La_xGd_yBi_{0.8}FeO_3$ for $x = 0.05$ at (b). 2 K and (c). 300 K.

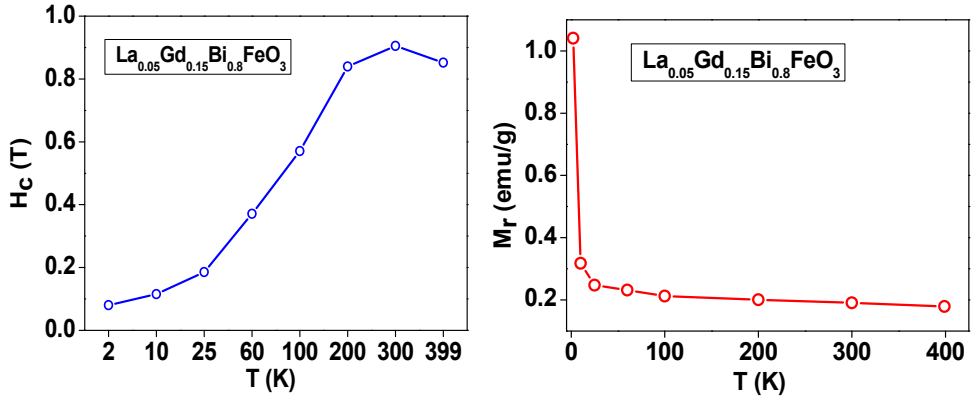

Figure 5.7 Temperature dependence H_C and M_r of $La_xGd_yBi_{0.8}FeO_3$ for $x = 0.05$.

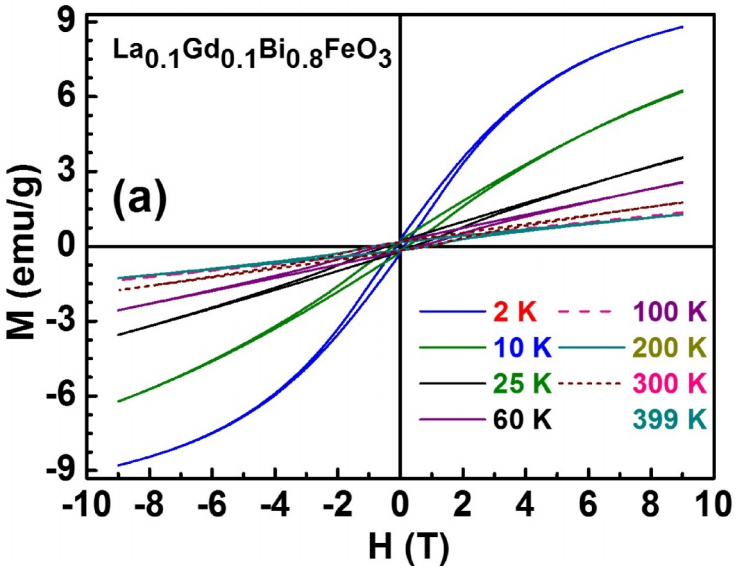

Figure 5.8 (a) M-H loops of $La_xGd_yBi_{0.8}FeO_3$ for $x = 0.1$ at different temperatures.

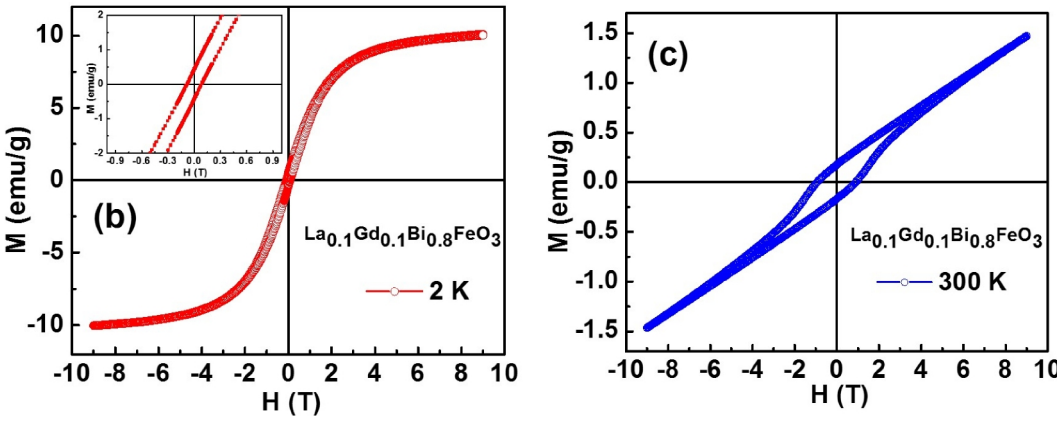

Figure 5.8 (b, c) M-H loops of $La_xGd_yBi_{0.8}FeO_3$ for $x = 0.1$ at (b) 2 K and (c) 300 K.

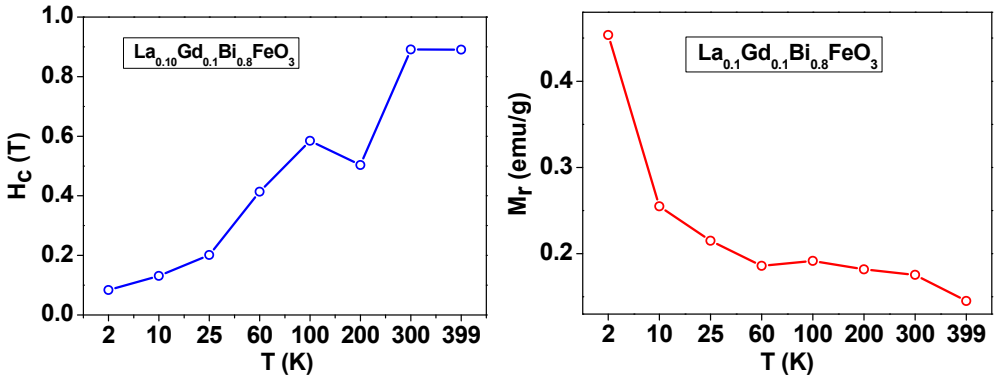

Figure 5.9 Temperature dependence H_C and M_r of $La_xGd_yBi_{0.8}FeO_3$ for $x = 0.1$.

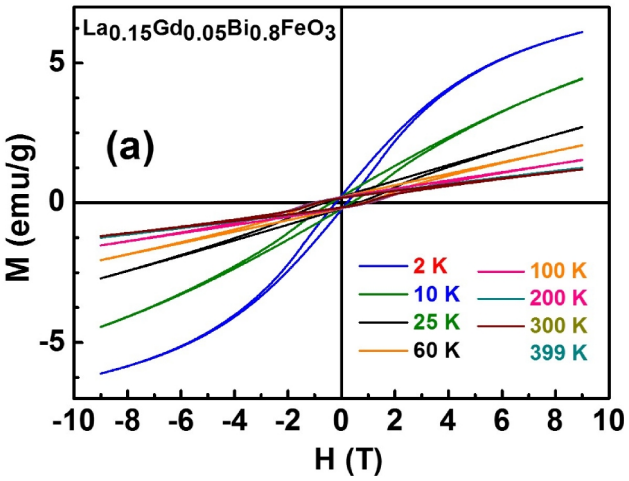

Figure 5.10 (a) M-H loops of $La_xGd_yBi_{0.8}FeO_3$ for $x = 0.15$ at different temperatures.

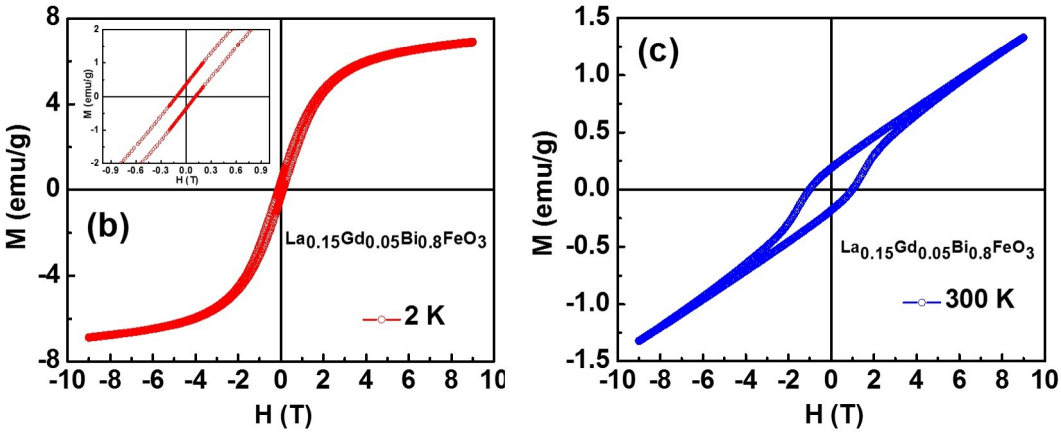

Figure 5.10 (b, c) M-H loops of $La_xGd_yBi_{0.8}FeO_3$ for $x = 0.15$ at (b).2 K and (c).300 K.

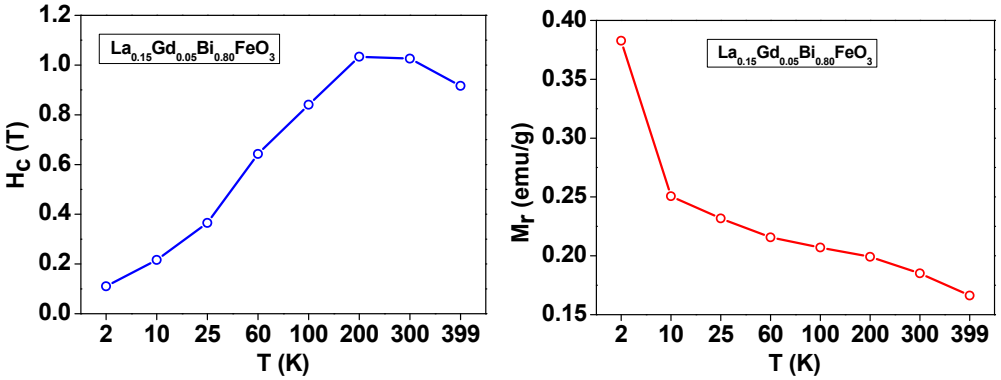

Figure 5.11 Temperature dependence H_C and M_r of $La_xGd_yBi_{0.8}FeO_3$ for $x = 0.1$.

The ZFC and FC measurements are carried out in two different field ranges namely 100 Oe and 1000 Oe (figure 5.12, 5.13 and 5.14) in the temperature range of 5 K - 300 K. From the graph, it is clear that the magnetization increases as temperature decreases due to ordering of

moments at low temperature and a sudden rise in the magnetization is seen below 50 K for all the samples due to the ordering of magnetic moment of Gd^{3+}. Similar results are observed in the recent studies on Gd doped samples [21]. In conformity to M-H data, the M-T curve shows the increase in the magnetization with Gd content. The value of the magnetization increases from 0.015 emu/g for x = 0 to 0.34 emu/g for a small amount of Gd doping, x = 0.05, and it reaches a maximum of 0.70 emu/g for x = 0.15 at 3 K for the applied external field of 1000 Oe. This enhancement in the magnetization can be attributed to the change in Fe – O – Fe bond angle due to the crystal distortion. Our refinement results show a decrease in the bond angle and bond lengths with x (table 5.1) indicating the distortion in the crystal. From the figures 5.12 and 5.13, the magnetization value increases with the field and a minimum in the M-T curve is observed in the 100 Oe fields, which is completely suppressed by the applied field value 1000 Oe. However, this observed minimum is not present for the sample, this minimum in M-T around 290 K may be due to the two sub lattice interactions. Here, La and Gd form a sublattice in which the interaction between the spins is mainly ferromagnetic and Fe makes the second sublattice consisting of canted antiferromagnetic interaction with in the sublattices. These two sublattices interact antiferromagnetically. At low temperatures the field holds the anti-parallel alignment of the spins and moment seems to

decrease up to certain temperature but as the temperature increases, the AFM alignment disrupts due to thermal agitation and there by spins try to align parallel results in the increase in the moment at high temperatures. The increase in coercivity with increase in temperature may be due to the presence of complex temperature dependence of anisotropy and sublattice magnetizations in these systems.

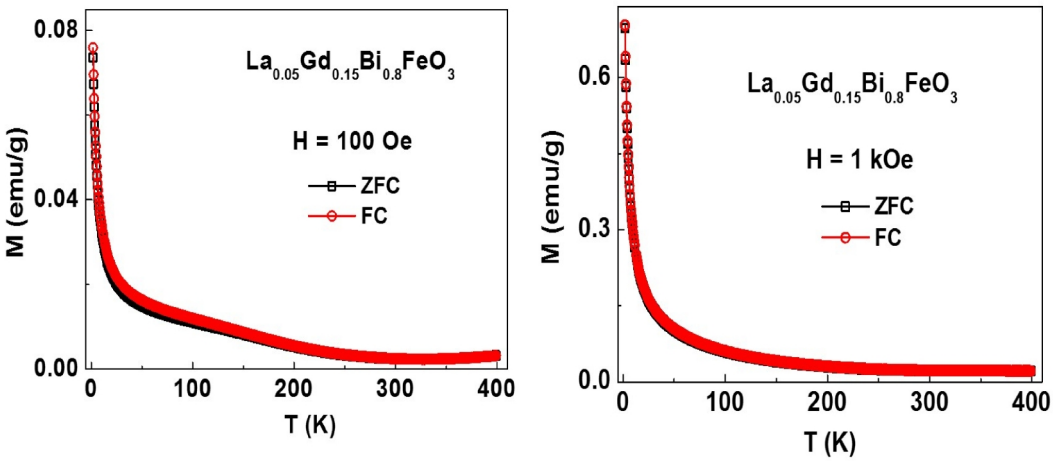

Figure 5.12 Temperature dependent magnetization curves (M-T) from 2 K to 400 K of $La_{0.05}Gd_{0.15}Bi_{0.8}FeO_3$.

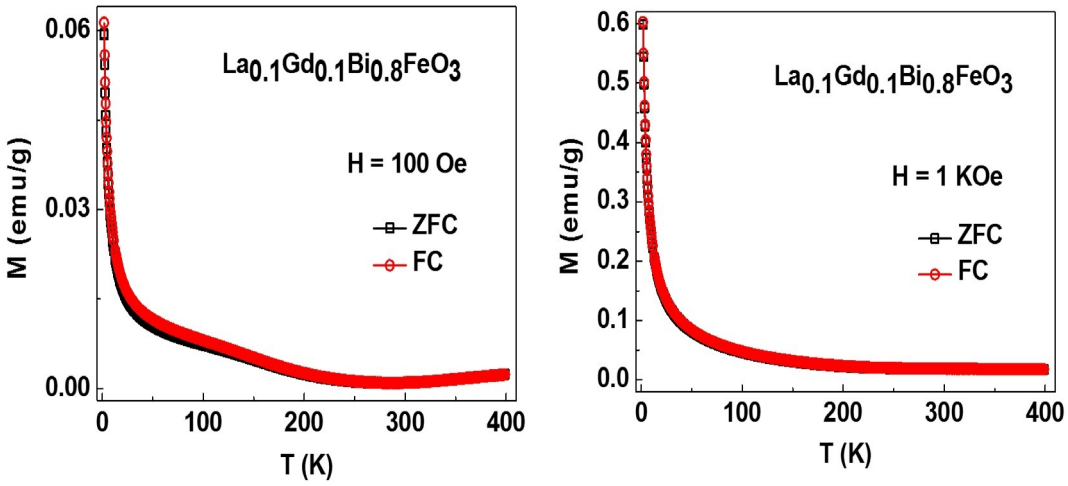

Figure 5.13. Temperature dependent magnetization curves (M-T) from 2 K to 400 K of $La_{0.1}Gd_{0.05}Bi_{0.8}FeO_3$.

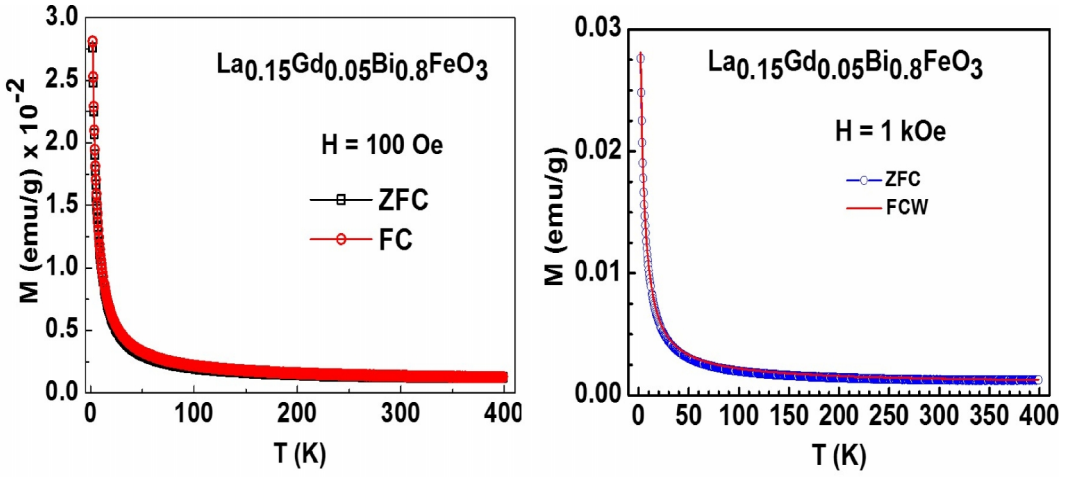

Figure 5.14. Temperature dependent magnetization curves (M-T) from 2 K to 400 K of $La_{0.15}Gd_{0.05}Bi_{0.8}FeO_3$.

5.4. Summary

In summary, we have successfully synthesized $La_xGd_yBi_{0.8}FeO_3$ (LGBFO) for (*x, y)* = (0.05, 0.15); (0.1, 0.1); (0.15, 0.05) ceramic samples through solid state reaction method. The multiferroic properties of LGBFO samples improve greatly with La-Gd co-doping retaining the crystal structure of the parent compound. The enhancement in the dielectric constant with a reduction in the loss is achieved for an optimal concentration of co-doping. Improvement in the magnetization along with coercivity is achieved in these systems.

References

[1] P. Thakuria and P. A. Joy, *Appl. Phys. Lett.* **97**, 162504 (2010).

[2] I. O. Troyanchuk, N. V. Tereshko, A. N. Chobot, M. V. Bushinsky, K. Barner, *Physica B* **404,** 4185 (2009).

[3] Y-j Zhang, H-g Zhang, J-h Yin, H-w Zhang, W-q Wang, J-l Chen and G-h Wu, *J. Mag. Mag. Mater.* **322**, 2251 (2010).

[4] B. F. Yu, M. Y. Li, J. Liu, D. Y. Guo, L. Pei and X. Z. Zhao, *J. Phys. D: Appl. Phys***. 41,** 065003 (2008).

[5] B. F. Yu, M. Y. Li, J. Wang, L. Pei, D. Y. Guo and X. Z. Zhao, *J. Phys. D: Appl. Phys.* **41,** 185401(2008).

[6] S. K. Singh, K. Maruyama and H. Ishiwara, *Appl. Phys. Lett.* **91,** 11291(2007).

[7] Z. X. Cheng, X. L. Wang, S. X. Dou, H. Kimura and K. Ozawa, *Phys. Rev. B*. **77,** 092101 (2008).

[8] P. Suresh and S. Srinath, *J. Alloys. Comp.* **554** 271 (2013).

[9] S. Y. Wang, X Qiu, J. Gao, Y Feng, W. N. Su, J. X. Zheng, D. S. Yu and D. J. Li, *Appl. Phys. Lett*. **98**, 152902 (2011).

[10] Z. X. Cheng, A. H. Li, X. L. Wang, S. X. Dou, K. Ozawa, H. Kimura, S. J. Zhang and T. R. Shrout, *J. Appl. Phys.* **103,** 07E507 (2008).

[11] V. A. Khomchenko, W. Kleemann, D. A. Kiselev, J. M. Vieira, I. K. Bdikin, V. V. Shvartsman, P. Borisov and A. L. Kholkin, Appl. Phys. Lett. **93**, 262905 (2008)

[12] P Suresh and S Srinath, *Materials Focus* **2**, 201(2013).

[13] G. K. Rozenberg, M. P. Pasternak, W. M. Xu, L. S. Dubrovinsky, S. Carlson, and R. D. Taylor, *Europhys. Lett.* **71**, 228 (2005).

[14] C. Chang and D. Mao, *Int. J. Chem. Kinetics*, **39**, 75 (2007).

[15] F. Yan, T. J. Zhu, M. O. Lai, and L. Lua, *Scr. Mater.* **63**, 780, (2010).

[16] S. T. Zhang, L. H. Pang, Y. Zhang, M. H. Lu, Y. F. Chen, *J. Appl. Phys.* **100,** 114108 (2006).

[17] S. Kazhugasalamoorthy, P. Jegatheesan, R. Mohandoss, N.V. Giridharan, B. Karthikeyan, R. Justin Joseyphus and S. Dhanuskodi, *J. Alloys Compd.* **493,** 569 (2010).

[18] J. S. Srikiran, A. B. Shinde and P. S. R. Krishna, *J. Phys.* **63,** 221 (2004).

[19] I. A. Abdel-Latif, A. S. Khramov, V. A. Trounov, O. P. Smirnov, Sh. Bashkirov, V. V. Parfenov, E. A. Tserkovnaya, G. G. Gumarov and Sh. Z. Ibragimo, *Egypt. J. Solids* **29,** 350 (2006).

[20] R. Mazumder, P. Sujatha devi, Dipten Bhattacharya, P. Choudhury and A. Sen Raja, *Appl. Phys. Lett.* **91,** 062510 (2007).

[21] V.A. Khomchenko, V.V. Shvartsman, P. Borisov, W. Kleemann, D.A. Kiselev, I.K. Bdikin, J.M. Vieira and A.L. Kholkin, *Acta Materialia* **57,** 5137 (2009).

Summary and Future Scope of the Present Thesis

6 Chapter

6.1. Summary

6.1.1. Preparation of pure and La doped $BiFeO_3$: effect of synthesis route

Bismuth ferrite is prepared through solid state and sol gel reactions. Solid-state reaction method does not form pure compound, but sol-gel method helps in removing the secondary phases for the optimal preparation conditions. The density of the samples is more for SG processed samples with a smaller grain size. A huge improvement in the dielectric constant at low frequencies is noticed for the SG prepared compounds due to Maxwell-Wagner contribution. The comparisons of various parameters are given in table 6.1.

Table 6.1 Magnetic and dielectric parameters of BFO prepared through SS and SG.

	Solid state		Sol-gel	
	5K	300 K	5K	300 K
M_r (emu/g)	5.9×10^{-5}	5.3×10^{-5}	0.01	0.01
H_C (Oe)	6.8	8.8	52	63
M_{7T} (emu/g)	0.40	0.40	0.57	0.53
ε_r at 10 kHz	----	60	----	150

Further, the effect of synthesis route on the Lanthanum doped BFO samples is studied in the compositional range x = 0 - 0.4. The SS processed samples exhibit a mixed structure of *R3c+Pbnm* for all compositional range whereas SG prepared samples show a complete structural change to *Pbnm* for $x > 0.2$. The smaller particle size ~0.4 μm of SG prepared samples results in the high densification and the dielectric constant increases. The comparison of various parameters for LBFO samples prepared through SS and SG are given in table 6.2.

Table 6.2 Magnetic and dielectric parameters of LBFO prepared through SS and SG.

La content	Solid state			Sol gel		
	300 K			300 K		
	H_C (kOe)	M_r (emu/g)	1 kHz	H_C (kOe)	M_r (emu/g)	1 kHz
$x = 0.0$	0.32	$5x10^{-4}$	53.23	0.853	$5.4x10^{-4}$	538.89
$x = 0.05$	12.1	0.13	127.91	5.91	0.076	12,696
$x = 0.2$	13.9	0.24	143.72	10.23	0.259	2520
$x = 0.4$	14.8	0.21	145.01	19.46	0.274	2187

6.1.2. Effect of Rare earth element (La, Gd and Ho) on the properties of $BiFeO_3$.

The effect of Rare earth element substitution on the structure, magnetic order and electric properties of the $BiFeO_3$ is investigated.

$RE_xBi_{1-x}FeO_3$ (*RE* = La, Gd and Ho) ceramics were synthesized successfully using high energy ball milled solid state route. Rietveld refinement shows a continuous structural evolution from rhombohedral *R3c* to orthorhombic *Pbnm*/*Pnma* phase as the RE doping increases.

The observed structural changes with different doping elements are tabulated below with respect to the concentrations (table 6.3). The variation in the structural changes is caused by the difference in the nature of dopant atom and its ionic radius.

Table 6.3 Structural changes of BFO with RE doping.

Dopant Element	**Composition (*x*)**	**Structure**
La	$0.05 < x < 0.4$	*R3c*+*Pbnm*
Gd	$0.1 < x < 0.15$	*R3c*+*Pn21a*
	0.2	*Pn21a*
	$0.2 < x < 0.35$	*Pnma*
Ho	$0.0 < x < 0.15$	*R3c*
	$x \geq 0.2$	*Pnma*

Dielectric constant (ε_r) is enhanced with the RE doping as the distortion occurred in the FeO_6 cage. All the RE dopants show an enhancement in the ε_r with along with the increase in dielectric loss

except lanthanum. La results in the observation of reduction in the dielectric loss with an increase in ε_r. Polarization hysteresis loops show that La doping results BFO into a hard ferroelectric and a significant improvement in the values of P_r is observed with all RE doping elements studied in this work.

M-H loops show a remarkable improvement in the H_C and M_r of BFO. With RE element substitution the antiferromagnetic (AFM) nature of BFO turns to ferromagnetic (FM). For La doped samples, a huge coercivity of the order of 1 Tesla is observed. Whereas great enhancement in the remnant magnetization (M_r) is observed in Gd doped samples. The high magnetization values are observed with the holmium doping. The improved magnetic properties are due to the destruction of spin cycloid structure and the interactions between Gd^{3+}, Ho^{3+} and Fe^{3+}. The Néel temperature (T_N) of the BFO increases with La doping, where as it is reduced with Gd and Ho content.

6.1.3. Effect of co-doping

La and Gd co-doping in the A-site of BFO showed improved properties. Enhancement in the ε_r with low dielectric loss is obtained for 10 % doping level. The improvement in H_C along with Mr is achieved with co-doping.

6.2. Future scope

- Bismuth ferrite is also a promising material for use as an optical filter, and as a part of communication devices, hence the study of its optical properties is highly anticipated.
- Micro magnetic modeling or numerical technique is required for finite analysis for the observed magnetic properties.
- Analyzing the magnetic properties using numerical techniques such as finite elemental analysis using the two sublattice model to quantify the sublattice magnetization and anisotropy.
- Need to understand the high dielectric constant in sol-gel prepared samples. What contribute to the observation of such a huge dielectric constant with high loss.
- Study of thin films of RE doped BFO using different substrates with mismatched lattice parameters with respect to BFO in order to induce epitaxial strain effects.
- Anisotropy measurements need to be carried out to understand the observed increase in H_C with temperature.
- The high temperature studies are required very much, especially structural transitions and its effect on electric and magnetic properties at high temperatures.

LIST OF PUBLICATIONS BASED ON THE RESEARCH WORK

1. A comparative study of sol–gel and solid-state prepared La^{3+} doped multiferroic $BiFeO_3$ (Accepted Article)
   Pittala Suresh and S. Srinath, ***Advanced Materials Letters***, *DOI:10.5185/amlett.2013.fdm.34*
2. Observation of high coercivity in multiferroic lanthanum doped $BiFeO_3$, **Pittala Suresh** and S. Srinath, ***Journal of Alloys and Compounds*** 554 271–276 (2013).
3. Crystal Structure and Enhanced Dielectric, Magnetic Properties of Gd Doped $BiFeO_3$ Ceramics,
   Pittala Suresh and S. Srinath, ***Materials Focus*** 2, 201–208, (2013).
4. Effect of La Substitution on Structure and Magnetic Properties of Sol-Gel Prepared $BiFeO_3$,
   Pittala Suresh and S. Srinath; ***Journal of Applied Physics*** *113, 17D920-1-3 (2013)*.
5. Role of La, Gd co- doping on the structural, electric and magnetic properties of $BiFeO_3$ ceramics,
   Pittala Suresh, P.D. Babu and S. Srinath (manuscript under preparation).
6. Study of the Structure and multiferroic properties of Ho Substituted $BiFeO_3$.
   Pittala Suresh, P.D. Babu and S. Srinath (manuscript under preparation).
7. Investigation of Multiferroic Properties of Pure and La doped Bismuth Ferrite,
   P Suresh and S. Srinath, ***AIP Conf. Proc.*** 1347, 314-317 (2011).

8. Structural refinement and observation of enhanced Magnetic properties of La doped $BiFeO_3$,
   Pittala Suresh and S. Srinath, ***AIP Conf. Proc.*** 1512, 76-77 (2013).
9. Observation of High magnetic moment in the Ho doped $BiFeO_3$ ceramics,
   Pittala Suresh and S. Srinath, ***AIP Conf. Proc.*** *1536*, 1059-1060 (2013)
10. Effects of Ho Substitution On Structure and Multiferroic Properties of $BiFeO_3$,
    Pittala Suresh and S. Srinath, ***Proceedings of AMPC2013***, 6-8 February 2013, Chennai, India.

Other Publications:

1. Observation of direct and indirect magnetoelectricity in lead free ferroelectric $Na_{0.5}Bi_{0.5}TiO_3$)–magnetostrictive ($CoFe_2O_4$) particulate composite, A. Srinivas, R. V. Krishnaiah, T. Karthik, **P. Suresh**, Saket Asthana, and S. V. Kamat, ***Applied Physics Letters.*** 101, 082902 (2012).

2. Dielectric and Spectroscopic properties of CuO doped multi-component Li_2O-PbO-B_2O_3-SiO_2-Bi_2O_3-Al_2O_3 glass system, P. Ramesh Babu, R. Vijay, P. Srinivasa Rao, **P. Suresh**, N. Veeraiah, D. Krishna Rao ***Journal of Non-Crystalline Solids***. 370 21 (2013).

3. Magnetic and ferroelectric properties of Fe doped $SrTiO_{3-\delta}$ films, AS Kumar, **P Suresh**, MM Kumar, H Srikanth, M L Post, K Sahner, R Moos, S Srinath, ***Journal of Physics Conference Series***. 200, 1-4 (2010).